



Novel combined fluorescence/reflectance spectroscopy system for guiding brain tumor resections

Master Thesis



Author: Zhiyuan Xie
Supervisor: Stefan Andersson Engels,
Johan Axelsson, Haiyan Xie.
Subject: Photonics Engineering
Level: Secondary



LUND INSTITUTE OF TECHNOLOGY
Lund University

Popular science

This thesis describes a system developed for assisting Glioblastoma multiforme (GBM) brain tumor surgery. The thesis starts with providing some facts of GBM tumor, and introduces some traditional diagnostic methods and their short comes. In the later chapters, the system development details and some tests for the system performances are described.

The glioblastoma brain tumor is a relatively common and really aggressive tumor. Once get the GBM, the quality of life for the patient will be quickly ruined, and in addition it is lethal with a median survival after diagnosis of approximately one year if treated with state-of-the-art treatments.

The first treatment stage of GBM is surgery. In the traditional way, the surgeons have to visually distinguish the tumor margins and then remove the tumor. Unfortunately, due to the similarity in appearance of the tumor to the surrounding healthy brain tissue, the surgery results used to be heavily depended on the surgeons' experiences. You may wonder why it is so important to do the tumor resection. As a matter of fact, research has proved that it is always good to remove the tumor as much as possible, as this will increase the patients' survival time. But over-doing the removing will also cause neurological impairment, which means the patients may lose some vital functions, e.g. hearing, visual or intelligence.

The existing diagnostic methods including MRI, CT and ultrasound can help locating the tumor, but they are generally in lack of accuracy and difficult to fully utilize during the surgeries, so scientists started to searching new techniques to

help intraoperative diagnosis. First, they used the light absorption differences between different types of tissue. This means when shining a light beam on the tissue surfaces, different tissue may re-emit light with different brightness and colors. Later, scientists realized some protein e.g. Flavin and porphyrin molecules in the tissue can give rise to such differences in the re-emitted light. This phenomenon is called autofluorescence. This tissue autofluorescence detecting method later became popular. The method is limited in that the re-emitted light is too weak to be fully utilized during brain surgeries, and it cannot give accurate diagnostic information. Therefore, certain external fluorophores are introduced to generate stronger fluorescence light with better diagnostic information. The fluorophore used in this project is called PpIX, which shows tumor-selective up-taking characteristic. The PpIX concentration in malignant brain tissue can reach up to 50 times higher than in normal tissue.

The system introduced in the thesis can detect and evaluate the diffuse reflected light from the examined tissue, the autofluorescence and the PpIX fluorescence light. The system is constructed with optical components and corresponding electronic system. A computer program was developed for controlling the system.

Some system testing results were shown in the thesis. These results proved the system is with good sensitivity to PpIX fluorescence and is be useful for guiding tumor resections. The future study plans are to investigate the clinical performances of the system during surgeries. We hope this system can benefit the patients.

Abstract

Glioblastoma multiforme (GBM) has long been noted as the most common and aggressive form of brain cancer [1]. The morphological similarity of the tumor with the surrounding tissue cause an extreme challenge to distinguish the tumors from normal tissue during surgeries [1]. Hence there is a need for tools that can guide the surgeon and provide means to better identify malignant tissue.

The fluorescent dye protoporphyrin IX, which is induced by the administration of 5-aminolevulinic acid (5-ALA), has proven to be helpful in guiding the surgical resection [2]. The concentration of PpIX indicates an apparent tumor-selective uptake characteristic in malignant brain tissue[3].

Detection instruments based on fiber optics provide means for localizing of protoporphyrin IX in the surgical bed. This approach has been pursued by several research groups, see e.g. Valdés et al. [4], and Anthony Kim et al. [5]. These instruments rely on detection of the characteristic spectrum of protoporphyrin IX in order to locate the tumor border [7].

The work presented in this thesis spawns from the developments performed by Haj-Hosseini et al. at Linköping University [7]. This original instrument was named ‘optical touch pointer’ (OTP).

The aim of this thesis work was to extend and improve the OTP-system.

The newly developed system described in this thesis is designed to be simple, robust, and more compact. And most

importantly it should also be capable of rejecting the ambient light ever present in the operation theatre.

Two different light source modulation methods were developed and compared in the project. Sensitivity testing and results from phantom experiments using these two methods will be presented. These results show that the system has excellent sensitivity to PpIX fluorescence, and it achieves ambient light influence-free detection.

The improved system developed within the work presented in the thesis could potentially become an important tool for guiding surgical resection in the combat of malignancies of tomorrow. Apart from Glioblastoma multiforme surgical resection, the system should also be able to be used on pancreatic neoplasm, cervical cancer, cholangiocarcinoma, colorectal carcinoma, hepatocellular carcinoma and other similar malignancies detection.

Table of Contents

Popular science.....	1
Abstract.....	3
Table of Contents.....	5
List of Publications	9
Chapter 1 Treatment of Glioblastoma.....	11
1.1 Glioblastoma (GBM).....	11
1.2 Surgical supplementary methods.....	12
Chapter 2 First generation OTP system	15
2.1 Principle components of the OTP system	15
2.2 Final design of the first generation OTP.....	16
2.2.1 Light source.....	17
2.2.2 Light guiding optical fibers.....	18
2.2.3 Detection units.....	19
2.2.4 System Control and Data Analysis.....	19
Chapter 3 Project purpose and objective.....	24
3.1 Objectives.....	24
Chapter 4 Theory	26
4.1 Interaction of light with tissue.....	26
4.1.1 Properties of light.....	26
4.1.2 Tissue optical properties.....	27
4.1.3 Diffuse reflectance spectroscopy.....	30
4.2 Fluorescence	31
4.2.1 Auto-fluorescence.....	31
4.2.2 5-aminolevulinic acid (5-ALA).....	33
4.3 Optoelectronics	36
4.3.1 Light emitting diodes (LED)	36
4.3.2 Laser diode	37

4.3.3 Photodiodes and avalanche photodiodes (APD).....	38
Chapter 5 System design.....	40
5.1 Hardware design	40
5.1.1 Optical hardware design	40
5.2 Signal processing methods.....	45
5.2.1 Square wave modulation method	46
5.2.2 Sine wave modulation method	48
5.3 System hardware design and components selection	52
5.3.1 Light source.....	52
5.3.2 Transmission fibers.....	54
5.3.3 Detecting components designing method	55
5.3.4 Input/output ports	56
5.4 Software design.....	57
5.4.1 Labview programming for square wave modulation	58
5.4.2 Labview programming for sine wave modulation	59
5.4.3 Matlab program for evaluating the measurements' results	60
5.5 System construction.....	61
Chapter 6 System capacity test.....	63
6.1 System calibration	63
6.1.1 Calibration method.....	63
6.1.2 Calibration result and analyses.....	65
6.2 System ambient light resistance ability test	66
6.2.1 Ambient light resistance ability test method.....	66
6.2.2 Ambient light suppression ability test result.....	67
6.3 System fluorescence sensitivity test.....	70
6.3.1 System fluorescence sensitivity test method.....	70
6.3.2 System PpIX fluorescence sensitivity test results.....	72

Chapter 7 Discussion and conclusions	75
7.1 Future works	75
7.2 Conclusion and outlook.....	76
Self-reflection	77
References	80
Appendix A.....	84
1. Square wave modulation method back panel	84
2. Sub VI program for Square wave modulation method	84
3. Sine wave modulation method front panel.....	84
4. Sine wave modulation signal processing Matlab program.....	88
5. Square wave modulation signal processing.....	94
Appendix B.....	108
Papers	108

List of Publications

This thesis is based on the following papers, including 3 conference papers and 1 journal paper. The papers are attached at the end of the thesis numbered by Roman numerals.

I. Design and validation of a fiber optic point probe instrument for therapy guidance and monitoring

Haiyan Xie, Haiyan Xie, Monirehalsadat Mousavi, Niels Bendsoe, Mikkel Brydegaard, Johan Axelsson, Stefan Andersson-Engels

Journal of Biomedical Optics. 2014.

II. Ambient Light Rejecting Fiber Optic Probe for Brain Tumor Surgical Resection Guidance

Haiyan Xie, Mikkel Brydegaard Sørensen, Zhiyuan Xie, Monirehalsadat Mousavi, Johan Axelsson, and Stefan Andersson-Engels

ECBO conference, Germany, 2013.

III. Novel combined fluorescence/reflectance spectroscopy system for guiding brain tumor resections – hardware considerations

Zhiyuan Xie, Haiyan Xie, Monirehalsadat Mousavi, Mikkel Brydegaard, Johan Axelsson, Stefan Andersson-Engels

SPIE conference, Riga, 2013

IV. Development of a novel combined fluorescence and reflectance spectroscopy system for guiding high-grade glioma resections

Monirehalsadat Mousavi, Haiyan Xie, Zhiyuan Xie., Mikkel Brydegaard, Johan Axelsson, Stefan Andersson-Engels

SPIE conference, Riga, 2013

Treatment of Glioblastoma

In this chapter, the brief medical background of the glioblastoma tumor, existing surgical supplementary methods will be introduced and discussed.

1.1 Glioblastoma (GBM)

Glioblastoma multiforme (GBM) is the most common and aggressive form of diffuse astrocytoma. It presents a low survival rate and short surviving time, with around 90% of the patients die within 3 years after the initial diagnosis. Due to this, GBM stays in the top ranking among all important neuro-oncology indications [7]. In addition, the invasive growing characteristic of GBMs and its similar appearance to surrounding functioning brain renders ample difficulties when performing surgery. To illustrate the unclear boarder of the GBM tumor, images taken with MRI is shown in Figure 1.

A detailed study based on 416 patients was made in order to determine how different variables influence the survival time of the patients [1]. Proper surgical resection appears to improve the survival time significantly. The minimum requirement for surgical resection is 89% of the tumor volume. However, resection of over 98% the tumor volume was considered to be desirable [1]. In Table 1, the comparison of median survival time in between resection volume exceeding and subceeding 98% is shown.

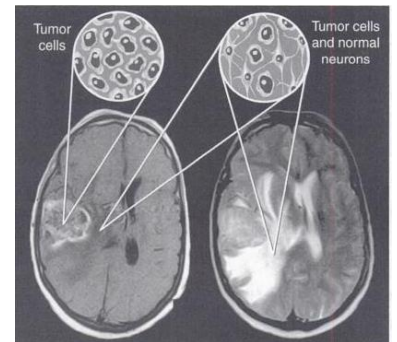


Figure 1 The hyper-intensity on T1-weighted MR images show the contrast enhanced tumor mass (left) which is composed of tumor cells without intervening brain parenchyma (left insert). The T2-weighted MR imaged (right) shows surrounding of this mass which is composed of infiltrating tumor cells (right insert) [8].

Table 1 Clinical out-come groups and length of survival in 416 patients with GBM [1]

Outcome Group	Number of patients	Median survival in Mos(95%CI)	Median Survival in months	
			Over 98% Resection	Less than 98% resection
A	15	35.3(not defined)	35.3(8)	32.8(7)
B	89	14.9(11.7-18.0)	19.0(49)	10.9(40)
C	184	10.7(9.2-12.2)	13.1(79)	8.3(105)
D	128	8.2(6.6-9.8)	8.6(61)	7.8(67)

From the results, the importance of complete tumor resection for the survival time is obvious. In addition, the study of Lacroix et al. also showed that the quality of life was improved for a surviving patient when more complete resection is accomplished [1].

1.2 Surgical supplementary methods

In modern surgery, efforts are made to distinguish GMB from surrounding tissue. The optimal result is to reach maximal tumor removal with minimal neurological damage [9]. This is for avoiding neurological impairment of the healthy brain and the corresponding neurological functions [10]. Since safe and effective resection of GBMs is highly dependent on correct localization and identification of the tumor, different surgical supplementary methods have been developed. This includes high-resolution intraoperative ultrasound, image guided frameless stereotaxis, and intraoperative CT or MR imaging [8].

However, all these techniques have their limitations. The intraoperative ultrasound offers quite poor spatial resolution and quite limited sensitivity [11]. As shown in Figure 1, even T2-weighted MR images cannot really distinguish the boarder unless the cancer cells are with certain density, moreover tiny shift of brain in the examining process will lead to a spatial inaccuracy. Most of these diagnostic methods cannot be used during surgery [12]. In reality, the neurosurgeons will still have to visually distinguish the margins from normal tissues, which make the results neither quite reliable nor stable and is heavily dependent on the surgeon's experience.

Hence, a real-time, high sensitivity, safe and intraoperative guidance tool for tumor margin detection is desperately in need. In order to meet this need, optical spectroscopy, has been suggested as a tool for surgical guidance [9].

There are many methods that rely on optical interrogation of the brain, some of these modalities aimed for surgical guidance are:

- Raman spectroscopy, a method which locates different tissue by their molecular composition [13].
- Scattering spectroscopy (e.g. time-resolved spectroscopy) which relies on the intrinsic scattering and absorption of the tissue [14].
- Autofluorence spectroscopy, there the tissue proteins' fluorescence is induced by UV-blue light (366nm and 405nm) [15].

The most widely used method nowadays, however, is fluorescence spectroscopy based on an exogenous fluorescence agent, e.g. HpD (hematoporphyrin derivative), ALA (5-

aminolevulinic acid), Chlorins and Phtalocyanine [16][17]. They provide rapid, sensitive and safe differentiation between tumor and benign tissue in various organ systems in vivo.

The group at Lund University, already in 1991 had made an optical fiber based system for distinguishing GBMs [18]. In 2000, Stummer et al. proved that the 5-aminolevulinic acid-induced protoporphyrin IX (PpIX) is helpful in guiding the GBM resection in surgery [19]. Later, the optical fiber based system developed by Valdés et al. can detect both fluorescence and reflectance spectroscopy at the same time. This system has proved to have up to 94% accuracies on declining tumor tissue in vivo quantification.

In parallel to these remarkable steps, a new system called ‘optical touch point’ (OTP) was developed in a collaboration between the Lund and Linköping Universities. It correlated to Stummer’s study on 5-ALA induced tumor fluorescence and Valdés’s study on fluorescence combined with reflectance spectroscopy for efficient tumor resection guidance [4][6]. This system mainly works by detecting the characteristic spectrum of PpIX with a fiber optic probe allowing tumorous tissue to be identified [6][20].

First generation OTP system

Haj-Hosseini et al.'s 'optical touch pointer' system is a clinically proved system. It is important to understand the system properly and to analyze the short-comings of this system for enabling further improvements.

As mentioned above, most imaging systems and the OTP system are developed based on the fluorescence properties of tumors. In typical cases, imaging systems have a limited depth penetrating ability, subsurface regions the imaging modalities are restricted [21][22]. In contrast, the use of nonimaging contact-point fiber probes can allow the detection of deeply embedded malignanat regions. Under certain condition this can make the localization of the rumor more accurate [23].

In order to distinguish the two ongoing projects from Lund University and Linköping University, the Linköping University system is referred to as '1st generation OTP system' in the following chapters.

2.1 Principle components of the OTP system

Generally, a fiber based fluorescence spectroscopy system consists of three distinct parts with corresponding interfaces (filtering) in between: a light source or several light sources, light guiding fibers, and a detection part. See Figure 2.

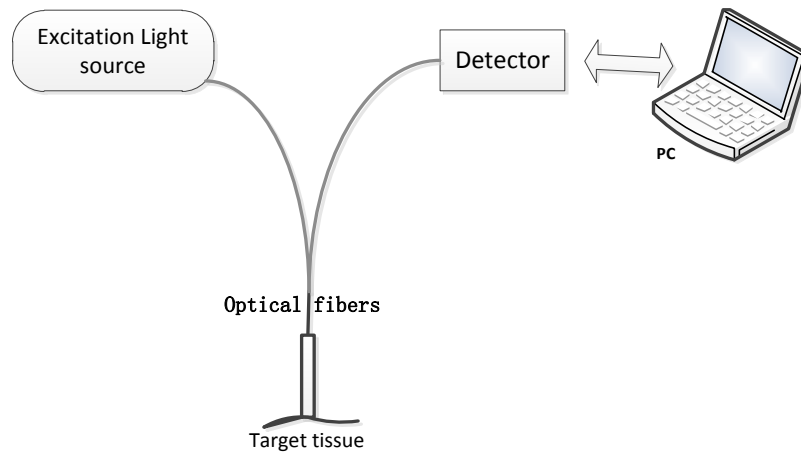


Figure 2 Schematic drawing of the principal components of the OTP system [24]

Figure 2 presents the very basic model of the optical touch pointer system. All systems mentioned in this thesis have these features in common.

In the schematic drawing in Figure 2, the light guiding part consists of at least two fibers practically, one for illumination and one for light collection. Changes to the number of fibers, the light source types or the detection instruments can be made according to different system requirements [24][25].

2.2 Final design of the first generation OTP

The 1st generation OTP system final set up sketch is shown in Figure 4.

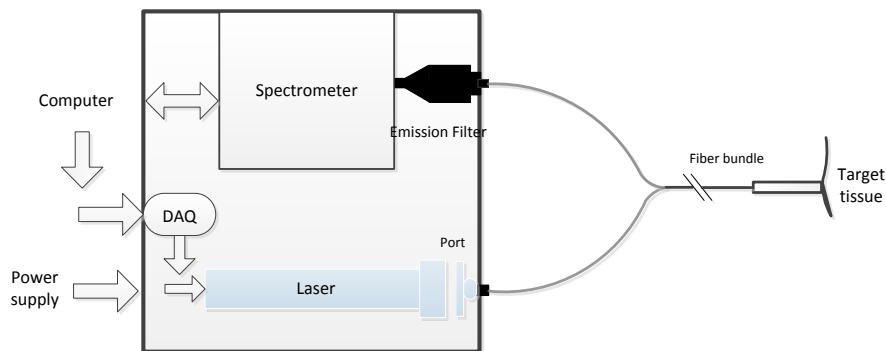


Figure 4 Sketch of the final version of the first generation OTP system [26]

2.2.1 Light source

In the final model of the first generation OTP system, a 405nm laser is used as light source. Originally a 395nm LED light was installed. However the LED light source was not capable of efficient excitation of the fluorophore due to coupling losses. For this reason a laser source was applied instead. The laser light source is controlled by computer interface created with LabView (National Instruments Inc., USA) through the signal in/out device DAQ card (National Instruments Inc., USA) [26].

2.2.2 Light guiding optical fibers

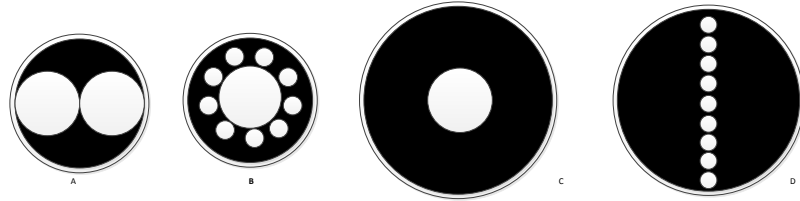


Figure 5 The design of different alternative for light guiding optical fiber assemblies. Images A) and B) illustrate the fiber arrangements for the detecting end that will attach the tissue, In A) one of the fibers is used for the excitation light while in B) the multiple smaller fibers are employed for the excitation. The other core is for collecting emitted or scattered light. The illustrations C) and D) illustrate the corresponding end that goes into the detector. The fibre arrangement in D) is specially designed for spectrometer detection, as the entry slit of normal spectrometers is line shape [27] .

The light guiding part of the system is based on optical fibers. In Figure 5, two different kinds of fiber assemblies are presented. Figure 5A and C shows the single core illumination fiber solutions, while Figures 5 (B) and Figures 5 (D) illustrate assemblies for multiple core illumination fibers'. Both designs were used in the first generation OTP system.

When choosing a suitable fiber for the system, apart from considering the numerical aperture of the fibers, it is important to consider the fiber geometry. As the collected light intensity and spectrum shape would be influenced by the fiber geometry.

The hand held optical fiber probe has a 600nm core and 950 nm total diameter, while the numerical aperture of the fiber is 0.37. The excitation fiber is surrounded by 9 other fibers, as shown in Figure 5 (B). They all have a core diameter of 200 μm core and a numerical aperture of 0.22. The optical fiber

bunch is arranged to match the slit configuration of the spectrometer at the detector end, which is 200 μ m wide [26][27].

2.2.3 Detection units

The detection part of the 1st generation OTP system is based on the spectrometer (EPP 2000, Stellarnet). This spectrometer include 2048 element CCD operating in the wavelength range of 240–850 nm with a resolution of 3 nm, this spectrometer is coupled to the system to measure the collected optical signal. Typical integration times for retrieving spectra with satisfactory signal-to-noise ratio is no less than 30ms [26] [25].

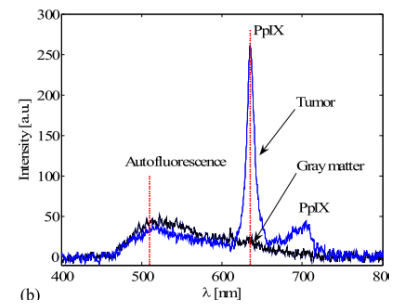
As a result of the long integration time, diffused back-scattered light would saturate the spectrometer. In order to suppress such light to reach the detector, a long pass filter at 475nm (Schott CG-GG-475-0.50-3, CVI, USA) is fixed in front of the detector slit.

2.2.4 System Control and Data Analysis

The system control and data analysis are processed through Labview programs. System control consists in terms of laser pulse generation and spectrometer spectra acquisition. These two processes should be performed in real time. Data analysis is done off-line in Matlab program after data collection.

System Control

The ambient light sources that might exist in the surgical room include fluorescent tubes, surgical lamps and surgical microscopes. In order to suppress the ambient light influence the laser is pulsed using a square wave 50% duty cycle. Two spectra are taken after each other: when the laser is “on” and later when the laser if “off”. The two spectra are named “light



(b) **Figure 6.** Representative spectrum acquired using the result of first generation system from a glioblastoma patient. In this case 5 mW laser power with 0.4 s integration time (2 mJ excitation) was used. PpIX peaks are apparent at 635 and 704 nm [28].

spectrum” and “dark spectrum”. The final spectrum that is subject for analysis is retrieved using Equation 1.

$$\begin{aligned} & \textit{Compensated spectrum}(i) \\ & = \textit{Light spectrum}(i) - \textit{Dark spectrum}(i) \end{aligned} \tag{1}$$

The compensated spectrum effectively reduced the influence from ambient light sources, since all such contributions are efficiently subtracted in Eq. 1. Figure 7 presents the experimental results from Haj-Hosseini et al. [27]. The figures show that the ambient light can be rather successfully suppressed, while the operating lamp and operating microscopy lamp seems to alter the form of the resulting spectra somewhat.

The spectrometer is set to be synchronized with the light source (50% duty cycle). To generate a fluorescence signal with sufficient signal-to-noise ratio, each spectrum was recorded with an illumination energy of 2mJ, this required a 0.4s recording time with a 5mW laser power [6].

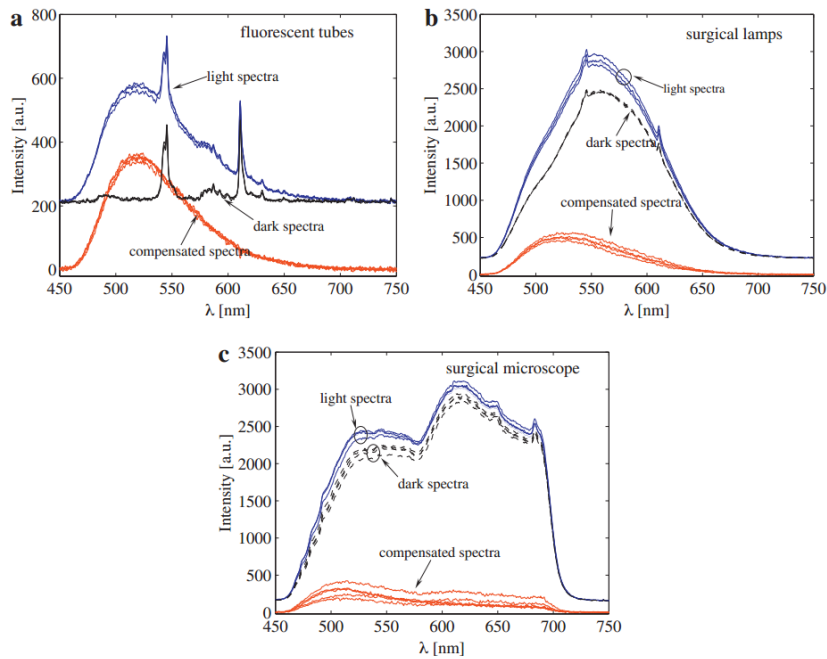


Figure 7. Skin measurement results under 5mw laser power, and 0.4s exposure using the original OTP design. Every image includes the light, dark and compensated spectra results. From the relative intensity of compensated spectra, it shows the goal of suppressing the ambient light is reached [6].

The compensated spectra are shown on the monitor in real-time and saved for off-line data processing. The instant presentation of the spectrum allows immediate control of signal quality and adjustment.

Data analyzing

Recorded fluorescence signal are analyzed by using MATLAB 7.8.0 (MathWorks™, Inc., Natick, MA) and Minitab (Minitab, Inc., State College, PA). The probe geometry, i.e. the alignment of the fiber probe relative the surface can influence the detected intensity.

In order to eliminate such influences, the detected signal is processed using Equation 2.

$$\text{Ratio number of compensated spectrum } (i) = \left(\frac{I_{PpIX} - I_{base}}{I_{autofl}} \right)_i$$

(2)

In Equation 2, I_{PpIX} Is the total fluorescence at 635nm, I_{base} at 635 nm is used as a reference level, while I_{autofl} is the maximum auto-fluorescence level at 510 nm, schematically depicted in Figure 6 [6][10][30][28].

Conclusion of the system performance

It was concluded that the 1st generation OTP system was able to discriminate between tumor and normal tissue, based on the collection of PpIX fluorescence. However, some problems still were presented, which formed the motivation for the work within this thesis. The problems with the first generation OTP system were:

1. Incompact system construction.
2. Data analysis is not performed in real time and it is somewhat complex, while not adequately compensating for all measurement uncertainties. The analysis needs to be conducted into Matlab.
3. The signal collection needs relative long integration time in order to retrieve spectra with good signal-to-noise ratio. This is needed as the sensitivity of the spectrometer is limited and in order to reduce the influence of ambient light. In turn the long integration time would cause strong photobleaching and also slightly slow down the surgery process.

4. Intricate analysis using two different program interfaces (LabView and SpectraSuite) must be involved in order to control the light source and spectrometer, respectively.
5. The system uses a single wavelength laser as the light source, but LEDs would be preferred in clinical use for laser safety, cost and reliability reasons.
6. The spectrometer is big, easy to saturate and need a long integration time to obtain signals with a sufficient signal-to-noise ratio. Due to the long acquisition time it cannot be used in any efficient modulation detection schemes to reduce the influence of the ambient light.

Project purpose and objective

3.1 Objectives

In order to solve the problems mentioned above, and improve system performance the following objectives were defined. The overall goal of this diploma project was to develop a system that is safe, user-friendly, able to efficiently suppress ambient light, provide more robust diagnostic information by adding new information, featuring on-line data processing, while being fast and sensitive.

- A. In order to replace the relative low-sensitive spectrometer in the 1st generation OTP system, and to skip the trouble of controlling the system from two different interfaces, the light detection unit was redesigned.
 1. A custom made metallic box, holding all the optical components, should be designed for the system.
 2. The optical components should be oriented and fixed into the optical box.
 3. A new electrical circuit should be designed for signal generation and light detection.
 4. Software should be developed in LabView for system operation and data analysis.
 5. The new system should be spectrally calibrated for further use.
- B. The excitation light source was replaced with a Multi-LED source. This was done primarily in order to present means for collecting also diffusely reflected light signals at several wavelengths. This can be important since this scheme enables retrieval of autofluorescence and signals related to

the optical properties of the tissue under study. The objective in this work was to test the feasibility of using a Multi-LED source as the excitation source, in place of the laser source.

1. A multi-LED source should be linked into the system.
 2. The output power from the multi-LED source should be measured and the transmission losses assessed.
 3. Development of new modulation methods for the multi-LED source that controls how the LEDs are turned on and off.
 - A sine wave modulation method should be developed and tested.
 - A square wave modulation method should be developed and tested.
- C. System sensitivity test with two modulation methods.
1. For both methods, evaluation tests should be done to estimate the ambient light influences on the system sensitivity. This should be done by measurements in Intralipid© liquid phantoms with different PpIX fluorophore concentrations, i.e. dilution experiment.
- D. The data analysis need to be performed using principal component analysis and this scheme should be developed based on the phantom measurements.

Theory

4.1 Interaction of light with tissue

This thesis mainly focuses on the use of fluorescence spectroscopy for tissue characterizing. Fluorescence spectroscopy is a type of optical spectroscopy, which is the study of electromagnetic radiation with matter that occurs as UV/VIS spectral region [24].

To give a detailed explanation of fluorescence spectroscopy, the principle of light-tissue interaction should be introduced.

4.1.1 Properties of light

Visible light is the ‘light’ that people normally talking about, it comprises a narrow band of electromagnetic radiation that can be perceived by human eyes [31]. As illustrated in Figure 8, the visible light spectrum lies in between 400nm and 780nm.

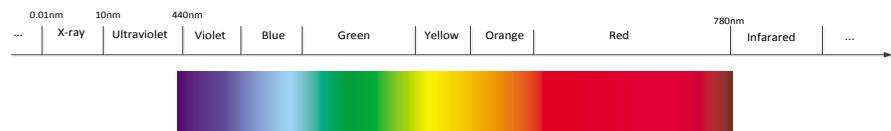


Figure 8 Electromagnetic radiation spectrum

The individual light photon energy is presented as

$$E = h\nu = hc/\lambda \quad (3)$$

In Equation 3, h is the plank constant. $\lambda = c/\nu$ is the light wavelength, c is the speed of light and ν is the light frequency.

4.1.2 Tissue optical properties

When light interacts with tissue, many different processes can take place. As shown in Figure 9, at the tissue-air surface, part of the incident light is reflected off, and the rest will enter the tissue. Light that propagates inside the tissue will either be scattered or absorbed. The scattering and absorption properties of the tissue are wavelength depended.

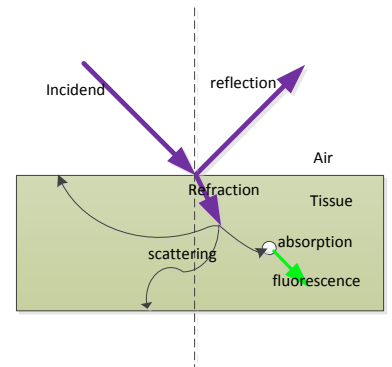


Figure 9 Interaction between light and tissue.

Absorption

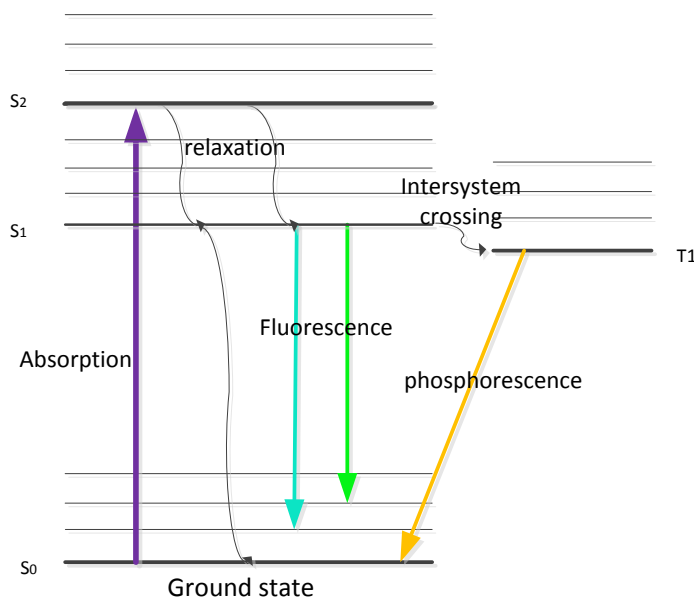


Figure 10 Jablonski diagram for illustrating the possible relaxation processes after a molecule absorbs a photon, including nonradiative radiation, fluorescence and phosphorescence processes [24].

When the energy of an incident photon equals to the energy differences of two energy levels in a molecule, this photon can be absorbed. As shown in Figure 10, the molecule, or chromophores, can be excited to a higher level following absorption of a photon. The molecule will then relax to its ground state through two main processes. One process is when the energy is dissipated through nonradiative energy transfer, essentially heating the tissue. The other process is when the

molecule de-excites through emission of lower energy photons, i.e. fluorescence.

In Figure 10, 3 different energy levels are shown. The ground level S0, and two excited states (S1, S2), every molecule has several distinct energy states. And the sublevels shown in figure are the molecular vibration states, each vibration state splits into several finer levels, these finer levels are the molecule rotational states (not shown in figure). These energy levels are associated with the nuclear and electron spin of the molecules [24].

When light illuminates tissue, photons can be absorbed by different types of chromophores. The probability of one photon being absorbed per unit length is defined as absorption coefficient.

$$\mu_a^\lambda = \ln(10) \cdot \varepsilon^\lambda \cdot C \quad (4)$$

In Equation 4, ε is the molar extinction coefficient, C is the tissue constituent concentration.

From Equation 4 one can tell the absorption coefficient is wavelength dependent. Some main chromophores' absorption spectra are shown in Figure 11.

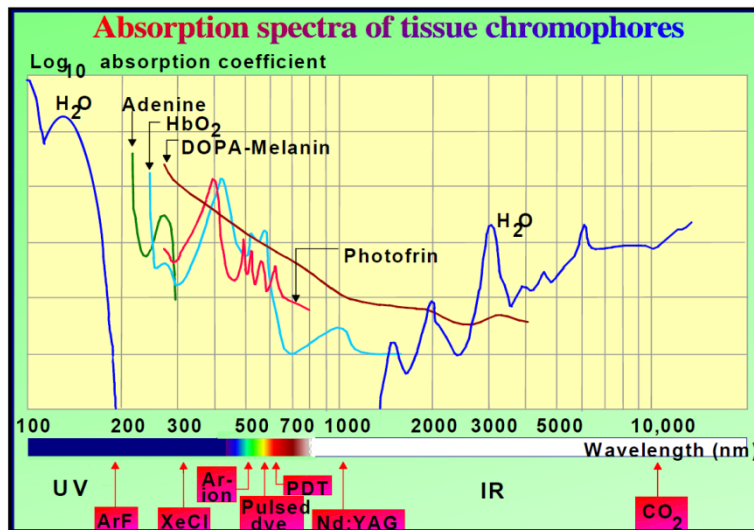


Figure 11 Absorption spectra of tissue chromophores

As shown in Figure 11, common chromophores like haemoglobin and melanin absorb strongly in blue to UV region. Meanwhile water is the main absorber in infrared region. Between 650nm-1300nm the chromophores absorb least, this spectrum band is called the 'tissue optical window' [32].

Scattering

Photon propagation in the tissue can also be subject to scattering.

Rayleigh scattering and Mie scattering are two types of elastic scattering. In these scattering processes, the incident light doesn't lose any energy, only the light propagating direction is changed. Mie scattering happens when the light wavelength is smaller than scatterers size. Mie scattered light intensity increases towards shorter wavelength with an approximate λ^{-2} dependence [16]. Rayleigh scattering happens when the incoming light wavelength is bigger than the little particle or molecule sizes. Similar to Mie scattering, Rayleigh

scattered light intensity increases towards shorter wavelength with an approximate λ^{-4} dependence.

If incoming light interaction with molecule different vibration or rotational levels and cause transition, the scattering process will be inelastic, e.g. Raman scattering [32]. With different initial and final energy state, the wavelength is Raman scattered light can either be red shifted or blue shifted, they defined as Raman Anti-stokes and Raman stokes, respectively.

Due to the refraction index mismatches at microscopic boundaries, tissue is a highly scattering media, also called turbid media. Light in tissue rarely travels straightly, but scattering around.

The scattering coefficient μ_s is used for describing the turbid media scattering. It is defined as the probability of scattering per unit length. However, as the scattering in tissue is not isotropic, in order to describe the scattering anisotropy, the anisotropy factor g that is related to the average scattering angle is used [33].

$$g = \int_{-1}^1 \cos\theta f(\cos\theta) d\cos\theta \quad (5)$$

Tissue g is normally equal to 0.8-0.95 [34]. The reduced scattering coefficient is defined as in Equation 6,

$$\mu'_s = \mu_s(1 - g) \quad (6)$$

$1/\mu'_s$ Measures the mean free path between either a scattering or absorption event.

4.1.3 Diffuse reflectance spectroscopy

Diffuse reflectance spectroscopy is based on the evaluation of the reflected light escaping the tissue following irradiation of

the tissue with a light source. It can be used to provide direct measurements of the light absorption and the scattering coefficients. These properties characterize the tissue physiology and can form important means for detection of malignancies and tissue types [35]. In the project, the diffuse reflectance signal is considered as an important factor for distinguishing tissue types as complement to the fluorescence light signal.

4.2 Fluorescence

As shown in Figure 10, fluorescence process is one of the possible processes that can occur after a molecule absorbs a photon. The tissue auto-fluorescence and fluorescence from PpIX are the two fluorescence signals utilized in the project.

4.2.1 Auto-fluorescence

Auto-fluorescence is the phenomenon that occurs when UV/blue light is illuminating the tissue, resulting in blue-green fluorescence light being emitted from proteins existent in the tissue. Auto-fluorescence spectroscopy has been used for diagnostics before today's wide use of exogenous fluorophores.

The tissue auto-fluorescence is due to several endogenous fluorophores from tissue matrix molecules and intracellular molecules including different proteins, flavins and porphyrins[31]. Different disease cells appear to have different concentrations of these fluorophores, which makes it possible to detect tissue alterations optically [36]. Also the extra blood flow due to tumor vascularization will decrease the fluorescence signal, as the increase of blood increases the amount of light absorbed [37]. This means that a significant variation in auto-fluorescence signal intensity can reveal the existence of a tumor.

Table 2 Wavelengths for excitation and emission maxima for the most abundant endogeneous tissue fluorophores [24]

Fluorophore	$\lambda_{\text{exe}}(\text{nm})$	$\lambda_{\text{em}}(\text{nm})$
Tryptophan	275	350
Collagen	340	395
	270	395
	285	310
Elastin	460	520
	360	410
	425	490
	260	410
NADH	350	460
β -karoten		520
Endogenous porphyrins	400	610,675

4.2.2 5-aminolevulinic acid (5-ALA)

As the design of the system is based on the optical property of the fluorescent dye 5-aminolevulinic acid (5-ALA) induced protoporphyrin IX (PpIX), the transition from 5-ALA to PpIX and the special properties of PpIX should be introduced first.

5-ALA acid is preferred among all drugs in tumor marking and PDT diagnostics. As shown in Figure 12, 5-ALA occurs naturally in human body as a metabolite in the heme biosynthesis pathway. Malignant glioma cells or abnormalities that exist in the epidermis would take ALA in, and converted it into strongly fluorescing protoporphyrin IX(PpIX) which is a photosensitive compound [38][39]. PpIX shows tumor-selective up-taking characteristic, its concentration in malignant brain tissue can reach up to 50 times higher than in normal tissue. The possibility of been used locally in a topically application instead of systemically is many times preferred when it is possible, e.g. for skin , bladder and lung tumors [40].

Based on all these superb properties of 5-ALA, image based system and fiber based system have being developed [26]. Vital brain tumor tissue can, using such systems, be delineated using ALA-induced fluorescence. This allows significant improvement in surgical results compared to conventional surgery without fluorescence guidance [41].

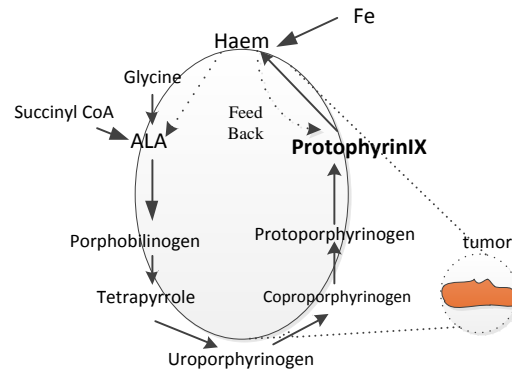


Figure 12 Haem cycle [16].

PpIX fluorescence

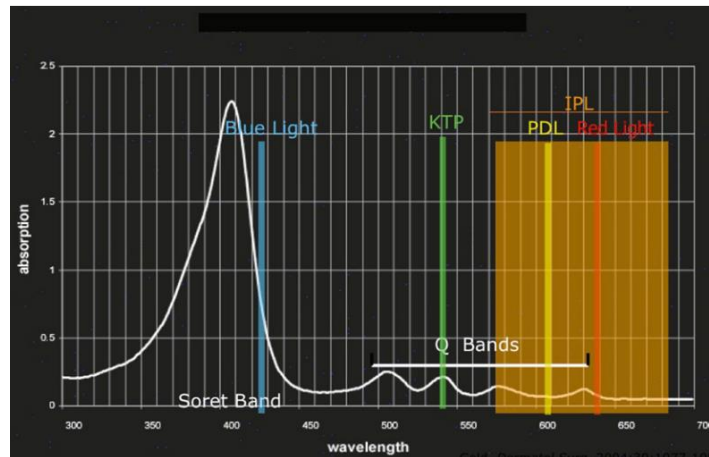


Figure 13 PpIX absorption peaks. 390-400nm absorption peak occurs, Q-bands extend from 510 to 630nm are with lower absorption. Hence, generally light source with wavelength around 400nm is widely used to induce PpIX fluorescence [39].

In Figure 13, the PpIX absorption spectrum is shown to determine what excitation light wavelength to be used. It is obvious from the figure that the main absorption peak occurs at around 390 to 400nm.

When 405nm excitation light is used to excite the PpIX, it introduces a strong fluorescence emission at 635nm and 704nm, as shown in the spectrum in Figure 14.

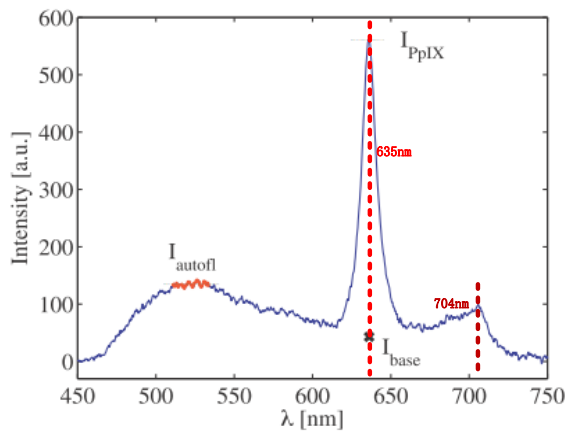


Figure 14 PpIX fluorescence spectrum generated by 405nm excitation light. The peak at around 510nm is caused by brain auto fluorescence [6].

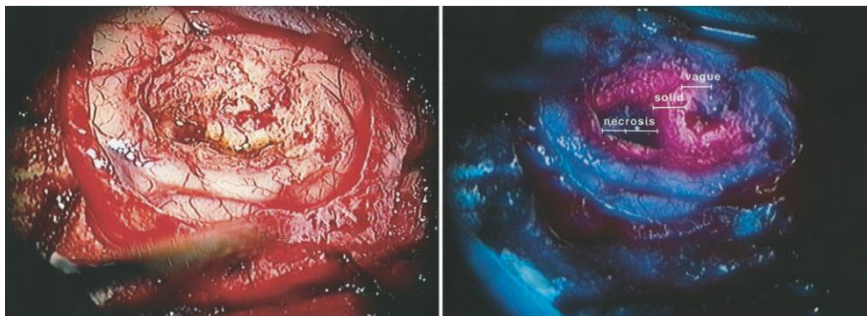


Figure 15 Intraoperative photographs demonstrating tumor cavity viewed under conventional white light (left) and violet-blue illumination (right). PpIX fluorescence is proved to be able to mark the tumor margin [20].

In Figure 15, violet-blue light is used to illuminate on glioblastoma compared to white light. It is seen that ALA-induced PpIX fluorescence is possible to mark tumor margin. Although the view is quite blurry, the tumor outline is faintly visible.

Hence, it is possible to develop fast, robust and non-invasive optical biopsy equipment based on the 5-ALA induced PpIX fluorescence property that can be used for tumor resection guidance.

4.3 Optoelectronics

Optoelectronic devices are small, highly efficient, robust, simple to control and sensitive. All these properties are consistent with the system design target. In the design, laser diodes (LD) or light emitting diodes (LED) are used as light sources, and photo diodes (PD) or avalanche photon diodes (APD) are used as detectors.

4.3.1 Light emitting diodes (LED)

A light-emitting diode (LED) is a simple and basic optoelectronic component. It is constructed by a P-N junction. P-N junction is formed by two pieces of closely attached semiconductor materials, one of which is a P-doped material which has an increased hole concentration in the material. The other one is an N-doped material with increased electron concentration. Close to the depletion region, electrons and holes can move freely across the depletion region until thermal equilibrium in the p-n junction is reached. If no external electric field is applied, the thermal equilibrium would give rise to a potential voltage difference eV_0 .

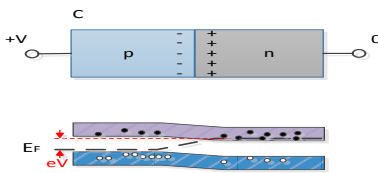


Figure 16 Forward biased P-N junction

When this junction is biased, the outer electric field breaks down the equilibrium and drives the carriers to flow through the junction. Because of this flow an efficient recombination of electrons and holes takes place and in the process photons are emitted. This is referred to as recombination radiation.

There are two important properties of LEDs.

First, the power conversion efficiency of LED is

$$\rho_c = \frac{P_o}{iV} = \rho \frac{hv}{eV} \quad (7)$$

Where V denote the voltage drop across the LED, $\rho = \rho_i \rho_e$ is external efficiency, ρ_i is the internal efficiency and ρ_e is the extraction efficiency. Second, the power output of the LED light is defined by

$$P_0 = hv\varphi = \rho \frac{i}{e} \quad (8)$$

Nowadays, LEDs are widely used as indicate lights , mobile and computer screens, televisions are all illuminated with visible LEDs due to the small size and low price with great durability, LED screens are gradually replacing all the old type screens in the modern electric world. As illumination light source, white LEDs are replacing the old fluorescent lamps and incandescent lamps as they are more stable and energy conserving.

4.3.2 Laser diode

A laser diode is essentially an LED where the crystal planes of the diode, normal to the p-n junction, have with high reflective efficiency. The surfaces are either highly polished or cleaved, sometime extra reflective layers are added on. The high reflection surfaces form a resonant optical cavity for narrow band wavelengths lasing in. Like all other laser light source, this would cause high energy and coherent narrow band radiation output.

The LD output power is

$$P_0 = \rho_d (i - i_t) \frac{1.24}{\lambda} \quad (9)$$

Where i_t is the threshold current.

The LD's power conversion efficiency is defined by

$$\rho_c = \rho_d \frac{(i - i_t) hv}{ieV} \quad (10)$$

4.3.3 Photodiodes and avalanche photodiodes (APD)

Photodiodes and avalanche photodiodes are low cost and widely used semiconductor optical detectors. With good performance and large varieties in sizes, response frequencies, materials and other characteristics, they are quite often used in the photon sensation project.

Although the basic elements of normal light emitting diodes and photodiodes are both P-N junctions, the working principle of photodiodes is very opposite to the normal light emitting diodes. Instead of emitting photons from the recombination of electrons and holes, the photons enter P-N junction and get absorbed. Extra electron and hole pairs are then generated in the depletion area. In addition, P-N junction photodiodes are not the only type of photodiodes, there are versions made from P-I-N junction components, the 'I' refers to 'intrinsic', which is a low doped semiconductor material, this 'I' structure forms a long depletion layer in between P and N material. P-I-N junction photodiode is more efficient than normal photodiode.

An APD is normally a P-I-N diode. The only difference of APDs and normal photodiodes is that APDs are with much higher gain coefficient. When heavily biased, the generation of electron-hole pairs would speed up, and random collisions may occur in between electrons, which has a certain possibility to generate an extra electron-hole pair.

For PDs, there are few properties are important.

Responsively defines how well the detector generates a current depending on the incoming light. High responsively is important for detectors.

$$R = \frac{i_p}{P} = \frac{\rho e}{h\nu} = \frac{\rho \lambda}{1.24} \quad (11)$$

In the formula, ρ is the quantum efficiency of the component which is wavelength dependent.

For APD, the responsivity is defined as

$$R = \frac{i_p}{P} = \frac{\rho M e}{h\nu} = \frac{\rho M \lambda}{1.24} \quad (12)$$

M is the gain coefficient of the APD.

Unfortunately, APD and PD are temperature sensitive components seen in Figure 17 where the responsivity is plotted as a function of the temperature.

From their i-V property we can see from Equation 13.

$$i = i_s(e^{eV/kT} - 1) - i_p \quad (13)$$

Where i_p is the photon current proportional to the photon flux density, and i_s is the saturation dark current. The first part of the equation is the APD dark current. V is the device bias voltage. T is the operational temperature of the diode.

First, from Equation 13 one can tell the dark current of APD is temperature dependent. When applying bias voltage, dark noise would be reduced with lower temperature as well. As from Figure 17, it is obvious that the gain of APD is temperature dependent. So while the bias voltage is constant, decreasing the device temperature would increase APD responsivity [42].

In general we conclude that both the PD and APD show a performance that is temperature dependent. Both devices will provide a better performance if cooled below room temperature.

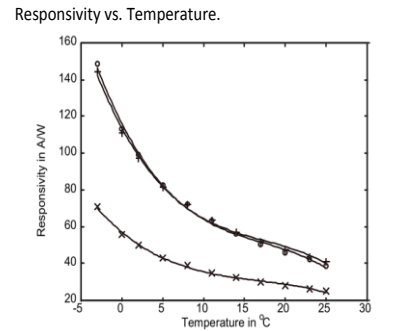


Figure 2 APD responsivity variation with temperature at 336 V bias at (o) 720 nm, (+) 820 nm and (x)940 n [42].

System design

5.1 Hardware design

5.1.1 Optical hardware design

As introduced in chapter 4, PpIX fluorescence, as well as diffuse reflectance and auto-fluorescence from tissue, can help to differentiate tumor from normal tissue. In the system developed within this project, a 405nm light source was chosen to act as the illumination source. It allows excitation of PpIX fluorescence as well as tissue autofluorescence.

Transmission filters are used to separate different spectral bands out from the collected light. The filtered light is routed onto individual light detectors, effectively creating a low resolution spectrum.

In the design, light sensors are located at the end of five plastic tubes, and four corresponding beam splitters are used for guiding light into these tubes. In the following sections, these five tubes and the optical systems included are referred to as ‘channels.’

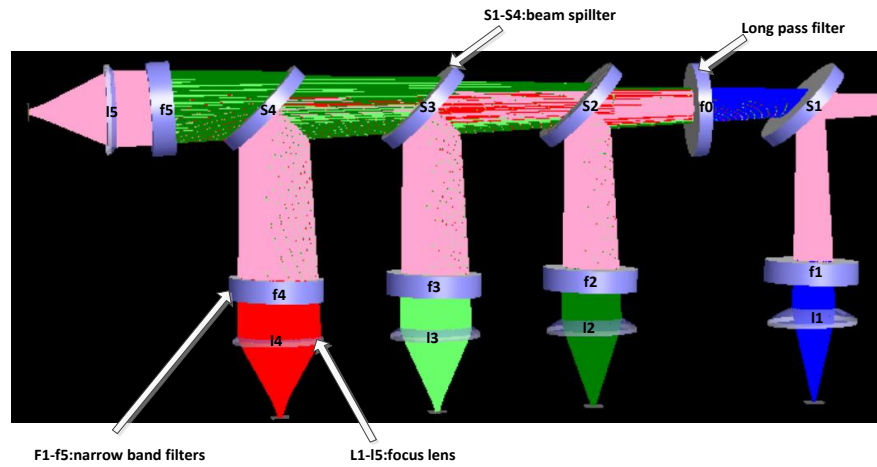
In Table 3, the five filters that are applied in these five channels are listed together with the main function of each channel.

Table 3 List of optical channels

Channel number	Channel function
Channel 1 (405nm)	Scattering spectrum
Channel 2 (510nm)	Auto fluorescence
Channel 3 (530nm)	Auto fluorescence
Channel 4 (635nm)	PpIX fluorescence
Channel 5 (660nm)	For observation of photo bleaching products

The complete optical system setup sketch is presented as in Figure 18.

Ray tracing sketch of the optical system



Optical box design

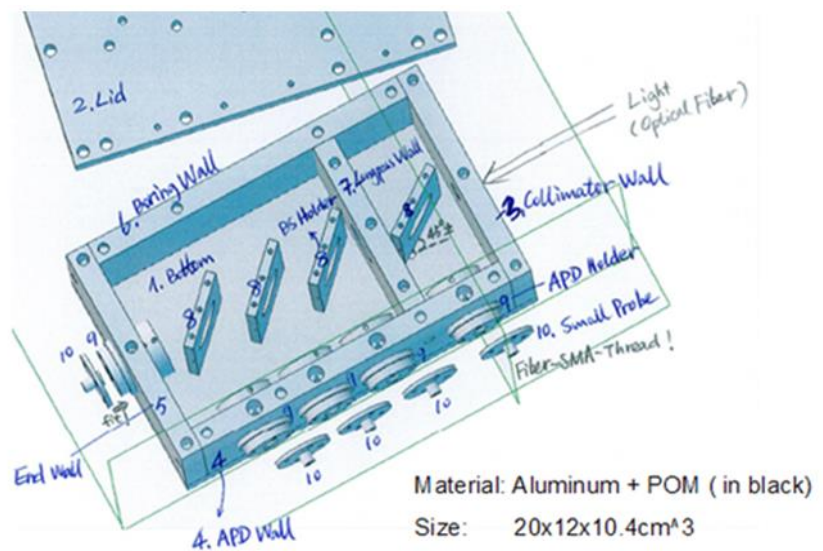


Figure 17 The upper picture is for showing the ray-tracing sketch (Fred) of the optical system in the optical box. The lower picture presents the detail sketch for the optical box [43].

On the system testing stage, light source with only one wavelength output was used. Figure 18 presents the system set up sketch with 405nm diode laser as light source.

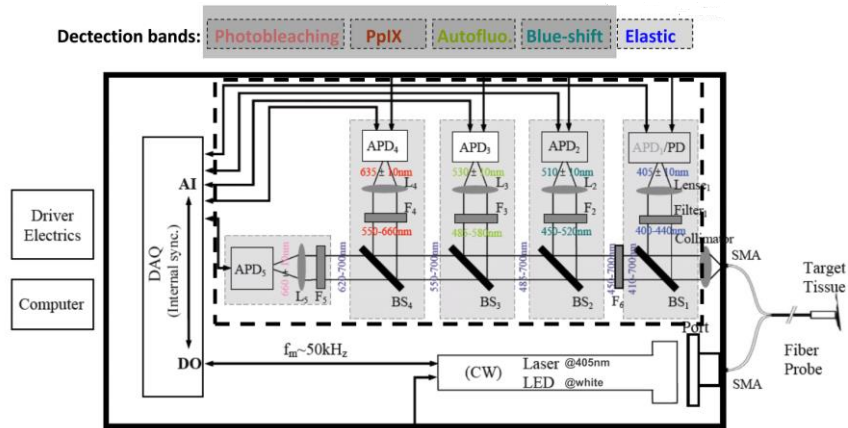


Figure 18 Schematic Diagram of the 2nd generation Optical Touch Pointer system powered with a 405nm diode laser.

In schematic diagram as shown in Figure 19,

1. The optical fiber (Prizmatix Ltd.; Y-shaped fiber patch cord bundle) can be connected to optical box and light source with SMA connectors.
2. The collimators (64770, Edmund Optics) in the design are used for expending the original small incident light spot from the fiber.
3. The beam splitters 1-4 (DMPL425, 505, 567 and 638, Thorlabs) are for directing part of the light to fixed channels located on the side wall of the optical box. At the designed wavelengths the transmittance efficiency is supposed to be 50% of the incident light.
4. One long pass filter (GG-435, Edmund Optics) is set for lowering the reflected light power from tissue after the 405nm channel. When the intensity of reflected light is too high, it will cause high noise in other channels.

5. The band pass filters 1-5 (FB405-10, FB470-10, FB530-10, FB-635-10, and FB-660-10, respectively) are located in the front part of the plastic tubes. The use of them is to sort out target wavelengths before sending in to the detecting components.
6. In each channel after the band pass filter there is one focus lens (47884, Edmund Optics). This lens is for focusing the expended light spot to match the detectors' detecting area.

Design with Multi-LED source

In the later stage of the project, the system light source is gradually changed to LED light sources. As mentioned in Chapter 4, LEDs are more compact and robust light sources, and they are preferred in clinical use.

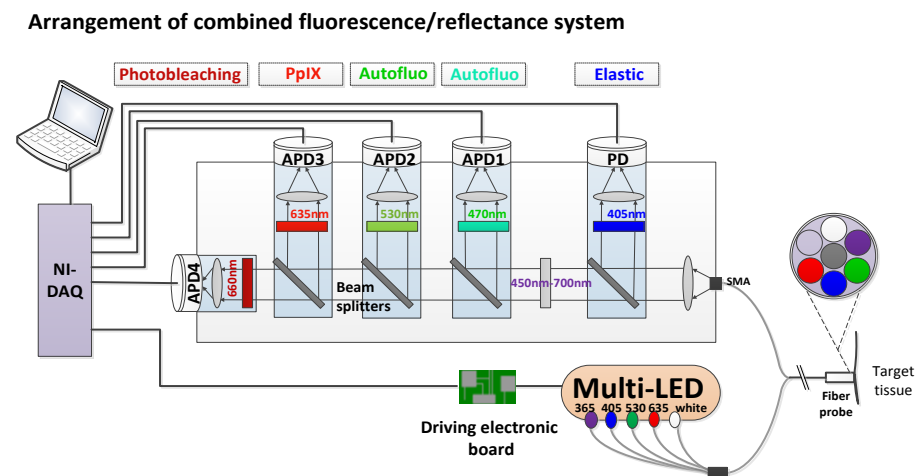


Figure 19 Schematic Diagram of the 2nd generation Optical Touch Pointer system powered with multi-LED source.

The multi-LED source includes 5 LEDs with different wavelengths: 365 nm, 405 nm, 530 nm, 640 nm and white. These 5 different LEDs are linked to individual fibers to illuminate the tissue surface. Apart from these the other parts of the system remain the same.

In this multi-LED source, 365 nm-LEDs is used to excite tissue auto-fluorescence and 405 nm-LED is for generating PpIX fluorescence with an intensity peak at 635 nm. The other three LEDs (530, 640 nm and white) are used for monitoring tissue diffuse reflectance. This could potentially be used for monitoring of tissue optical properties.

In this thesis, most experiments and testing are done with only 405 nm LED as light source. The system function testing with multi-LED source is still in progress.

5.2 Signal processing methods

In order to eliminate or reduce the influence due to ambient light, the light source is designed to be powered with either square wave or sine wave. In this case, two different signal processing methods were developed to cooperate with those two powering methods.

5.2.1 Square wave modulation method

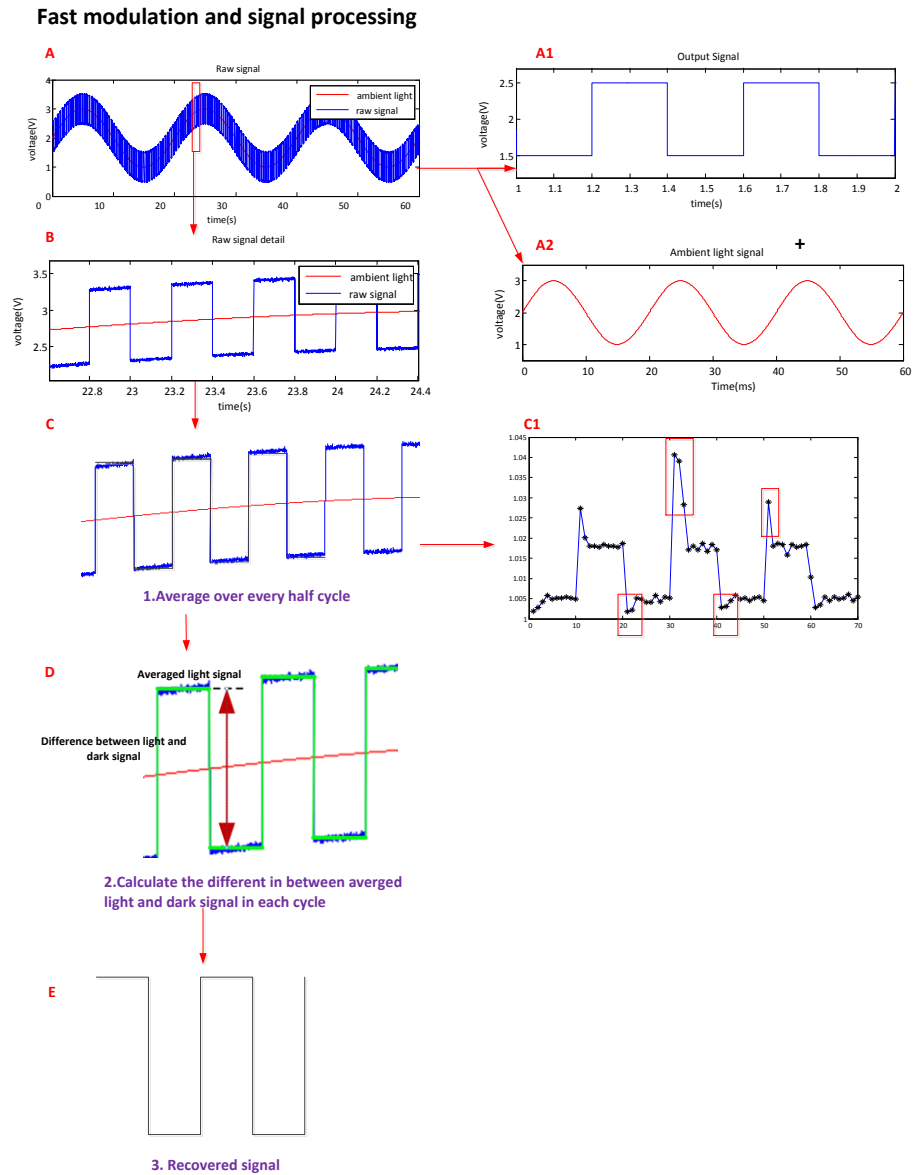


Figure 20 Square wave modulation and signal processing.

To explain the details of the sub figures in Figure 21,

(A) Shows the raw result signal. It consist the high frequency light pulses as shown in (A1), the 50Hz

ambient light signal (A2) and some noise signal. The pulses shown in (A1) are generated from DAQ-card modulated LED light source.

- (B) Shows the details of raw signal (A), in order to present the signal processing clearly, the following process are performed based on this figure. From the figure one can tell, if the modulation frequency (A1) is high enough, the intensity shift on y-axis in figure (B) should be quite small.
- (C) Shows the main signal suppressing process. The raw data is averaged over every half cycle. If enough data points in each half cycle can be processed in the calculation, the white noise and other high frequency noises can be almost suppressed. Unfortunately, the signal in reality looks like in figure (C1), this is due to the operational amplifier's property, a high signal peak appears when there is a signal rise. In order to obtain the best result, the data points consist in these signal peaks are taken away before other processes.
- (D) Shows the signal compensation process. Similar to the 1st generation OTP system, according to Equation 2, the compensated signal result is obtained.
- (E) Shows the final recovered signal. In the optimal situation, the output signal should be noise free and stable.

5.2.2 Sine wave modulation method

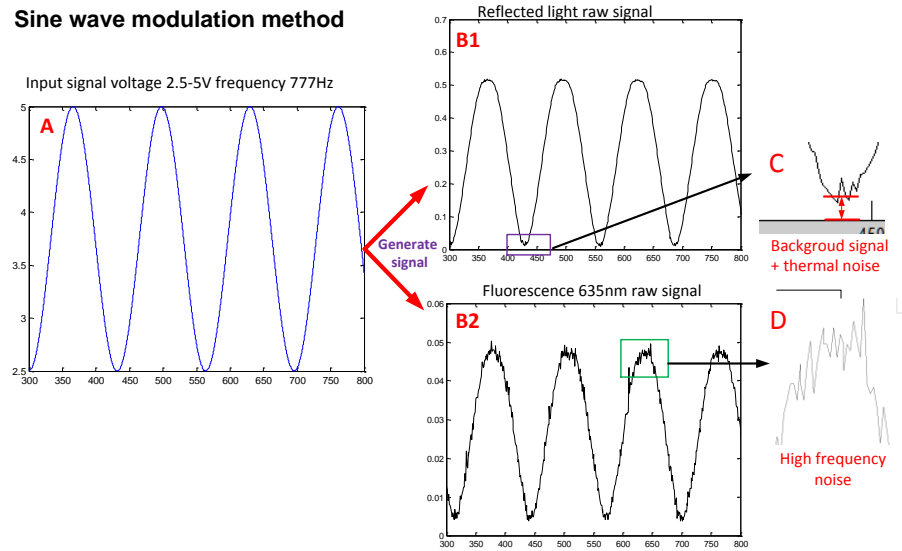


Figure 21 Sine wave modulation method and signal processing

The system is first tested with the ‘square wave modulation method’, the system sensitivity and ambient light suppressing ability of the hardware is proved to be good, the detailed testing methods and results are introduced in Chapter 6. An alternative approach was developed in order to reduce the ambient light influence, named the ‘sine wave modulation method’ was developed. By using this method the noise in the input raw signal can be removed through a Fourier transform of the signal. Although this process requires relatively longer integration time to collect enough data points for obtaining accurate Fourier transform results, it simplifies the whole signal processing method. This method is more direct to explain to other users and for the developers, it also offers an extra choice of applying either hardware or software filters in the system for getting better signal results. In the ‘square wave modulation method’, such filters could not be used, since a

square wave is a combination of different frequency waves. When a square wave is passed through a filter, the signal will get distorted.

The detailed sine wave signal processing method is shown in Figure 21.

(A) shows the DAQ-card output signal for powering the LED source. In the figure the signal strength is 2.5 V-5 V with modulation frequency 777 Hz. To power the LED in this voltage range is due to the LED working voltage barrel meaning the LED source cannot be lit up unless the input voltage is over 2.5 V. This is a specific built-in hardware problem from the light source manufacturer.

(B1) shows the raw signal result from the 405nm back scattered light wave. It has a much higher intensity than fluorescence light signal as shown in (B2).

(B2) shows the 405 nm LED generated fluorescence (635 nm) raw signal result.

(C) shows the lowest signal intensity of back scattered light can't reach 0 V. This is due to the thermal noise from the APD/PD and possible ambient light intensity.

(D) shows the high frequency noise signal exist in the detected raw signal.

The output signal can be defined by,

$$V_o = A \cdot V_i + V_{DC} + \textit{noise} \quad (14)$$

In Equation 14, V_o is the sum of the attenuated input signal, noise signal and a DC component. Figure 22 presents the Fourier transformed result of fluorescence signal result.

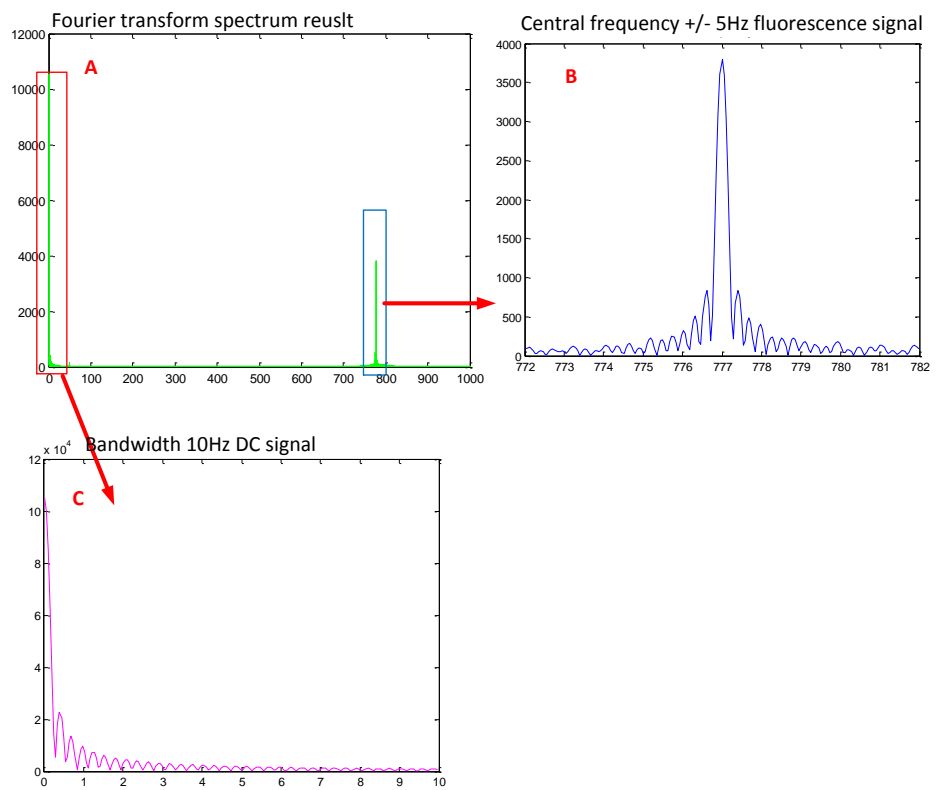


Figure 22 Fourier transformed spectrum plots of the generated fluorescence raw signal

In Figure 22,

(A) shows the full spectrum obtained from Fourier transformed fluorescence raw signal. In this figure, only two obvious peaks (locate at 0 Hz, and 777 Hz) can be observed, they present the fluorescence signal. At the times of 50 Hz (e.g. 50 Hz, 100 Hz, 150 Hz...), signal peaks caused by ambient light can be observed as well. This figure is a plot of the real experiment result, which again proves that the detected signal is not quite influenced by ambient light.

(B) shows a close look the signal peak located at the modulation frequency 777 Hz with ± 5 Hz bandwidth around central frequency.

(C) shows the DC component of the detected fluorescence signal correspond to Figure 22 (C).

The same processes are applied on reflected light signal. Fluorescence and reflectance intensities are retrieved by integrating the peak in (B), within the interval ± 5 Hz around central frequency on both fluorescence spectrum and reflection spectrum. They are named I_f and I_r , respectively.

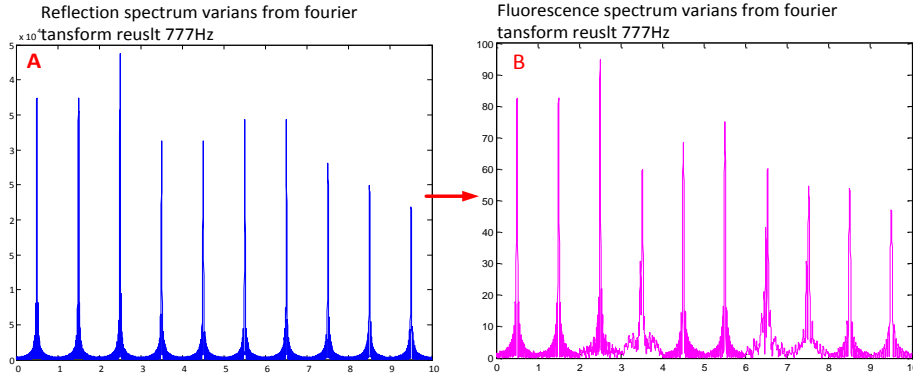


Figure 23 (A) shows 10 groups of Fourier transformed results obtained under the same experimental condition. One can see some fluctuation of reflected light intensity occurs in these results, this is because the LED light source output is not quite stable.

Since both fluorescence and reflectance are influenced by the same light fluctuations the following formula was used to eliminate the light source variations.

$$I_n = I_f / I_r \quad (15)$$

Effectively, this is a normalization of the fluorescence signal by the reflected light.

5.3 System hardware design and components selection

5.3.1 Light source

Laser diode light source and signal LED light source

The light sources are controlled in a computer interface created with LabView 2012 (National Instruments Inc., USA) through the signal in/out device DAQ card (USB-6351, National Instruments Inc., USA). The laser diode output laser power can be controlled by a variable resistor. This design is needed for avoiding detector saturation.

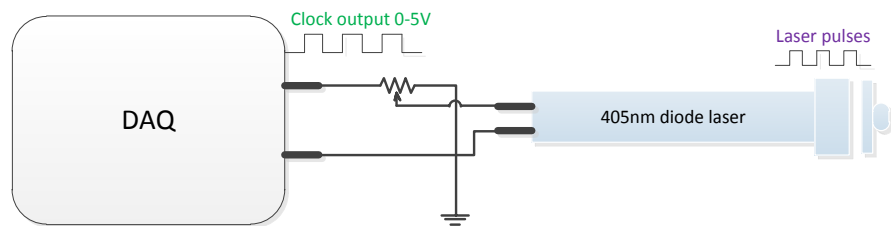


Figure 24 Tunable intensity diode laser electrical circuit powered through the clock output from DAQ card.

For single LED source (405 nm) (FC-5, Prizmatix Ltd.), this LED is one of the LED channels from the multi-LED source which would be shown in the next part in detail. Due to the internal electrical circuit design, extra power tuning components would influence the off-state of the light source, which means the LED cannot be totally turned off. So this light source is linked in the same way as in Figure 25 without the extra variable resistance.

Multi-LED light source

Multi-Led source and multi head fiber budle

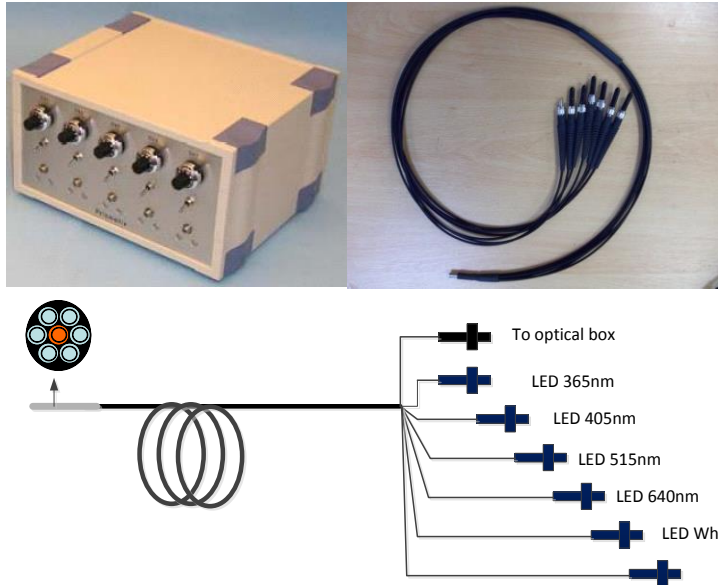


Figure 25 Multi-led source and multi-head fiber bundle specialised used for the led source

As shown in Figure 25, this Multi-LED source include 5 different LEDs, in order to run the multi-LED source properly, there are two different operating methods made.

1. Pulse each led individually for certain amount of time in order to get enough data for processing. This might result in long data acquiring time for running all LEDs.
2. To turn each led on once sequentially, this would speed up the process.

Light sources output power arrangement

Table 4 Laser Diode/Multi-LED source output power after optical fiber transmission

Light source type	Wavelength	Output power (after fiber)
LD	405 nm	3-10 mw
LED	365 nm	10 mw
	405 nm	8 mw
	530 nm	8.2 mw
	635 nm	10 mw

In Table 4 the noted the output powers of 405 nm Laser Diode and each LED light sources after optical fiber transmission. From the table one can tell the real light power of LED light source is not much lower than laser diode, which means the challenge of changing the light source in the system is not on the decrease of light power

5.3.2 Transmission fibers

In the system, two types of optical fibers are used for matching the two different light sources that were used. For the laser diode, as only one light source was used, a bifurcated fiber was chosen. For matching the multi-LED source, a fiber bundled contains 6 light delivering fibers and one collecting fiber was applied.

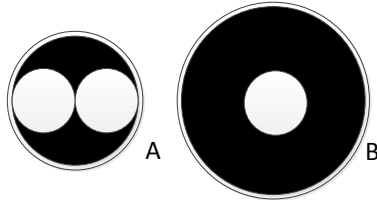


Figure 26 Bifurcated fiber used to deliver laser light and collect fluorescence and reflectance. (Fiber Patch Cord Bundle, Ltd company)

Bifurcated fiber for LD

Figure 26 (A) shows the end with both delivering fiber and collecting fiber. End (A) of the fiber is for touching the tissue, so around the fiber tip a hard jacket outside was special designed for obtaining some extra fiber strength. While the other two ends as shown in Figure 26 (B), they are built with SMA connectors. The core diameter of the fiber is 1000 nm.

Fiber Patch Cord Bundle for Multi-Led source

As shown in Figure 25, the fiber bundled (Fiber Patch Cord Bundle, Prizmatix Ltd.) is constructed of one collecting fiber in the center and 6 other delivering fibers. These fibers are with 750 nm diameter and a length of 4m, with NA 0.5. At the end of the bundled there is a 5 cm long hand-held probe made from iron.

5.3.3 Detecting components designing method

In the project, 4 APDs (S9075, Hamamatsu) and one PD (53378, Edmund Optics) were chosen as light detecting units. To amplify the output signal from these components, an operational amplifier is used. Apart from considering the amplification power of the electrical system, the response frequency of the system should be considered as well. The electric circulars for these components are presented as in Figure 27.

The four paths multi-amplifier LM324 is the operational amplifier used in the project. The reference voltage input to the LM324 is tunable from 1 V to 5 V. This setting makes it easier to view the amplified waveform from LabView program front panel.

Due to the detector capacitor C_d the full signal will swing across it, so the output rolls off at

$$f_{(RC)} = \frac{1}{2\pi R_L C_d} \quad (16)$$

The capacitance C_d of the chosen PD and APD are 300 pf and 30 pf respectively. With these data acquired from data sheets, a plot can be made according to frequency response for different value of applied resistant R_L .

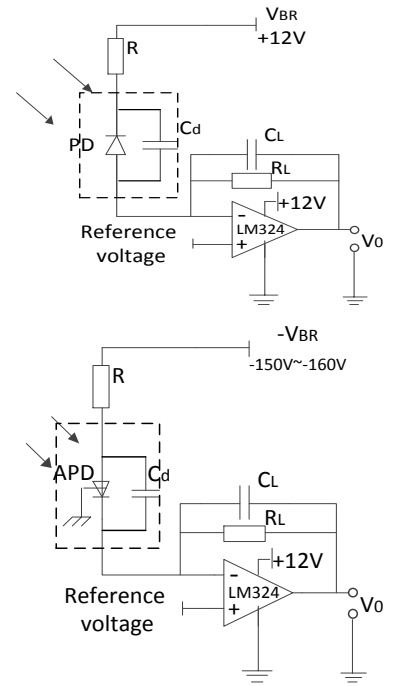


Figure 27 APDs and PD port in circular design

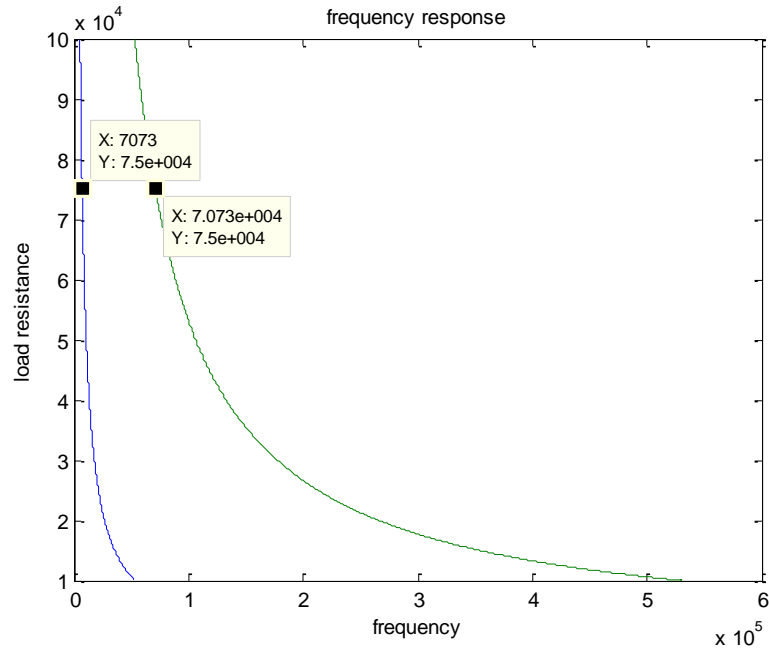


Figure 28 Frequency response of APD and PD used in design.

Assume the current generated from APD and PD are $1 \mu\text{A}$ and $3 \mu\text{A}$ respectively, as reflected light intensity should be much stronger than fluorescence light. If a resistance of $75 \text{ k}\Omega$ was chosen as R_L for both APD and PD it would first ensure the same amplification power for both APD and PD output. Second, it ensures efficient dynamic range and bandwidth of the output. With this design, the SNR loss of the system can be controlled around 1 dB, and response frequency is can reach over 7 kHz, this would allow the sufficient system ambient light rejection according to the design by Hobbs, Philip C. D. [44]. C_L is set to be 10 pf in order to suppress the current swing across the detector capacitance C_d .

5.3.4 Input/output ports

To do proper sorting of all electrical input/output ports is an efficient way to organize the system. When electrical problems

occur, or when the system is moved to other locations, Table 5 works as a fast check list.

Table 5 Input/ Output ports summary of 2nd OTP system

Input		Output	
APD 1-4	DAQ A1-A4	Clock pulses for diode laser	DAQ clock0(0-5 v)
PD	DAQ A0	Diode laser	220 v
		Lm324 amplifier (3pieces)	12 v
		Lm324 reference voltage	2 v
		APD bias voltage power supply (m6017) supply voltage	5 v
		M6017 gain control voltage	0-3 v
		APD bias voltage(from m6017)	-5 v— -200 v
		PD bias voltage	12 v

5.4 Software design

Software design in this project consist two important parts: Labview programming and Matlab programming. Labview is used to programming the operating system interfaces and implement the signal generation and basic signal processing. The Matlab programs are used for further analysis of the experimental data.

Detailed software designs can be found in Appendix.

5.4.1 Labview programming for square wave modulation

LabVIEW (Version 2011, National Instruments) is used for developing the system interfaces. On the interface, the real-time signal processed results are shown, and also the real-time raw signal results are shown in waveform.

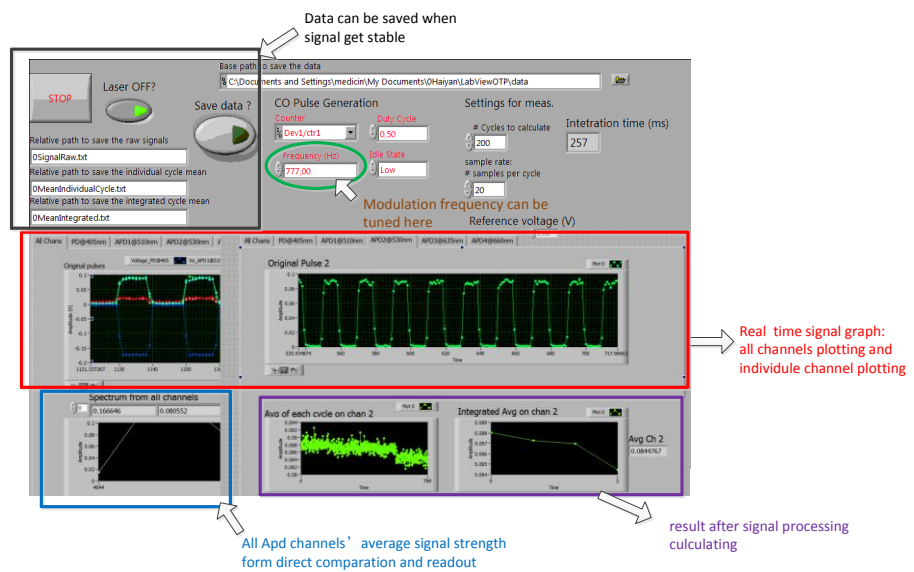


Figure 29 Front panel of the OTP system LabView program for square wave modulation

On the front panel as shown in Figure 29, the light source modulation frequency, integration cycles' number and sample rate are all adjustable. All processed data can be saved in individual folders for further data analysis.

5.4.2 Labview programming for sine wave modulation

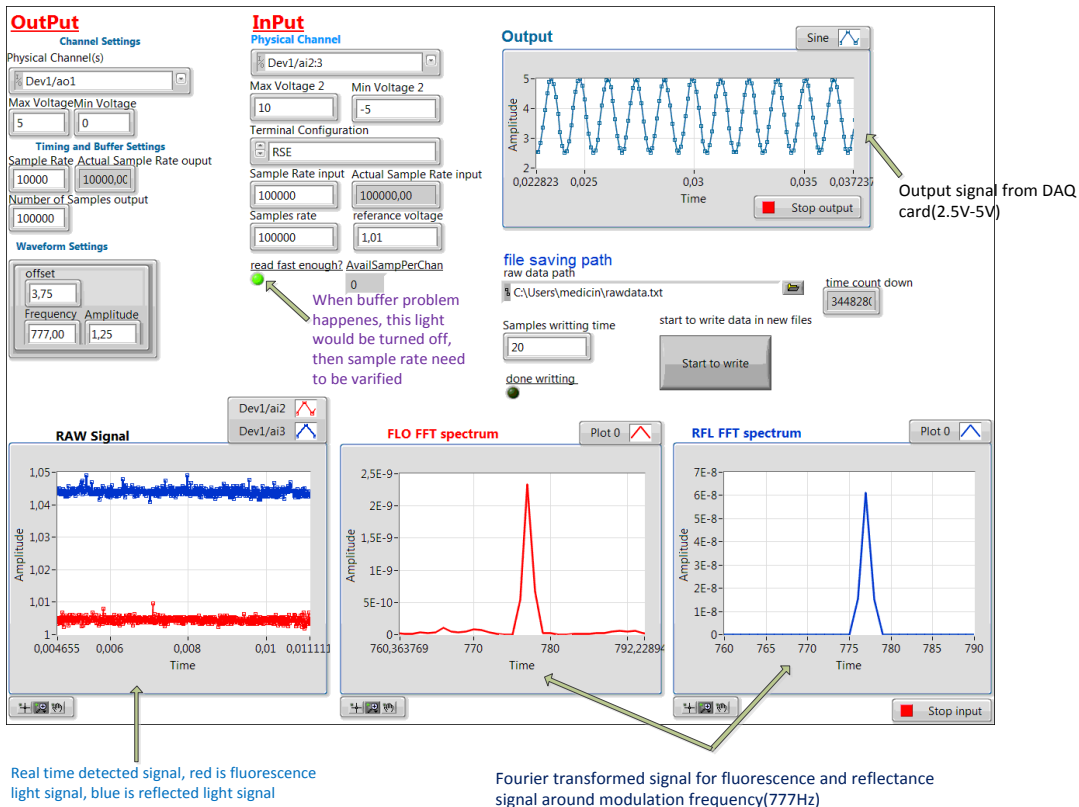


Figure 30 Front panel of the OTP system LabView program for sine wave modulation

In this design as shown in Figure 30, the output modulation signal for light source can be adjusted. In addition, real-time Fourier transform results can be shown.

In this design a common problem in Labview called ‘buffer problem’ is solved. The ‘buffer problem’ problem is caused by the mismatching of system processing speed and data collection speed. This mismatching can cause some errors in signal processing, and influence the evaluation of the system

performance. To solve this problem an indicating light was set. When the program is running normal, the light would be on all the time, and when the ‘buffer problem’ happens, the light would be turned off. At the same time the auto data writing would be stopped to make sure there are no erroneous data include in the final results. One can adjust the system sampling rate to solve the problem.

5.4.3 Matlab program for evaluating the measurements’ results

In Matlab programming, sine wave progressing programs and square wave processing programs are made separately. With these programs, several goals are achieved

1. These programs can process data fast for analysis. The program can read files from over 100 folders in short time, and process these data with high speed later as well.
2. These programs are simple to use. Most of the programs are built as Matlab functions, with simple calling syntax the programs can be used. This allows the analysis to be done simultaneously by several persons even they might not know the details of the programs. This speeds up the final data analysis stage.
3. These programs can be reused in the future analysis. As the multi-LED source would be used in the future, and more system testing would be performed, these programs can be reused in the future with very tiny modifications.

Detailed program codes are attached in the Appendix.

5.5 System construction

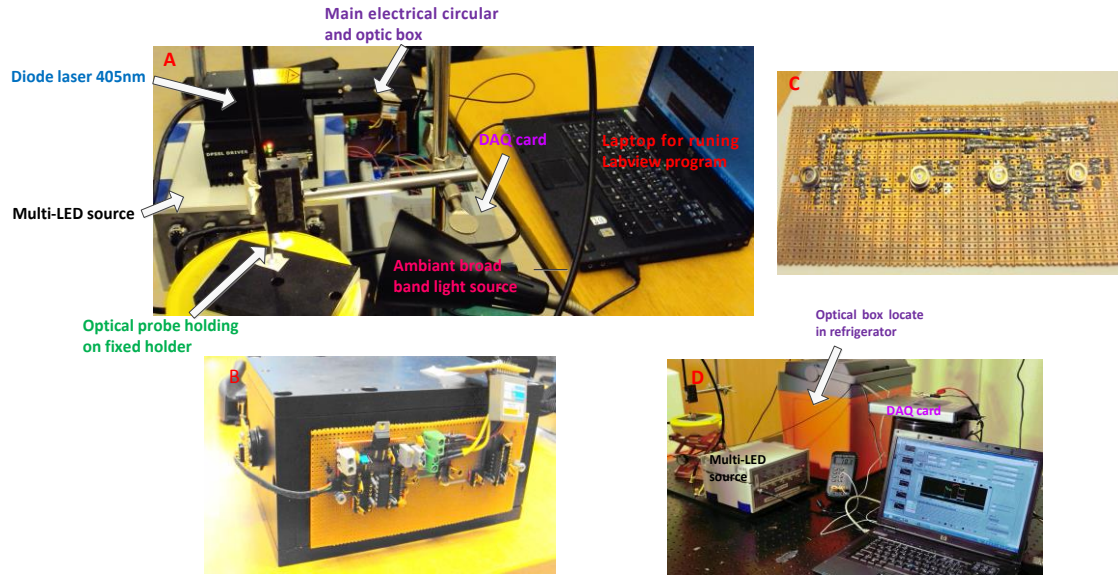


Figure 31 Final system hardware set up. (A) The view of the full system (B) Detailed view of the optical box, the designed electrical board is attached and fix at the side of the optical box, most connecting cables and components are portable (C) The view of electrical board from back, the orientation of APDs is based on the geometry of the optical box, so the APDs and PD can be inserted into the holes aligned on the side of the optical box wall (D) The view of the full experiment system setup on the optical table

In the final stage, linking up the assembled instruments is not the only job. In addition, manufacturing the electrical board to match the geometry of the optical box, as well as adjusting and aligning the optical components are part of the system assembly. As shown in Figure 31(B), the electrical board can be closely fixed on the side wall of the optical box, and all amplification components are located on this piece of board.

Several editions of the electric boards were produced in the past year. In this final version, the electrical board is made almost double sided, and most of linking cables and

components are portable, this allows fast system assembly the system is moved to other locations.

The electrical board developed for this system has now been used in many experiments under rather long time. It has so far worked reliable, and it can thus empirically be concluded it works in a stable manner.

System capacity test

6.1 System calibration

6.1.1 Calibration method

Inside the optical box, light is passing different optical components causing some intensity loss. In order to present the true signal value from each channel, system calibration was done.

A high power broadband calibration lamp (63355, Oriel) was used for calibrating the system, and this lamp has a calibrated spectrum intensity documents attached. When power the lamp with 6.5A current (68830, Oriel), the lamp would shine with a broadband spectrum shown in Figure 32.

Light from this calibration lamp was collected with a fiber fixed 5 meters away from the lamp and guided to the optical box. The system recorded the signals for the various detection wavelengths. By normalizing all these signal strengths to the 405nm channel one obtain the result 1, A1, A2, A3, and A4 for the different channels, respectively.

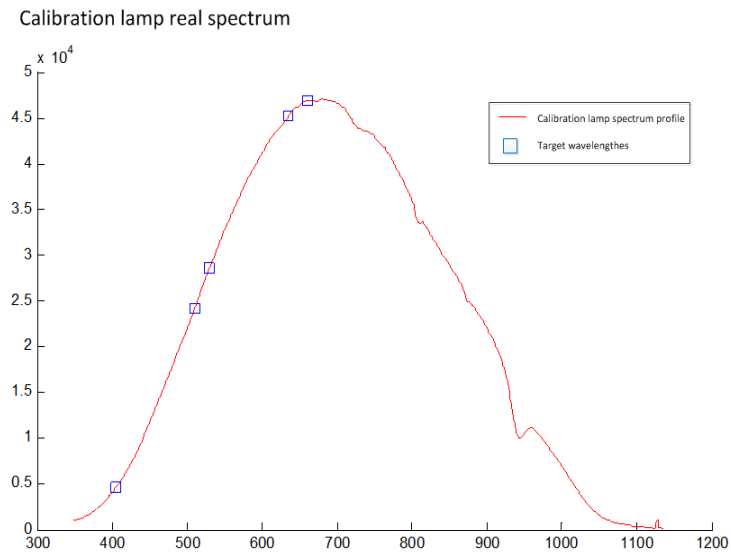


Figure 32 The plotting of calibration lamp real spectrum

In Figure 32 the true spectrum profile of the calibration lamp are plotted. By picking out the intensity values at corresponding wavelengths (405 nm, 510 nm, 530 nm, 635 nm, 660 nm) from the calibration lamp profile and do the same normalization, results 1, S1, S2, S3, S4 are obtained.

The calibration factor can be calculated from dividing the normalized signal with the corresponding result from lamp spectrum,

$$f1 = S1/A1. \tag{17}$$

6.1.2 Calibration result and analyses

Table 6 OTP system calibration result

Wave length	Calibration factor f
405	1
510	5.2652
530	6.2252
635	9.8197
660	10.1885

These parameters in Table 6 would then be stored in the program and all subsequently recorded signals will be corrected for this sensitivity. The system interface will thus present calibrated data only.

The variations in the calibration factors are caused by different light intensity losses in the light paths, the detector sensitivities at the different wavelengths, and by the amplification power of the electrical circular and APD gain differences. This means the light intensity from the last two channels might be weak after losses in multiple dichroic mirrors. As the 635nm channel is the PpIX characteristic fluorescence channel which is of high importance for tumor detection, a high loss in this detection would influence the system sensitivity in detecting PpIX signals.

The system tests presented below shown a quite satisfying system performance and sensitivity. On the other hand, it can be interesting to increase the system sensitivity by optimizing the band pass filters and other optical components in the future.

6.2 System ambient light resistance ability test

As explained in Chapter 2, the ability to suppress the ambient light in the detection is one of the most important capabilities of the system. So tests were done for two modulation methods individually.

As 405nm generated PpIX characteristic fluorescence wavelength is 635 nm, so only experiment data from 635 nm channel was studied in this stage.

6.2.1 Ambient light resistance ability test method

The ambient light source used in the test is a ring light guided by fiber from a lab use microscope lamp. The system probe was arranged in a fixed position in contact with the sample, vertically in the center of the ring light. The ambient light condition was varied by shifting the height of the ring light position. A photometer was positioned under the fiber tip for each position of the ring light, so that the ambient light level could be quantified. The ambient light level was adjusted such that the luminance reads outs from photometer were 15, 23, 30, 50, 70, 120, 200, 600, 1500, 2300 Lux (lm/m²).

In the tests, liquid phantom with high PpIX concentration was used as the experimental sample. The phantom sample recipe is shown below in Table 7.

Table 7 Phantom recipe for the ambient background ring light testing

Phantom content	Quantum
Water	192 ml
Intralipid (20%)	7.3 ml
Ink(1:100)	0.5 ml
Tween	3 ml
Ppix	100 nm

To give a short introduction of the phantom, intralipid provides certain light scattering property of the phantom, and ink is for providing light absorption property. Thus this mixture of water, intralipid and ink makes a sample with optical properties similar to those of real human tissue. The fluorophore PpIX is added to yield fluorescence signal from the phantom. In addition, tween is added to the mixture to avoid PpIX aggregation in the phantom, as the aggregation would alter the fluorescence properties.

6.2.2 Ambient light suppression ability test result

In Figure 35 the results of the system sensitivity to ambient light measurements are presented. From the figure, one can tell both sine wave and square wave modulation work well with the principle of lock-in detection, this permit the background light can be directly and accurately subtracted from the final signal as described in chapter 5.

System background sensitivity result

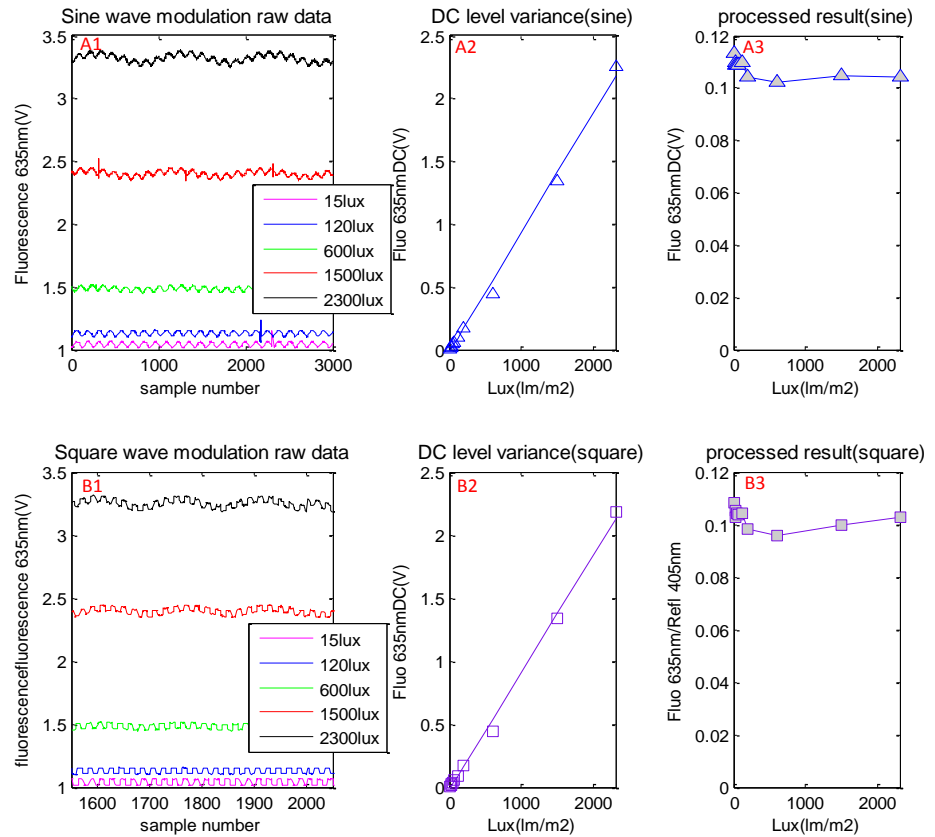


Figure 35 Ambient light suppression ability test result. In the upper row of figures (A) the results from sine wave modulation is presented, while the results from square wave modulation are presented in the lower row (B). The left hand figures demonstrate the raw signal intensities as a function of time. The graphs in the middle illustrate the averaged signal levels, while the right-hand graphs show the fluorescence signals with the ambient background light subtracted.

In Figure 35,

Figures A1 & B1 illustrates the sine/square wave modulation method detected raw signal measured from the 635 nm channel. The raw signals are obtained with a reference voltage of 1.00 V, which is applied on the operational amplifier as mentioned in chapter 5. This explains why all the signal levels are above 1 V. From these two figures, it is obvious that the raw signal

levels increase with the ambient background luminance. One can also observe a high modulation frequency from the LED induced fluorescence as well as a 50 and 100 Hz modulation frequency from the ring light power supply.

In figures A2 and B2 the actual DC levels are plotted depending on luminance power for the sine and square wave modulation methods, respectively. The solid lines in the figures are linear fitted curves for independent result points. The added reference voltage is subtracted from the presented results. In these two figures, the DC level increase almost identically as expected. This means that the background light is detected equally efficiently, independently on how the LED was modulated, as the exact same detector in the same geometry was utilized independent on modulation scheme. .

In figures A3 and B3, it provides the resulting signal intensity change, ambient background light signal have been subtracted from the two modulation schemes, respectively. These plots are thus presenting the results after the full signal processing as mentioned in chapter 5. The solid lines represent the linear fits to the result data points. These two figures again show extremely high similarities between the results from the two modulation schemes. From the figures one can understand that the background suppression is very efficient for both techniques, and the background light only influences the final signal to a small extent (4.5% maximum variance). The slight variation in the final result may be due to that the PpIX was unevenly dissolved, indicated by that the same variations is present simultaneously for both methods.

Thus, both processing methods can achieve almost ambient light influence-free fluorescence detection.

6.3 System fluorescence sensitivity test

If the previous subchapter concerned the signal-to-background ratio and how to suppress the background in an optimal way, we will here be concerning the signal-to-noise ratio of the system. It is important to increase the signal-to-noise ratio, as this is directly related to how low concentrations of tumor cell that can be detected. As mentioned in chapter 1, a high sensitivity would enable to maximize the tumor remove ratio and thus the outcome of the surgical resection would be optimized.

Similar to the last experiment, data analyzing was only done with 635nm channel results.

6.3.1 System fluorescence sensitivity test method

In order to measure the sensitivity of the system, a series of tissue phantoms with low and various amounts of fluorophore concentrations were produced. By evaluate the detected the fluorescence light signal level, the sensitivity of the system can be shown. The tissue phantom used in the tests was based on the water phantom. Measurements started on a phantom with relatively high PpIX concentration. The PpIX concentration in the phantom was diluted by gradually adding in more of plain phantom material without any fluorophore, thus these experiments are called: the ‘dilution experiment’.

The experiments were conducted in a dark room without any ambient background light.

Two series of experiments were conducted to test the sensitivity of the system. The experiments were divided as:

1. Sensitivity comparison of two different modulation methods in dilution experiment with an ink-based phantom.
2. Dilution experiment with a cow-blood-based (instead of ink) phantom for square wave modulation.

In the second group of dilution experiments, cow blood replaced the ink as the absorption ingredient in the phantom. The reason is that cow blood absorbs differently depending on wavelengths, while ink absorbs about the same independent to the wavelength. Therefore cow blood offers a tissue phantom with optical properties more closely resembling the properties of real tissue.

The recipes of the tissue phantoms used are list below in Table 8 and Table 9.

Table 8 Ink phantom

Phantom ingredients	Amount
Water	192 ml
Intralipid (20%)	7.3 ml
Ink (1:100)	1 ml
Tween	3 ml
Ppix	0, 6, 8, 16, 20, 25, 33, 40 50, 55, 62, 71, 83, 100 nm

Table 9 Blood phantom

Phantom ingredients	Amount
Water	1920 ml
Intralipid (20%)	73 ml
Blood	1%, 2%, 3% ml
Tween	40 ml
Ppix	0, 100, 200, 300, 500, 700, 1000 nm

6.3.2 System PpIX fluorescence sensitivity test results

PpIX dilution experiment results

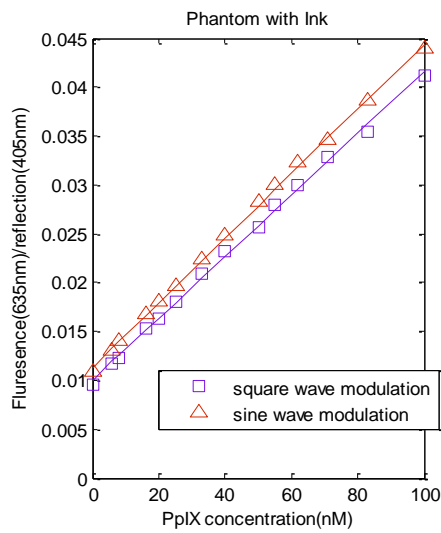


Figure 3 Sensitivity test result with the ink phantom with sine and square wave modulation methods

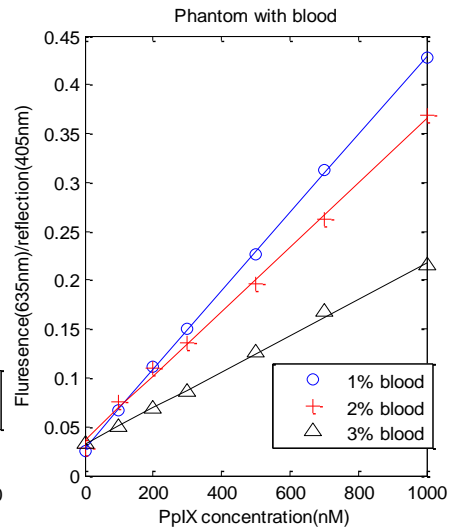


Figure 4 Sensitivity test result for the blood phantom with square wave modulation methods

The system sensitivity testing results with the ink phantom are presented in Figure 34, while the results for the blood phantom are shown in Figure 35. In these figures the solid lines are the linear fitting of corresponding data points. With the PpIX concentration increasing, great linearity is shown on the fluorescence signal intensity for both methods. The slightly higher value for sine wave modulation method might due to the fluorophore bleaching, as the experiment of sine wave modulation method was done first. Despite the lowest PpIX concentration used in the dilution experiments is lower than the clinical relevance, the sensitivity limit of the system was still not reached, meaning the signal-to-noise ratio still seems to be acceptable at the lowest PpIX concentration for both modulation schemes. From this figure we can see that the system sensitivity for both modulating methods is good, even with low PpIX concentration, the signal can be detected by the system and analyzed efficiently.

In order to execute further evaluation the performance of the system in a more realistic situation, blood-based phantoms provide a much worse measurement condition due the high absorption property. This can be seen by comparing the results presented in Figure 34 and Figure 35, in particular by comparing the signal levels for a specific PpIX concentration. A phantom with 10 times higher PpIX concentration in Figure 34, provides a fluorescence intensity increased less than 10 times the value given in Figure 35.

With different blood concentrations, the great linearity remains between PpIX concentration increasing and fluorescence intensity growth. And with high blood concentration (3%) even with around 50% decreasing on

fluorescence signal level can be seen, but the fluorescence signal level changing is still quite sharp and clear in the low PpIX concentration region.

These results prove that the system possesses excellent sensitivity, and the original designs of the system are all achieved.

Discussion and conclusions

7.1 Future works

As introduced in chapter 6, the system is tested in several laboratory experiments with liquid phantom, also it is proved to have stable performance and high sensitivity to low PpIX concentration under strong ambient light sources. The next step is to test the system in clinics on superficial skin cancer at Skåne University Hospital in Lund and later in Glioblastoma surgeries at Linköping University Hospital. Analysis of the ability to distinguish different tissue types will be conducted utilizing multivariate calibration techniques, and such studies are planned.

As shown in Figure 36, some clinical tests have started in Skåne University Hospital in Lund from May 2013. These data will be analyzed and more studies will be performed in the near future.

System clinical test on PDT treatment patient 2013.05.22



Figure 36 Clinical test of the system on a PDT treatment patient. This patient has a 3cm*4cm lesion on her forehead. Measurements were done before and after PpIX cream applied, and after the PDT treatment.

7.2 Conclusion and outlook

The second generation optical touch pointer system (new OTP system) is developed for assistant efficient glioblastoma tumor resection in clinical surgeries. The concept of the system is to distinguish the tissue types by combining information from tissue auto-fluorescence, fluorescence from the contrast agent ALA-induced PpIX, as well as diffuse reflected light. As malignant glioma cells will take up ALA as a consequence of a damaged blood-brain-barrier in tumor tissue, and be converted it into strongly fluorescent protoporphyrin IX (PpIX). The PpIX concentration in the tumor can reach 50 times the

concentration in the surrounding brain. With 405nm excitation light, the PpIX would fluorescence intensively around 635nm.

As established in the thesis, the system act stable under intensive ambient light luminance, at the same time the system appears high sensitivity to low PpIX concentration even in high light absorbing surrounding. At the same time the original desire for a high efficient, compact and robust system is achieved by delicate designing of electronic circular. Meanwhile the powerful LabView program and the friendly and simple interface ultimately simplify the system operation.

As shown in the thesis, although in the final system setup the square-wave-modulation method is adapted, the sine-wave-modulation method acts equally efficient in all the tests. As a matter of fact, the sine-wave-modulation method has the potential to be reused in the future, and may help to develop a faster and simpler system.

Self-reflection

During the work on my thesis project, I have successfully combined my theory knowledge with the experimental work. I also improved my programming, data evaluating, electric circuit designing and writing skills. During the literature researching period, I have obtained more knowledge about modern radiation imaging methods and optical imaging methods. The neurophotonics, biomedical imaging, optical spectroscopy, oncology relevant research becomes really fascinating to me.

Working with more experienced people gives me a different view on practical works. I adapted their good methods of organizing materials for future using and keeping track of

project processes. I have also learnt a lot of tricks for solving practical problems. These knowledges are really valuable as they are not possible to get from lectures, but the enormous amount practical works.

My working content cross between optics and electronics, in Lund University the optical labs are equipped with big amount of optical components and various types of equipments. Working on my thesis project and helping with other projects give me chances to use these components and equipments. When building the system, I have gone through lots of the websites for finding suitable electrical and optical components, meanwhile updated my knowledge of the new products.

Now I am used to plot an 'information net' connecting theory, hardware and software programming in mind before every new step in the project. This net can give me a clear view of how to fulfill the project requirements in an easy and efficient way, at the same time help me make sure that whatever I do will benefit the future works. In the thesis project I have always been looking for methods that are more efficient and accurate. That is the key point of me getting such fruitful and cheerful results in the project.

As a conclusion, I have learnt a lot during the project time, and I am satisfied with the system performance and the final results. I enjoyed the project a lot.

References

- [1] M. Lacroix, D. Abi-Said, D. R. Fournay, Z. L. Gokaslan, W. Shi, F. DeMonte, F. F. Lang, I. E. McCutcheon, S. J. Hassenbusch, E. Holland, K. Hess, C. Michael, D. Miller, and R. Sawaya, "A multivariate analysis of 416 patients with glioblastoma multiforme: prognosis, extent of resection, and survival," *J. Neurosurg.*, vol. 95, no. 2, pp. 190–8, Aug. 2001.
- [2] W. Stummer, a Novotny, H. Stepp, C. Goetz, K. Bise, and H. J. Reulen, "Fluorescence-guided resection of glioblastoma multiforme by using 5-aminolevulinic acid-induced porphyrins: a prospective study in 52 consecutive patients," *J. Neurosurg.*, vol. 93, no. 6, pp. 1003–13, Dec. 2000.
- [3] A. Johansson, G. Palte, O. Schnell, J.-C. Tonn, J. Herms, and H. Stepp, "5-Aminolevulinic acid-induced protoporphyrin IX levels in tissue of human malignant brain tumors," *Photochem. Photobiol.*, vol. 86, no. 6, pp. 1373–8, 2010.
- [4] P. a Valdés, A. Kim, F. Leblond, O. M. Conde, B. T. Harris, K. D. Paulsen, B. C. Wilson, and D. W. Roberts, "Combined fluorescence and reflectance spectroscopy for in vivo quantification of cancer biomarkers in low- and high-grade glioma surgery," *J. Biomed. Opt.*, vol. 16, no. 11, p. 116007, Nov. 2011.
- [5] A. Kim, M. Roy, F. Dadani, and B. C. Wilson, "A fiberoptic reflectance probe with multiple source-collector separations to increase the dynamic range of derived tissue optical absorption and scattering coefficients," *Opt. Express*, vol. 18, no. 6, pp. 5580–94, Mar. 2010.
- [6] N. Haj-Hosseini, J. Richter, S. Andersson-Engels, and K. Wårdell, "Optical touch pointer for fluorescence guided glioblastoma resection using 5-aminolevulinic acid," *Lasers Surg. Med.*, vol. 42, no. 1, pp. 9–14, Jan. 2010.
- [7] F. W. Kreth, P. C. Warnke, R. Scheremet, and C. B. Ostertag, "Surgical resection and radiation therapy versus biopsy and radiation therapy in the treatment of glioblastoma multiforme.," *J. Neurosurg.*, vol. 78, no. 5, pp. 762–6, May 1993.
- [8] J. Markert, *Glioblastoma Multiforme*, Jones & Bartlett Learning, 2005, p.316.
- [9] W. C. Lin, S. a Toms, M. Johnson, E. D. Jansen, and a Mahadevan-Jansen, "In vivo brain tumor demarcation using optical spectroscopy," *Photochem. Photobiol.*, vol. 73, no. 4, pp. 396–402, Apr. 2001.
- [10] J. C. O. Richter, N. Haj-Hosseini, S. Andersson-Engel, and K. Wårdell, "Fluorescence spectroscopy measurements in ultrasonic navigated resection of malignant brain tumors," *Lasers Surg. Med.*, vol. 43, no. 1, pp. 8–14, Jan. 2011.

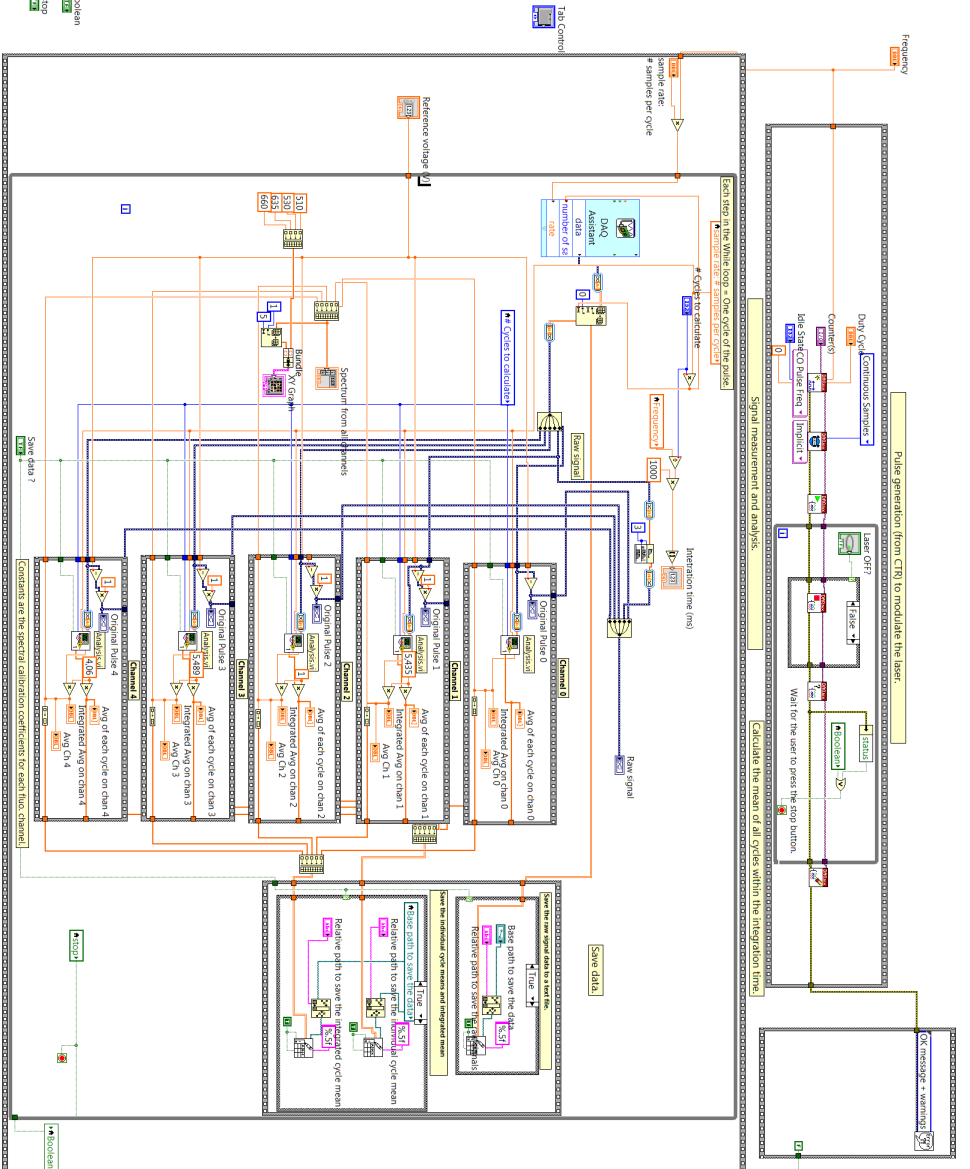
- [11] V. S. Klimberg, S. Harms, and S. Korourian, "Assessing margin status," *Surgical oncology*, vol. 8, no. 1999, pp. 77–84, 2000.
- [12] W. S. Poon, K. T. Schomacker, T. F. Deutsch, and R. L. Martuza, "Laser-induced fluorescence: experimental intraoperative delineation of tumor resection margins," *J. Neurosurg.*, vol. 76, no. 4, pp. 679–86, Apr. 1992.
- [13] S. Koljenovi&ccacute;, "Discriminating vital tumor from necrotic tissue in human glioblastoma tissue samples by Raman spectroscopy," *Laboratory investigation*, vol. 82, no. 10, pp. 1265–1277, 2002.
- [14] L. Marcu, J. a Jo, P. V Butte, W. H. Yong, B. K. Pikul, K. L. Black, and R. C. Thompson, "Fluorescence lifetime spectroscopy of glioblastoma multiforme," *Photochem. Photobiol.*, vol. 80, pp. 98–103, 2004.
- [15] A. C. Croce, S. Fiorani, D. Locatelli, R. Nano, M. Ceroni, F. Tancioni, E. Giombelli, E. Benericetti, and G. Bottioli, "Diagnostic potential of autofluorescence for an assisted intraoperative delineation of glioblastoma resection margins," *Photochem. Photobiol.*, vol. 77, no. 3, pp. 309–18, Mar. 2003.
- [16] S. Svanberg, *Atomic and Molecular Spectroscopy: Basic Aspects and Practical*, Springer, Berlin, 2004.
- [17] R. R. Allison, G. H. Downie, R. Cuenca, X.-H. Hu, C. J. Childs, and C. H. Sibata, "Photosensitizers in clinical PDT," *Photodiagnosis Photodyn. Ther.*, vol. 1, no. 1, pp. 27–42, May 2004.
- [18] S. Andersson-Engels, Elnor, and J. Johansson, "Clinical recording of laser-induced fluorescence spectra for evaluation of tumour demarcation feasibility in selected clinical specialities," *Lasers Med.*, vol. 6, no. 8, pp. 415–424, 1991.
- [19] W. Stummer, a Novotny, H. Stepp, C. Goetz, K. Bise, and H. J. Reulen, "Fluorescence-guided resection of glioblastoma multiforme by using 5-aminolevulinic acid-induced porphyrins: a prospective study in 52 consecutive patients," *J. Neurosurg.*, vol. 93, no. 6, pp. 1003–13, Dec. 2000.
- [20] W. Stummer, a Novotny, H. Stepp, C. Goetz, K. Bise, and H. J. Reulen, "Fluorescence-guided resection of glioblastoma multiforme by using 5-aminolevulinic acid-induced porphyrins: a prospective study in 52 consecutive patients," *J. Neurosurg.*, vol. 93, no. 6, pp. 1003–13, Dec. 2000.
- [21] M. A. Scott, C. Hopper, A. Sahota, R. Springett, B. W. Mcilroy, and S. G. Bown, "Fluorescence Photodiagnosics and Photobleaching Studies of Cancerous Lesions using Ratio Imaging," pp. 63–72, 2000.
- [22] M. Hefti, V. C. G, M. Moschopulos, A. Siegner, H. Looser, and H. Landolt, "protoporphyrin IX fluorescence in high-grade glioma surgery," vol. 8, pp. 180–186.
- [23] K. Wårdell, "Photobleaching-Insensitive Fluorescence Diagnostics in Skin and Brain Tissue Diagnostics in Skin and Brain Tissue," vol. 3, no. 3, 2011.

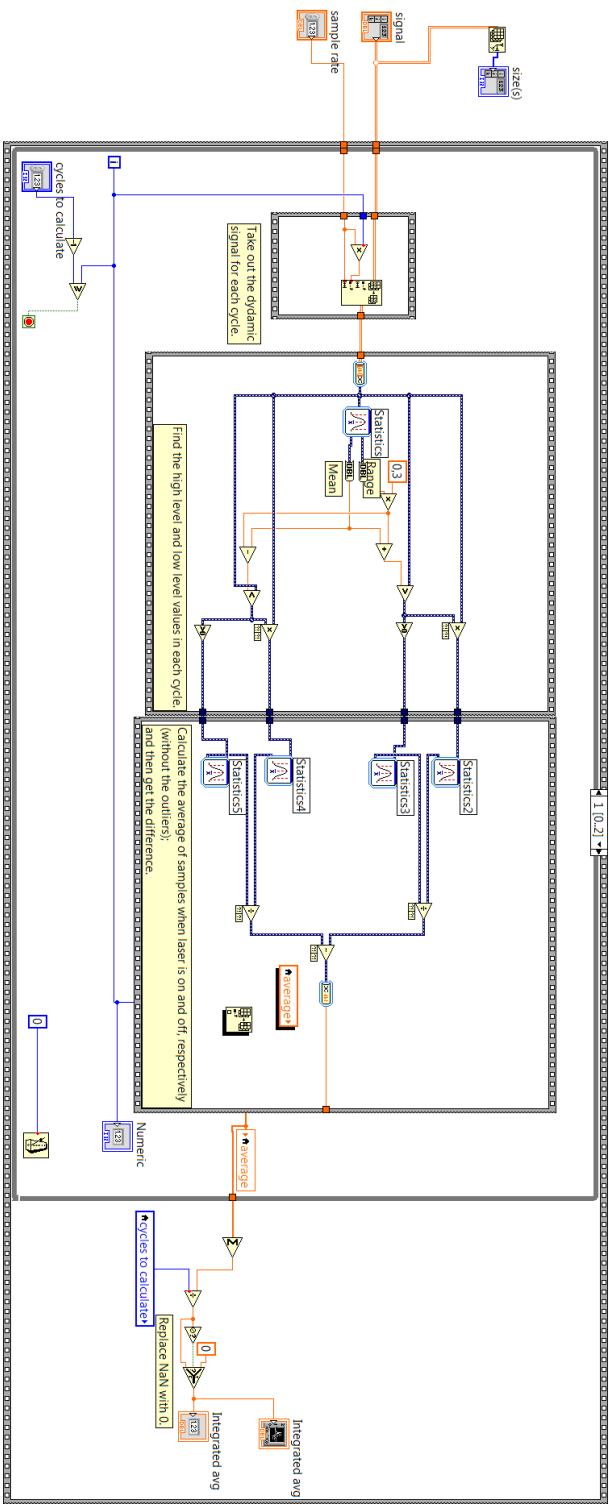
- [24] K. Vishwanath and N. Ramanujam, "Fluorescence spectroscopy in vivo," *Encyclopedia of Analytical Chemistry*, 2011
- [25] C. Klinteberg, M. Andreasson, and O. Sandström, "Compact medical fluorosensor for minimally invasive tissue characterization," pp. 1–7, 2005.
- [26] K. Wårdell, "Evaluation of a Fiber-Optic Based Pulsed Laser System for Fluorescence Spectroscopy," no. Fig 1, pp. 363–366, 2008.
- [27] K. Wårdell, "Evaluation of a Fiber-Optic Fluorescence Spectroscopy System to Assist Neurosurgical Tumor Resections," vol. 6631, pp. 2–9, 2007.
- [28] N. Haj-Hosseini, J. Richter, S. Andersson-Engels, and K. Wårdell, "Photobleaching behavior of protoporphyrin IX during 5-aminolevulinic acid marked glioblastoma detection," *Proc. SPIE*, vol. 7161, pp. 716131–716131–8, 2009.
- [29] N. Haj-Hosseini, J. Richter, S. Andersson-Engels, and K. Wårdell, "Optical touch pointer for fluorescence guided glioblastoma resection using 5-aminolevulinic acid," *Lasers Surg. Med.*, vol. 42, no. 1, pp. 9–14, Jan. 2010.
- [30] N. Haj-hosseini, J. Richter, S. Andersson-engels, and K. Wårdell, "Fiber-optic based fluorescence spectroscopy for glioblastoma demarcation using 5-aminolevulinic acid," *Lasers in surgery and medicine*, vol. 42, no. 1, pp. 9–14, Jan. 2010.
- [31] I. Wang, *Photodynamic therapy and laser-based diagnostic studies of malignant tumours*, doctor of science dissertation, Lund, Sweden: Lund University, February, 1999.
- [32] S. Pålsson, *Methods , Instrumentation and Mechanisms for Optical Characterization of Tissue and Treatment of Malignant Tumours*, doctor of science dissertation, Lund, Sweden: Lund University. 2003.
- [33] Tuchin V V, Tuchin V. *Tissue optics: light scattering methods and instruments for medical diagnosis[M]*. Bellingham: SPIE press, 2007.
- [34] Cheong, Wai-Fung, Scott A. Prahl, and Ashley J. Welch. "A review of the optical properties of biological tissues." *IEEE journal of quantum electronics* 26.12 (1990): 2166-2185.
- [35] T. M. Breslin, F. Xu, G. M. Palmer, C. Zhu, K. W. Gilchrist, and N. Ramanujam, "Autofluorescence and Diffuse Reflectance Properties of Malignant and Benign Breast Tissues," vol. 11, no. 1, pp. 65–70, 2004.
- [36] D. De Veld and M. Skurichina, "Autofluorescence and diffuse reflectance spectroscopy for oral oncology," *Lasers Surg.*, vol. 364, no. April, pp. 356–364, 2005.
- [37] S. Lowndes, *Blood interference in fluorescence spectrum – Experiment , analysis and comparison with intra- operative measurements on brain tumor*, Doctor of science dissertation, Linköping, Sweden: Linköping University, May, 2010.
- [38] P. Use, "Fluorescence-guided Resection of Malignant Gliomas Using 5-aminolevulinic Acid," *The lancet oncology*, vol. 55, pp. 20–26, 2008.

- [39]A. F. Taub, "Photodynamic Therapy in Dermatology," *Journal of the American Academy of Dermatology*, 42(3), pp.389-413. 2011.
- [40]A. F. Taub, K. Berg, J. Moan, M. Kongshaug, and J. M. Neslandl, "Invited Review 5-Aminolevulinic Acid-Based Photodynamic Therapy: Principles and Experimental Research," *Photochemistry and photobiology*, vol. 65, no. 2, pp. 235–251, 1997.
- [41]W. Stummer, U. Pichlmeier, T. Meinel, O. D. Wiestler, F. Zanella, H. Reulen, and A. Study, "Fluorescence-guided surgery with 5-aminolevulinic acid for resection of malignant glioma : a randomised controlled multicentre phase III trial," *The lancet oncology*, vol. 7, no. May, 2006.
- [42]T. F. Refaat, W. S. Luck, and R. J. Deyoung, "Temperature Control of Avalanche Photodiode Using Thermoelectric Cooler," no. October, 1999.
- [43]H. Xie, M. Brydegaard, and S. Andersson-engels, "Development of Multi Light Source System for Fluorescence Detection."
- [44]P. C. D. Hobbs, *Building Electro-Optical Systems: Making It All Work* (Vol. 71), Wiley, 2011.

Appendix A

1. Square wave modulation method back panel
2. Sub VI program for Square wave modulation method
3. Sine wave modulation method front panel
4. Sine wave modulation method front panel





10.21

size(6)

Take out the dynamic signal for each cycle

Find the high level and low level values in each cycle

Calculate the average of samples when laser is on and off, respectively (without the outliers): and then get the difference.

Average

Integrated avg

Replace NaN with 0

cycles to calculate

Numeric

cycles to calculate

0

cycles to calculate

Output Channel Settings

Physical Channel(s): Dev1/ao1

Max Voltage/Min Voltage: 5 / 0

Terminal Configuration: RSE

Sample Rate Input: 100000

Actual Sample Rate Input: 100000

Number of Samples Output: 1000

Waveform Settings: Offset: 10.00, Frequency: 777.00, Amplitude: 1.25

Input Physical Channel

Physical Channel: Dev1/ai1

Max Voltage 2: 10, Min Voltage 2: -5

Terminal Configuration: RSE

Sample Rate Input: 100, Actual Sample Rate Input: 100000

Reference Voltage: 20

reference voltage: 20

read fast enough? AvailSampleChan: 0

file saving path

raw data path: C:\Users\medicinn\Desktop\rawdata.txt

time count down: 100000

Samples writing time: 20

done writing.

Start to write

start to write data in new files

Stop output

RAW signal

Amplitude: 2.5, 3, 3.5, 4, 4.5, 5

Time: 0.00465, 0.006, 0.008, 0.01, 0.01111

FLO FFT spectrum

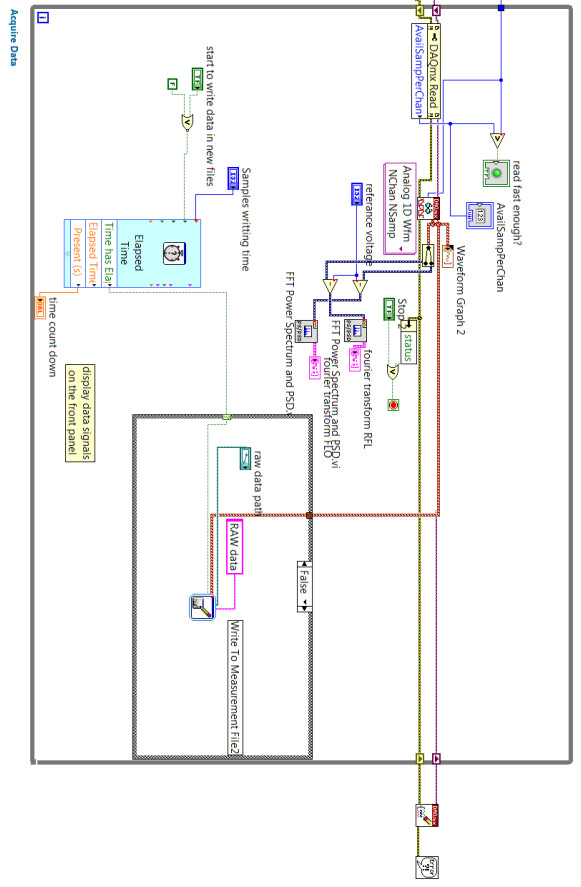
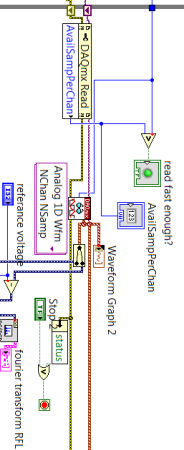
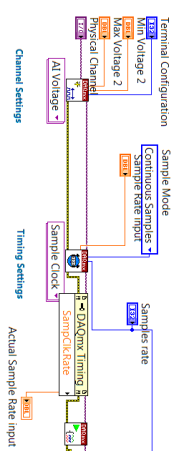
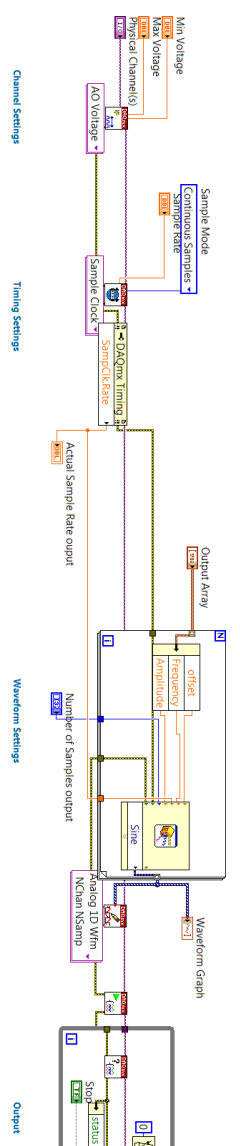
Amplitude: 0.012, 0.01, 0.008, 0.006, 0.004, 0.002

Time: 760.363769, 770, 780, 792.22894

RFL FFT spectrum

Amplitude: 0.014, 0.012, 0.01, 0.008, 0.006, 0.004, 0.002

Time: 756.204988, 780, 793.60355



5. Sine wave modulation signal processing

Matlab program

Main program:

```
fprintf('put in the concentration matrix ,e.g[1 2 3...] ')
concentrationvalue = input('figures coming: ');
FluorvsReflection=handlingSquarewaver(concentrationvalue);
```

Functions involved:

1. handlingSquarewaver.m

```
function C=handlingSquarewaver(concentrationvalue)
clc;
clear all;
mainDirectoryName = cd();
path(path,mainDirectoryName);
listOfMainFiles = dir();
isDirVec = ones(1,length(listOfMainFiles));
```

```
for m=1:length(listOfMainFiles)
    isDirVec(m) =listOfMainFiles(m).isdir;
end
```

```
nbrOfConcentrationPoints = sum(isDirVec)-2;    %Minus
2 beacuse a includes '.' and '..'
```

```
C = cell(nbrOfConcentrationPoints,1);
```

```
for k=(1+2):(nbrOfConcentrationPoints+2)
    listOfMainFiles(k).name
    cd(listOfMainFiles(k).name);
    C{k-2} = collectConcentrationMatrix();
    concentrationCountdown =
(nbrOfConcentrationPoints+2)-k
    cd(mainDirectoryName);
```

```

end

for i=1:length(C)

for j=1:10;
nonzero=C{i}(find(C{i}(:,j)>0),j); %%find non zero sets
in colum
Mg{i}(j,1)=mean(nonzero);
%%to get the avarage of nonzero set in every coloum in
matrix Ci,as there are 10 colums in
%the matrix, put the results put in a new cell would creat
cell with i matrix
%every matrix with 10 results
end
Dv(i)=std(Mg{i});
Mmg(i)=mean(Mg{i});
SNR(i)=Mmg(i)./Dv(i);
% to get the std of each matrix then get i ge results
end

conc=concentrationvalue;
figure(1),
plot(conc,SNR,'r*',conc,SNR)
xlabel('concentration nM')
ylabel('SNR')
title('nomalised SNR...Square wave')

[m n]=size(C);
[a b]=size(C{1});
figure(2),
for i=1:m
    if i==1 || i==6 || i== 11 || i==16 || i==21 || i==27
        p=plot((b*(i-1)+1):b*i,Mg{i}, 'k*')
    elseif i==2 || i==7 || i== 12 || i==17 || i==22 ||
i==28
        p=plot((b*(i-1)+1):b*i,Mg{i}, 'r*')
    end
end

```

```

elseif i==3 || i==8 || i== 13 || i==18 || i==23
|| i==29
    p=plot((b*(i-1)+1):b*i,Mg{i}, 'g*')
        elseif i==4 || i==9 || i== 14 || i==19 || i==24
|| i==30
            p=plot((b*(i-1)+1):b*i,Mg{i}, 'm*')
                elseif i==5 || i==10 || i== 15 || i==20 ||
i==25 || i==31
                    p=plot((b*(i-1)+1):b*i,Mg{i}, 'b*')
else
    printscreen('not enough color')
end
hold on
end
title('results in groups:Square wave dilution result
normalised')
ylabel('signal intensity')
hold off

figure(3)
plot(conc,Mmg,'r*',conc,Mmg)
hold on
nn=1;
index = 1:length(conc);
p=polyfit(conc(index), Mmg(index), nn);
z=polyval(p, conc(index));

hold on,
plot(conc(index), z, 'r'),
xlabel('concentration nM')
ylabel('signal intensity')
title('Square wave dilution result normalised ')
hold off
end

```

2. collectConcentrationMatrix.m

```

function A = collectConcentrationMatrix()
    subDirectoryName = cd();
    listOfSubFiles = dir();
    isDirVec = ones(1,length(listOfSubFiles));

    for m=1:length(listOfSubFiles)
        isDirVec(m) =listOfSubFiles(m).isdir;
    end

    nbrOfDataSets = sum(isDirVec)-2;

    maxDataPoints = 0;

    for k=(1+2):(nbrOfDataSets+2)
        cd(listOfSubFiles(k).name);
        dataColumns = load('0MeanIntegrated.txt');
        if length(dataColumns)>maxDataPoints
            maxDataPoints = length(dataColumns);
        end
        cd(subDirectoryName);
    end
    maxDataPoints

    cd(subDirectoryName);
    A = zeros(maxDataPoints,nbrOfDataSets);

    for k=(1+2):(nbrOfDataSets+2)
        cd(listOfSubFiles(k).name);
        dataColumns = load('0MeanIntegrated.txt');
        A(1:length(dataColumns(:,1)),k-2) =
dataColumns(:,1)./dataColumns(:,2);
        B= dataColumns(:,1);
        C=dataColumns(:,2);
    end
end

```

```
        cd(subDirectoryName);  
    end  
end
```

6. Square wave modulation signal processing

Many version of square wave processing codes are produced for different plotting purposes, here will present the last version of plotting program, and the functions involved should be considered more important.

Main program:

```
cd('C:\Users\Arefeh\Desktop\data\different
concentration\19.11\sin\0nm\')
[SBR_0405,centralreflect_0405,reflectplot_0405,SBR_06
35,centralrefluorescence_0635,fluorplot_0635]=
dealwithdata(777);
flvsrf0=centralrefluorescence_0635(:,2)./centralreflect_04
05(:,2)
SBR0=mean(flvsrf0)/mean(SBR_0635)
SNR0=mean(flvsrf0)/std(flvsrf0);
cd('C:\Users\Arefeh\Desktop\data\different
concentration\19.11\sin\6.2nm\')
[SBR_6n405,centralreflect_6n405,reflectplot_6n405,SBR
_6n635,centralrefluorescence_6n635,fluorplot_6n635]=
dealwithdata(777);
flvsrf6n=centralrefluorescence_6n635(:,2)./centralreflect_
6n405(:,2)
SBR6n=mean(flvsrf6n)/mean(SBR_6n635)
SNR6n=mean(flvsrf6n)/std(flvsrf6n);
cd('C:\Users\Arefeh\Desktop\data\different
concentration\19.11\sin\8.3nm\')
[SBR_8n405,centralreflect_8n405,reflectplot_8n405,SBR
_8n635,centralrefluorescence_8n635,fluorplot_8n635]=
dealwithdata(777);
flvsrf8n=centralrefluorescence_8n635(:,2)./centralreflect_
8n405(:,2)
SBR8n=mean(flvsrf8n)/mean(SBR_8n635)
```

```
SNR8n=mean(flvsrf8n)/std(flvsrf8n);
```

```
cd('C:\Users\Arefeh\Desktop\data\different  
concentration\19.11\sin\11nm\')  
[SBR_11n405,centralreflect_11n405,reflectplot_11n405,S  
BR_11n635,centralrefluorescence_11n635,fluorplot_11n6  
35]= dealwithdata(777);  
flvsrf11n=centralrefluorescence_11n635(:,2)./centralreflec  
t_11n405(:,2)  
SBR11n=mean(flvsrf11n)/mean(SBR_11n635)  
SNR11n=mean(flvsrf11n)/std(flvsrf11n);
```

```
cd('C:\Users\Arefeh\Desktop\data\different  
concentration\19.11\sin\14nm\')  
[SBR_14n,centralreflect_14n405,reflectplot_14n405,SBR  
_14n635,centralrefluorescence_14n635,fluorplot_14n635]  
= dealwithdata(777);  
flvsrf14n=centralrefluorescence_14n635(:,2)./centralreflec  
t_14n405(:,2);  
SBR14n=mean(flvsrf14n)/mean(SBR_14n635);  
SNR14n=mean(flvsrf14n)/std(flvsrf14n);
```

```
cd('C:\Users\Arefeh\Desktop\data\different  
concentration\19.11\sin\16nm\')  
[SBR_16n,centralreflect_16n405,reflectplot_16n405,SBR  
_16n635,centralrefluorescence_16n635,fluorplot_16n635]  
= dealwithdata(777);  
flvsrf16n=centralrefluorescence_16n635(:,2)./centralreflec  
t_16n405(:,2);  
SBR16n=mean(flvsrf16n)/mean(SBR_16n635);  
SNR16n=mean(flvsrf16n)/std(flvsrf16n);
```

```
cd('C:\Users\Arefeh\Desktop\data\different  
concentration\19.11\sin\20nm\')
```

```
[SBR_20n405,centralreflect_20n405,reflectplot_20n405,SBR_20n635,centralrefluorescence_20n635,fluorplot_20n635]= dealwithdata(777);
flvsrf20n=centralrefluorescence_20n635(:,2)./centralreflect_20n405(:,2)
SBR20n=mean(flvsrf20n)/mean(SBR_20n635);
SNR20n=mean(flvsrf20n)/std(flvsrf20n);
```

```
cd('C:\Users\Arefeh\Desktop\data\different concentration\19.11\sin\25nm\')
[SBR_25n405,centralreflect_25n405,reflectplot_25n405,SBR_25n635,centralrefluorescence_25n635,fluorplot_25n635]= dealwithdata(777);
flvsrf25n=centralrefluorescence_25n635(:,2)./centralreflect_25n405(:,2);
SBR25n=mean(flvsrf25n)/mean(SBR_25n635);
SNR25n=mean(flvsrf25n)/std(flvsrf25n);
```

```
cd('C:\Users\Arefeh\Desktop\data\different concentration\19.11\sin\33nm\')
[SBR_33n405,centralreflect_33n405,reflectplot_33n405,SBR_33n635,centralrefluorescence_33n635,fluorplot_33n635]= dealwithdata(777);
flvsrf33n=centralrefluorescence_33n635(:,2)./centralreflect_33n405(:,2);
SBR33n=mean(flvsrf33n)/mean(SBR_33n635);
SNR33n=mean(flvsrf33n)/std(flvsrf33n);
```

```
cd('C:\Users\Arefeh\Desktop\data\different concentration\19.11\sin\40nm\')
[SBR_40n405,centralreflect_40n405,reflectplot_40n405,SBR_40n635,centralrefluorescence_40n635,fluorplot_40n635]= dealwithdata(777);
flvsrf40n=centralrefluorescence_40n635(:,2)./centralreflect_40n405(:,2);
SBR40n=mean(flvsrf40n)/mean(SBR_40n635);
```

```
SNR40n=mean(flvsrf40n)/std(flvsrf40n);
```

```
cd('C:\Users\Arefeh\Desktop\data\different  
concentration\19.11\sin\50nm\')  
[SBR_50n405,centralreflect_50n405,reflectplot_50n405,S  
BR_50n635,centralrefluorescence_50n635,fluorplot_50n6  
35]= dealwithdata(777);  
flvsrf50n=centralrefluorescence_50n635(:,2)./centralreflec  
t_50n405(:,2);  
SBR50n=mean(flvsrf50n)/mean(SBR_50n635);  
SNR50n=mean(flvsrf50n)/std(flvsrf50n);
```

```
cd('C:\Users\Arefeh\Desktop\data\different  
concentration\19.11\sin\55nm\')  
[SBR_55n405,centralreflect_55n405,reflectplot_55n405,S  
BR_55n635,centralrefluorescence_55n635,fluorplot_55n6  
35]= dealwithdata(777);  
flvsrf55n=centralrefluorescence_55n635(:,2)./centralreflec  
t_55n405(:,2)  
SBR55n=mean(flvsrf55n)/mean(SBR_55n635);  
SNR55n=mean(flvsrf55n)/std(flvsrf55n);
```

```
cd('C:\Users\Arefeh\Desktop\data\different  
concentration\19.11\sin\62nm\')  
[SBR_62n405,centralreflect_62n405,reflectplot_62n405,S  
BR_62n635,centralrefluorescence_62n635,fluorplot_62n6  
35]= dealwithdata(777);  
% fluorescencevsreflect  
flvsrf62n=centralrefluorescence_62n635(:,2)./centralreflec  
t_62n405(:,2);  
SBR62n=mean(flvsrf62n)/mean(SBR_62n635);  
SNR62n=mean(flvsrf62n)/std(flvsrf62n);
```

```
cd('C:\Users\Arefeh\Desktop\data\different  
concentration\19.11\sin\71nm\')
```

```

[SBR_71n405,centralreflect_71n405,reflectplot_71n450,S
BR_71n635,centralrefluorescence_71n635,fluorplot_71n6
35]= dealwithdata(777);
% fluorescencevsreflect
flvsrf71n=centralrefluorescence_71n635(:,2)./centralreflec
t_71n405(:,2);
SBR71n=mean(flvsrf71n)/mean(SBR_71n635);
SNR71n=mean(flvsrf71n)/std(flvsrf71n);

cd('C:\Users\Arefeh\Desktop\data\different
concentration\19.11\sin\83nm')
[SBR_83n405,centralreflect_83n405,reflectplot_83n405,S
BR_83n635,centralrefluorescence_83n635,fluorplot_83n6
35]= dealwithdata(777);
% fluorescencevsreflect
flvsrf83n=centralrefluorescence_83n635(:,2)./centralreflec
t_83n405(:,2);
SBR83n=mean(flvsrf83n)/mean(SBR_83n635);
SNR83n=mean(flvsrf83n)/std(flvsrf83n);

cd('C:\Users\Arefeh\Desktop\data\different
concentration\19.11\sin\100nm\')
[SBR_100n405,centralreflect_100n405,reflectplot_a100n4
05,SBR_100n635,centralrefluorescence_100n635,fluorplot
_100n635]= dealwithdata(777);
%fluorescencevsreflect
flvsrf100n=centralrefluorescence_100n635(:,2)./centralrefl
ect_100n405(:,2);
SBR100n=mean(flvsrf100n)/mean(SBR_100n635);
SNR100n=mean(flvsrf100n)/std(flvsrf100n);
% Plot(flvsrf)
steps=linspace(1,85,85);
figure(21)
plot(steps(1:5),flvsrf0,'r*-')
hold on
plot(steps(6:10),flvsrf6n,'r*-')

```

```

hold on
plot(steps(11:15),flvsrf8n,'r*-' )
hold on
plot(steps(16:20),flvsrf16n,'r*-' )
hold on
plot(steps(21:25),flvsrf20n,'b*-' )
hold on
plot(steps(26:30),flvsrf25n,'r*-' )
hold on
plot(steps(31:35),flvsrf33n,'g*-' )
hold on
plot(steps(36:40),flvsrf40n,'k*-' )
hold on
plot(steps(41:45),flvsrf50n,'r*-' )
hold on
plot(steps(46:50),flvsrf55n,'b*-' )
hold on
plot(steps(51:55),flvsrf62n,'g*-' )
hold on
plot(steps(56:60),flvsrf71n,'k*-' )
hold on
plot(steps(61:65),flvsrf83n,'r*-' )
hold on
plot(steps(66:70),flvsrf100n,'b*-' )
hold on
plot(steps(71:75),flvsrf83n,'go*-' )
hold on
plot(steps(76:80),flvsrf100n,'ko*-' )
title('fluorescence vs reflection')
legend('0
nM','6.2nM','8.3nM','16nM','20nM','25nM','33nM','40nM
','50nM','55nM','62nM','71nM','83nM','100nM','Location',
'EastOutside')

% plot SNR
figure(31)

```

```

SNR=zeros(1,14)
SNR(1,1)=mean(flvsrf0)./std(flvsrf0)
SNR(1,2)=mean(flvsrf6n)./std(flvsrf6n)
SNR(1,3)=mean(flvsrf8n)./std(flvsrf8n)
SNR(1,4)=mean(flvsrf11n)./std(flvsrf11n)
SNR(1,5)=mean(flvsrf14n)./std(flvsrf14n)
SNR(1,4)=mean(flvsrf16n)./std(flvsrf16n)
SNR(1,5)=mean(flvsrf20n)./std(flvsrf20n)
SNR(1,6)=mean(flvsrf25n)./std(flvsrf25n)
SNR(1,7)=mean(flvsrf33n)./std(flvsrf33n)
SNR(1,8)=mean(flvsrf40n)./std(flvsrf40n)
SNR(1,9)=mean(flvsrf50n)./std(flvsrf50n)
SNR(1,10)=mean(flvsrf55n)./std(flvsrf55n)
SNR(1,11)=mean(flvsrf62n)./std(flvsrf62n)
SNR(1,12)=mean(flvsrf71n)./std(flvsrf71n)
SNR(1,13)=mean(flvsrf83n)./std(flvsrf83n);
SNR(1,14)=mean(flvsrf100n)./std(flvsrf100n)
z=[0 6 8 16 20 25 33 40 50 55 62 71 83 100]
plot(z,SNR,'r*')
hold on
nn=1;
p=polyfit(z,SNR,nn);
xi=linspace(0,100,100);
r=polyval(p,xi);
plot(z,SNR,'g',xi,r,'b:')
title('SNR...SIN WAVE')
ylabel('SNR')
xlabel('concentration nM')

% plot SBR
figure(41)
SBR=zeros(1,12)
SBR(1,1)=SBR0;
SBR(1,2)=SBR14n;
SBR(1,3)=SBR20n;
SBR(1,4)=SBR25n;

```

```

SBR(1,5)=SBR33n;
SBR(1,6)=SBR40n;
SBR(1,7)=SBR50n;
SBR(1,8)=SBR55n;
SBR(1,9)=SBR62n;
SBR(1,10)=SBR71n;
SBR(1,11)=SBR83n;
SBR(1,12)=SBR100n;
z=[0 14 20 25 33 40 50 55 62 71 83 100]
plot(z,SBR,'g*-')
hold on
nn=1;
p=polyfit(z,SBR,nn);
xi=linspace(0,100,100);
r=polyval(p,xi);
plot(z,SBR,'r',xi,r,'b:')
title('SBR...SIN WAVE')
ylabel('SBR')
xlabel('concentration nM')

```

```

% plot flvsrf
figure(51)
fl=zeros(1,14);
fl(1,1)=mean(flvsrf0);
fl(1,2)=mean(flvsrf6n);
fl(1,3)=mean(flvsrf8n);
fl(1,4)=mean(flvsrf11n);
fl(1,5)=mean(flvsrf14n);
fl(1,4)=mean(flvsrf16n);
fl(1,5)=mean(flvsrf20n);
fl(1,6)=mean(flvsrf25n);
fl(1,7)=mean(flvsrf33n);
fl(1,8)=mean(flvsrf40n);
fl(1,9)=mean(flvsrf50n);
fl(1,10)=mean(flvsrf55n);
fl(1,11)=mean(flvsrf62n);

```

```

fl(1,12)=mean(flvsrf71n);
fl(1,13)=mean(flvsrf83n);
fl(1,14)=mean(flvsrf100n);
z=[0 6 8 16 20 25 33 40 50 55 62 71 83 100];
plot(z,fl,'g*-')
hold on
nn=1;
p=polyfit(z,fl,nn);
xi=linspace(0,100,100);
r=polyval(p,xi);
plot(z,fl,'r',xi,r,'b:')
title('fl/rf...SIN WAVE')
ylabel('Normalized intensity')
xlabel('concentration nM')
functions involved:
1. dealwithdata.m
function
[SBR1,centralreflect,reflectplot,SBR,centralrefluorescence,
fluorplot]= dealwithdata(centralfrequency)
close all
clc;
%---For importing data-----
-----
datalist = dir('**.txt');
m = length(load(datalist(1).name));
n = length(datalist);
%Kx1Matrix = zeros(m,n);      %Matrix dimensions:
Maximum number of data points x number of sets of data
%Kx2Matrix = zeros(m,n);      %Matrix dimensions:
Maximum number of data points x number of sets of data
centralrefluorescence=zeros(n,2);
centralrefluorescence(:,1)=linspace(0,n,n);
centralreflect=zeros(n,2);
centralreflect(:,1)=linspace(0,n,n);
fluorplot=zeros(615*n,2);
fluorplot(:,1)=linspace(0,2,615*n);

```

```

reflectplot=zeros(615*n,2);
reflectplot(:,1)=linspace(0,n,615*n);
SBR1 = zeros(n,1);
SBR = zeros(n,1);
STDfl = zeros(n,1);
STDrf = zeros(n,1);

for k=1:n
    %---For loading the data-----
    -----
    datak = load(datalist(k).name);
    Kk1 = datak(:,1)-1;
    Kk2 = 1 - datak(:,2);
    %-----
    -

    %---For analysis of data-----
    -----

    [SBR1(k,1),centralreflect(k,2),reflectplot(((k-
1)*615+1):(k*615),2)] =
reflectcentralfrequency(Kk2,centralfrequency);
    [SBR(k,1),centralrefluorescence(k,2),fluorplot(((k-
1)*615+1):(k*615),2)] =
fluorescencecentralfrequency(Kk1,centralfrequency);
    %-----
    -

end
%-----
-

End

```

2. reflectcentralfrequency.m

function

```

[SBR1,intergrationreflection,X1]=reflectcentralfrequency(d
atafilename,centralfrequency)

```

```

B=datafilename;
C=centralfrequency;
%% fuorier spectrum tranform
N = 2048000;
X = abs(fft(B,N));
X = fftshift(X);
F = ([-N/2:N/2-1]/N)*100000;
F1=abs(F);
subplot(3,2,[1 3 5])
plot(F1,X,'g')
hold on
plot(F1,X,'r')
title('fft')
legend('realvalus','absvalue')
xlim([0,1000])
ylim([0,2.3*100000])
%% plot central frequency bandwidth 30hz
index1=find(F>=(C-15)&F<=(C+15));
X1=zeros(length(index1),1);
X1=X(index1);
subplot(3,2,2)
plot(F(index1),X1)
title('central frequency+-15')
% integration around central frequency
intergrationreflection=sum(X1);
%% plot DC component frequency bandwidth 30hz
index2=find(F>=0&F<=30);
X2=zeros(length(index2),1);
X2=X(index2);

subplot(3,2,4)
plot(F(index2),X2,'m')
title('bandwidth 30hz DC signal')
%%integration around 0 frequency
intergrationDC=sum(X2);

```

```

subplot(3,2,6)
plot(B,'k')
xlim([300,800])
title('x-axis 300 to 800')
plot(F1(index4),X4,'k')
title('bandwidth 30hz around 100Hz signal')
intergration100Hz=sum(X4)
%%
display('-----
      SBR=intergrationreflection/intergrationDC-----')
SBR1=intergrationreflection/intergrationDC;

display('-----
SNR=intergrationfluorescence/(intergration50Hz+intergr
ation100Hz)-----')
SNR=intergrationfluorescence/(intergration50Hz+intergr
ation100Hz)
End

```

3. fluorescencecentralfrequency.m

```

function [SBR,intergrationfluorescence,X1]=
fluorescencecentralfrequency(datafilename,centralfrequenc
y)
B=datafilename;
C=centralfrequency;
%% fuorier spectrum tranform
N = 2048000;
X = abs(fft(B,N));
X = fftshift(X);
F = ([-N/2:N/2-1]/N)*100000;
F1=abs(F);
subplot(3,2,[1 3 5])
plot(F1,X,'g')
% hold on
% plot(F1,X,'r')
% title('fft')

```

```

% legend('realvalue','absvalue')
xlim([0,1000])
% ylim([0,2.3*100000])
%% plot central frequency bandwidth 30hz

index1=find(F>=(C-15)&F<=(C+15));
X1=zeros(length(index1),1);
X1=X(index1);

subplot(3,2,2)
plot(F(index1),X1)
title('central frequency+-15')

% integration around central frequency
intergrationfluorescence=sum(X1);
%% plot DC component frequency bandwidth 30hz
index2=find(F>=0&F<=30);
X2=zeros(length(index2),1);
X2=X(index2);

subplot(3,2,4)
plot(F(index2),X2,'m')
title('bandwidth 30hz DC signal')
% integration around 0 frequency
intergrationDC=sum(X2);
%%
% index3=find(F1>35&F1<65);
% X3=zeros(length(index3),1);
% X3=X(index3);
%
% subplot(4,2,6)
% plot(F1(index3),X3,'g-')
% title('bandwidth 30hz around 50Hz signal')
% intergration50Hz=sum(X3)
% %%
% index4=find(F1>85&F1<115);

```

```

% X4=zeros(length(index4),1);
% X4=X(index4);

subplot(3,2,6)
plot(B,'k')
xlim([300,800])
title('x-axis 200 to 600')
% plot(F1(index4),X4,'k')
% title('bandwidth 30hz around 100Hz signal')
% intergration100Hz=sum(X4)
%%
%
%                                     display('-----')
SBR=intergrationfluorescence/intergrationDC-----')
SBR=intergrationDC;

%
%                                     display('-----')
SNR=intergrationfluorescence/(intergration50Hz+intergr
ation100Hz)-----')
%
SNR=intergrationfluorescence/(intergration50Hz+intergr
ation100Hz)

end

```

Appendix B

Papers

Papers I

Design and validation of a fiber optic point probe instrument for therapy guidance and monitoring

Haiyan Xie,^a Zhiyuan Xie,^a Monirehalsadat Mousavi,^a Niels Bendsoe,^b
Mikkel Brydegaard,^a Johan Axelsson,^a and Stefan Andersson-Engels^a

^aLund University, Department of Physics, P.O. Box 118, Lund, Sweden, SE-221 00

^bSkåne University Hospital, Department of Dermatology and Venereology, Lasarettsgatan 15, Lund, Sweden, SE-221 85

Abstract. Optical techniques for tissue diagnostics are experiencing tremendous growth in biomedical applications nowadays, mainly due to their non-invasive, inexpensive and real-time functionality. Here we demonstrate a novel hand-held fiber optic probe instrument based on fluorescence/reflectance spectroscopy for precise tumor delineation. It is mainly aimed for brain tumor resection guidance with clinically-adaption to minimize the disruption of the standard surgical workflow and meant as a complement to the state-of-the-art fluorescence surgical microscopy technique. Multiple light sources with fast pulse modulation and lock-in like detection enable precise quantification of PpIX, tissue optical properties and ambient light suppression. Laboratory measurements show the system is insensitive to strong ambient light. Validation measurements of tissue phantoms using non-linear Least Squares Support Vector Machines (LS-SVM) regression analysis demonstrate an error of less than 5% for PpIX concentration ranging from 400 to 1000 nM, even in presence of large variations in phantom optical properties. The mean error is 3% for reduced scattering coefficient and 5% for blood concentration, respectively. Diagnostic precision of 100% was obtained by LS-SVM classification for *in vivo* skin tumors with topically applied ALA during photodynamic therapy. The probe could easily be generalized to other tissue types and fluorophores for therapy guidance and monitoring.

Keywords: fiber optic sensors, fluorescence spectroscopy, reflectance, tissues, light-emitting diodes.

Address all correspondence to: Haiyan Xie, Lund Univeristy, Department of Physics, Professorsgatan 1, Lund, Sweden, SE-221 00; Tel: +46 46-222-3119; Fax: +46 46-222-4250; E-mail: haiyan.xie@fysik.lth.se

1 Introduction

Optical techniques provide powerful means for tissue diagnostics in a wide variety of biomedical applications nowadays. The extensive efforts have been made in developing optical diagnostic tools which are non-invasive, inexpensive and could be applied *in vivo* and real-time. Fiber optic probes for biomedical optical spectroscopy enable clinical use in endoscopy, surgery and neurological imaging.¹ Typically, such a probe incorporates a light source, fiber optic cables for light transport, and an optical detector integrated with spectroscopic devices. Different spectroscopic fiber optic probes have since long been developed and used to substantially improve clinical diagnostic capability for different purposes,^{2,3} such as surgical guidance during brain tumor resection,⁴⁻⁶ determination of tissue optical property for optical biopsy of brain tissue⁷ and for interstitial photodynamic therapy,⁸ treatment monitoring during photodynamic therapy,^{9,10} lung cancer staging of mediastinal lymph nodes,¹¹ diagnosis of non-alcoholic fatty liver diseases,¹² detection of metastatic breast cancer in sentinel lymph nodes,¹³ tumor oxygenation monitoring and tissue optical properties evaluation for breast cancer diagnosis.^{14,15} These probes have the flexibility that they can either be manufactured into cavities or tubular structures, put in contact with epithelial surfaces, or inserted into structures, punctured by rigid devices such as needles.¹

Most of the spectroscopic fiber optic probes for biomedical applications are performing reflectance and/or fluorescence spectroscopy of turbid tissues. These probes are capable of providing quantitative molecular and functional information to distinguish normal from abnormal human

tissues. For example, Kanick *et al.*¹¹ employed a single-fiber reflectance spectroscopy system for lung cancer staging. They developed a data evaluation model to extract information about the physiological and morphological properties of lymph tissue. Austwick *et al.*¹³ developed a scanning elastic scattering spectroscopy system, combined with statistical discrimination analysis. It was used to detect metastatic breast cancer in sentinel lymph nodes. Fluorescence spectroscopic probes are a different approach, where either endogenous tissue fluorescence (*i.e.* tissue autofluorescence) or exogenous fluorescence from contrast agents is used for tissue discrimination. For instance, a fiber optic fluorosensor was developed to measure the fluorescence signal from 5-aminolevulinic acid (ALA)-induced Protoporphyrin IX (PpIX) for tumor resection guidance during the open brain surgery.^{4,5} To correct for tissue autofluorescence superimposed on the PpIX fluorescence peak, a dimensionless fluorescence ratio was taken between these two spectral bands. To further improve the data evaluation, a photobleaching-insensitive method was developed based on a dynamic model together with multivariate analysis.¹⁶ Valdes *et al.* reported a combined fluorescence and reflectance spectroscopy system for *in vivo* quantification of PpIX in low- and high-grade glioma surgery. They conducted model based evaluation to correct the detected fluorescence spectra for tissue optical properties from the reflectance.^{6,17} Foscan[®] concentration in rat liver *in vivo* was measured by Kruijt *et al* with fluorescence differential path length spectroscopy, based on the fluorescence intensity corrected for absorption from the differential reflectance spectra.¹⁸

Fluorescence biochemical probes have been extensively applied to fluorescence-guided surgery (FGS) of malignant brain tumors.^{5,19-21} In this area, 5-ALA-induced-PpIX accumulates in malignant tumors and inflamed brain tissue because of the blood-brain barrier.^{20,21} The resulting increased tumor tissue fluorescence is used to enhance the contrast between the tumors and surrounding healthy tissue. It could thus assist the surgeon in deciding which tissue to remove or spare in the open brain surgery and improve surgical outcomes. By this technique, brain tumors have been visualized using two types of fluorescence probes: Type I. Point spectroscopic tools (such as fiber optic probes) for measuring at one region at a time; Type II. Imaging systems (such as *in vivo* fluorescence microscopy, modified surgical microscopes, commercial neurosurgical operating fluorescent microscopes) for displaying every point in the area of resection. The non-contact surgical microscopy instruments are implemented as a standard in surgical resection today. However, it suffers from only being useful for identifying tumor subtypes with relatively high PpIX accumulation due to its low sensitivity from the limited capture of light.^{6,19,22} The imaging modalities are also limited to very superficial tissue as a result of the limited penetration depth for the excitation light. In contrast, a point probe can provide spectroscopy with better spectral information and usually higher overall sensitivity. It can be incorporated into hand tools used by the surgeon, such as ultrasonic vacuum suction devices, scalpels, and navigation systems.⁵ Therefore it can proceed to underlying regions and be able to probe the tissue just to be removed. Further, this may allow penetration beyond the exposed superficial cell layer, which is of critical importance in resecting the infiltrative tumors. The previous point monitoring systems have mainly used fluorescence spectroscopy based on spectrometers. Despite many wavelength channels, those systems only provide at most three spectral components among several individuals and measurement locations,¹⁶ thus providing limited diagnostic information for tissue diagnostics of complex tissue structures. In addition, a slight limitation with both current imaging and fiber based FGS systems is their high sensitivity to the surrounding light sources in the operating room (OR). This results from the fact that the integration time of the detector had to be long enough to detect the weak fluorescence signal. The light fluctuation within the relatively long measurement time could also lead to imprecise

measurements. Dim lighting conditions or shading the measurement region from the direct light required by current FGS systems are obviously disruptive to standard surgical workflow. There exists a need for an intraoperative FGS fluorescence spectroscopic system capable of suppressing ambient light in the OR while high fluorescence sensitivity and larger probing depth could be achieved.

In this paper, we demonstrate a novel clinically-adapted hand-held fiber optic probe system based on fluorescence/reflectance spectroscopy with pulse modulation in combination with the lock-in like detection. The probe was validated by tissue phantom measurements and *in vivo* clinical measurements on patients with skin tumors. It demonstrates insensitivity to the ambient light as well as accurate assessment of both fluorophore concentration and tissue optical properties. It is mainly aimed for brain tumor resection guidance, by providing the operating surgeon with an intuitive and real-time surgical guidance tool. The probe is applicable to other tissue types and fluorophores for therapy guidance and monitoring in a general sense.

2 Materials and Methods

2.1 System description

The fiber optic probe instrument described here was configured to quantify PpIX using fluorescence/reflectance light for therapy guidance and monitoring under surgical conditions during open brain surgery. The schematic diagram of the probe system is shown in Fig. 1. It consists of a light source with five fiber-coupled light-emitting diodes (LEDs), a source/detector fiber optic probe, a detection unit, a data acquisition (DAQ) board, electronic circuits, and a laptop computer. The entire system was assembled on a trolley with a dimension of $80 \times 50 \times 100 \text{ cm}^3$ and a total weight of 15 kg, to facilitate flexibility in use in the examination room or OR.

2.1.1 Light source

The light source comprises five fiber-coupled LEDs (Prizmatix Ltd., Israel; FC5-LED) at four different wavelengths: 365, 405, 530 and 635 nm, as well as a white light LED. (450-700nm). The 405-nm and 365-nm LED were chosen to provide a strong signal from PpIX fluorescence at 635 nm and tissue autofluorescence with a broad spectrum in the visible range, respectively. The other three LEDs were used to monitor tissue optical properties from the reflectance measurements at wavelengths of interest. When running in the continuous mode, all LEDs had a maximal output power of approximately 13 mW through a polymer optical fiber (POF) of $750 \mu\text{m}$ core diameter and a numerical aperture (NA) of 0.5. The power could be adjusted with a potentiometer located on the front panel.

All LEDs were multiplexed to work sequentially, driven by a TTL pulse at 777 Hz with a duty cycle of 8.3% for each LED. The source multiplexing module consists of a counter (CD40193) and a demultiplexer (CD4514). There were six pulses within one period: Each LED was lit up in turn within the first five pulses, followed by one pulse with all LEDs switched off. This allowed the measurement of ambient light level.

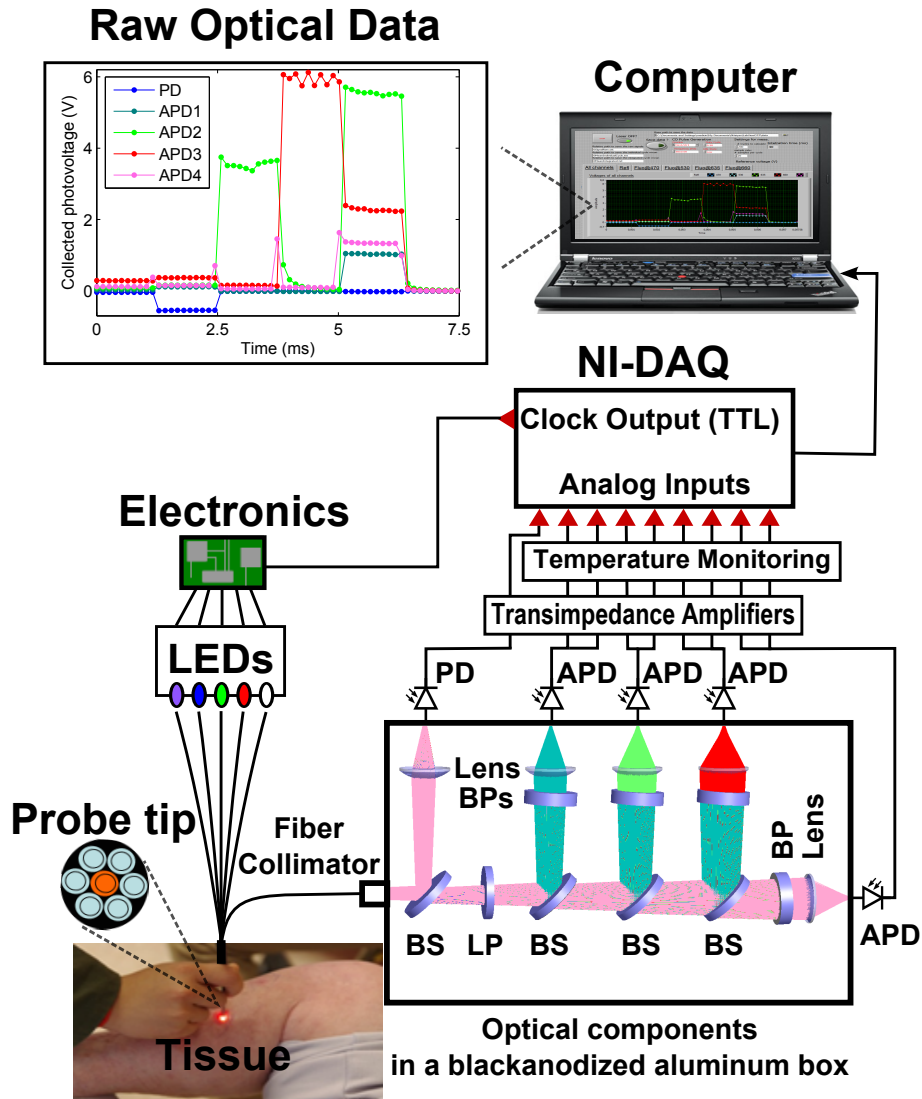


Fig 1 Schematic diagram of the fiber optic point probe system, illustrating in vivo measurement of a skin lesion on the right leg of a patient. The subplot on the top left shows the real-time raw optical data detected by the five photo detectors, including the PpIX fluorescence, tissue autofluorescence and reflectance spectra. Here the abbreviations in the figure are BS (dichroic beam splitter), LP (long-pass filter), BP (band-pass filter), PD (photodiode), and APD (avalanche photodiode).

2.1.2 Fiber optic probe

The custom-made hand-held fiber probe (Prizmatix Ltd.; Y-shaped fiber patch cord bundle) consists of six surrounding delivery fibers (one spare fiber during the measurement) and one collection fiber at the center. All fibers were made of POFs (750 μm core diameter, 0.50 NA, 4 m long), which could be sterilized with ETO gas in clinical practice. They were bundled together into a stainless steel tube (5 cm long and with a 4 mm diameter), and the other end of the fibers was assembled to an SMA905 connector. The distance between two adjacent cores is almost the same as the fiber core diameter as the cladding of POF is less than 15 μm . The probe tip was held perpendicular to and in contact with the sample surface.

2.1.3 Detection unit

The collected light from the sample was detected by the detection unit, mounted in a compact black anodized aluminum box (designed in-house using CAD). Collected light from the central fiber was collimated (Edmund Optics; 64770) and split into five different light paths by four dichroic beam splitters (BS) (Thorlabs; DMPL425, 505, 567 and 638). On each path, light was detected either by a silicon photodiode (PD) (Edmund Optics; 53378) with a UV enhanced response, or an avalanche photodiode (APD) (Hamamatsu; S9075, ϕ 1.5 mm active area). All four APDs were working at a reversed bias voltage of approximately -160 V, generated from an APD bias voltage power supply module (Hamamatsu; M6017). To suppress the back-reflected elastic violet light from reaching the APDs, a long pass cut-off filter (Edmund Optics; GG-435) was positioned after the first elastic channel. In front of each detector, there is a light focusing lens (Edmund Optics; 47884). For each APD, a 10 nm FWHM (Full Width at Half Maximum) narrowband band-pass filter (Edmund Optics; FB470-10, FB530-10, FB-635-10, and FB-660-10, respectively) was assembled. The photocurrent in each detector was converted to voltage with a larger dynamic range by an in-house transimpedance amplifier, consisting of an Operation Amplifier and RC feedbacks. The entire box has a dimension of $200 \times 120 \times 104 \text{ mm}^3$, together with the components.

2.1.4 Pulse generation and data acquisition

The TTL pulse to modulate the light source was generated from the digital clock output of a 16-bit DAQ board (National Instruments; NI USB-6351). The photovoltages in the PD and APDs were recorded by the analog inputs of the DAQ.

2.1.5 Intensity calibration

The intensity of each detection band was calibrated with a high-power quartz tungsten halogen lamp (Oriel; 63355), powered by a current power supply (Oriel; 68830) with an output current of 6.5 A. Light from the calibration lamp was guided by an optic fiber (Thorlabs; 600 μm core diameter, 0.39 NA, positioned 5 m away from the lamp) and entered the detection box without any sample. The voltage outputs on the photo detectors were normalized to the known intensity spectrum of the lamp for all five detection channels.

Unless otherwise stated, all calibration measurements were conducted in a dark laboratory room.

2.1.6 Thermal calibration

To compensate for the gain variation with temperature, each APD was glued with a thermistor (PTC 60-323-30, Elfa Distrelecs, Sweden) on the rear surface so that the APD temperature could be monitored. Thermal calibration measurement was performed in a similar way as described in Section 2.1.5 but mounting all detection units in a mobile car fridge (Mobicool Ltd., China; TC-16-12/230), which could be cooled down to +14°C. The measured photovoltage on each APD (V_{APD_i}) versus the voltage on each thermistor (V_{Therm_i}) was fitted by an exponential equation:

$$V_{Therm_i} = ae^{bV_{Therm_i}} \quad (i = 1 - 4), \quad (1)$$

where a and b are fitting coefficients. Both V_{APD_i} and V_{Therm_i} were averaged over all samples within the integration time. For each photovoltage measured later on, it was multiplied by a thermal calibration factor, $F_{Calib}(V_{Therm_i})$, calculated from the corresponding thermal voltage with Eq. 1:

$$F_{Calib}(V_{Therm_i}) = 1/(ae^{bV_{Therm_i}}) \quad (i = 1 - 4), \quad (2)$$

2.1.7 Software

Pulse generation, data acquisition and real-time signal manipulation were performed by a custom LabVIEW[®] (National Instruments; Version 2012) application running on a laptop computer. Off-line data analysis was performed in the Matlab[®] environment (MathworksTM, Inc.; version R2012a) on a conventional PC. LS-SVMlab (version 1.8),²³ a MATLAB toolbox for Least Squares Support Vector Machines (LS-SVM), was employed for multivariate regression and tissue classification analysis.

2.2 Experimental procedure

2.2.1 Phantom preparation

Phantom experiments were carried out to test the system performance. A set of well controlled tissue-like liquid phantoms were prepared by mixing water, intralipid (Fresenius Kabi, Sweden; 200 mg/ml), and India ink (Pelican Fount, Germany; 1:100 stock solution prepared in our lab) or bovine blood (purchased from a local supermarket). The optical properties were chosen to have a good correspondence to real biological tissue. PpIX stock solution was prepared by dissolving 0.056 g PpIX powder (Fisher Scientific) in 20 ml Dimethyl sulfoxide (DMSO) (Merck, Germany) and 80 ml distilled water, resulting in a PpIX concentration of 1 mM. When diluting the PpIX solution in the phantom, 2% volume of Tween (Scharlau Chemie S.A., Spain) was added to prevent PpIX from aggregation. The ink phantom contained 3.75% volume of intralipid, 0.25% volume of ink, and 100 nM PpIX. In total 270 blood phantoms were prepared, containing different concentrations of intralipid (3, 4, 5, 6, 7 and 8%, v:v), bovine blood (0, 1, 2, 3 and 4%, v:v), and PpIX (0, 100, 200, 300, 400, 500, 600, 750 and 1000 nM), respectively. Each phantom was placed in a cylindrical glass container. The phantoms were stirred for four hours prior to the measurements using a magnetic stirrer (to assure that the temperature of each APD was stable) and kept stirred during the measurements.

The reduced scattering coefficient of each phantom, in $\text{cm}^{-1}/(\text{ml}/1)$, was estimated from the expression:²⁴

$$\mu'_s(\lambda) = C \cdot (0.58 \cdot (\lambda/1\mu\text{m}) - 0.1) \cdot 0.32 \cdot (\lambda/1\mu\text{m})^{-2.4}, \quad (3)$$

where C is the concentration of intralipid-20% in ml/l, λ is the light wavelength in μm .

The absorption coefficient at 635 nm, $\mu_a(635)$, and reduced scattering coefficient, $\mu'_s(635)$, of the phantoms were measured with a time-of-flight (TOF) spectroscopy system employing a supercontinuum white light source, described in detail elsewhere.²⁵

2.2.2 *In vivo clinical validation measurements of skin cancer*

The performance of the system was validated on a total of eight patients (all of skin phototypes I-III) with skin cancers at the Department of Dermatology and Venereology, Skåne University Hospital, Sweden. The study was conducted with the approval of the local ethics committee and in accordance with the ethical principles of the Declaration of Helsinki. Patients were assessed and recruited by the clinical team at outpatient clinics and were going to receive photodynamic therapy (PDT) after the spectral measurements. Three hours prior to PDT, all patients were topically applied with either Ameluz[®] (78 mg/g gel, Biofrontera AG, Germany) or Metvix[®] (160 mg/g, Galderma, France) to the lesion as an approximately 1 mm thick layer including 5 mm of the surrounding normal tissue. The lesions are summarized in Table 1.

Table 1 Summary of the skin lesions in this study. Eight patients were involved in the clinical study, each with one lesion. For each lesion, a number of spots on both the tumor and surrounding normal tissue were measured.

Lesion Type	Patient No.	Number of locations	
		Lesions	Normal tissue
Squamous cell carcinoma <i>in situ</i>	1	6	4
Actinic keratosis	2, 8	11	8
Basal Cell Carcinoma	3, 7	9	8
Parapsoriasis	4	6	4
Alopecia mucinosa	5	6	4
Actinic cheilitis	6	6	4
Total measurements	8	44	32

The spectral measurements on patients were performed right prior to PDT. For each lesion, a couple of locations were measured on both the tumor and neighbouring tissues. The number of measurements, depending on the lesion size, is illustrated in an example image in Fig. 2 and listed in Table 1. After the measurements, the patients received PDT for 14 min.

2.3 *Evaluation protocol*

2.3.1 *Data pre-processing*

The collected pulses on all detectors were pre-processed following the procedure as illustrated by the flowchart in Fig. 3. Within each pulse from one detector, the first and the last two data points were excluded and then an average signal value was calculated. The background, measured as the average value from the time slot when all LEDs were turned off, was then subtracted from all the other measured values of the remaining five time slots. To increase the signal-to-noise ratio,

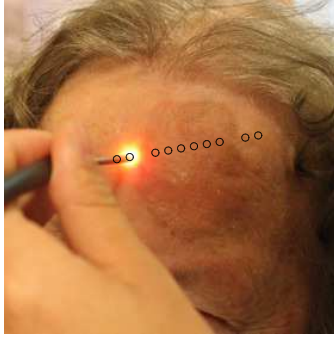


Fig 2 Example image showing the measured locations (circles) of a skin tumor (squamous cell carcinoma *in situ*) on the patient's forehead.

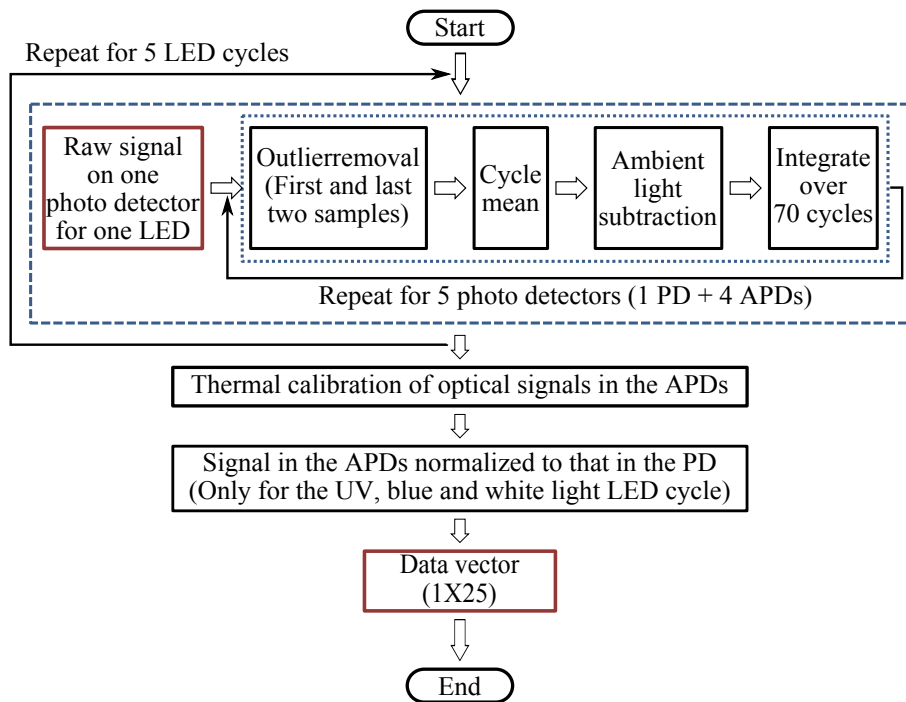


Fig 3 The flowchart of data pre-processing to retrieve the spectral data for one measurement location on a sample.

the signal was averaged over 70 light cycles, corresponding to a total integration time of 90 ms. Thereafter the APD data were divided by the corresponding PD data for the UV, blue and white light LED cycle, in order to compensate for the source fluctuation and tissue attenuation. Such a data pre-processing procedure would result in a data vector of size 1×25 for measurement on one sample spot.

For multiple samples, the data vector was joined to generate a matrix, M , each row representing the data vector for one measurement location.

2.3.2 Least squares support vector machines

A milestone of the Support Vector Machines (SVMs) algorithm was proposed by Cortes and Vapnik for solving two-group classification problems in 1995.²⁶ In short, the principle can be in-

terpreted as the idea that the observations in the input space are transformed non-linearly to a high-dimensional feature space, where an optimal linear separating hyperplane (with a maximized distance between the margins) is constructed with the training data to achieve good separation. The kernel trick realizes the non-linear feature transformation without explicitly computing the feature mapping function, if given the kernels (i.e. inner product of data point pairs in the feature space). Usually, a quadratic optimization problem (QOP) needs to be solved to determine the optimal hyperplane. SVMs have now been developed also for multi-class separation and function estimation (or regression).

LS-SVM is a simplified and recent derivative version of the standard SVMs,²⁷ which suffer from a major drawback of its high computational burden for the constrained QOP programming.²⁸ Instead of solving a QOP, LS-SVM works with solving linear equations. This makes LS-SVM much faster than the standard SVMs.^{23,28} In this work, LS-SVM was thus chosen for both regression (quantification of PpIX concentrations and tissue optical properties) and classification of tissue types (optical diagnostics of skin tumors) from the spectroscopic measurements. The readers are referred to the literatures elsewhere^{23,26,27,29} for the details of the theory of SVMs and LS-SVM.

For LS-SVM, a Gaussian radial basis function (RBF) kernel was used. Despite the data matrix M containing the spectral observations, there are two additional input parameters needed. They are (1) the kernel parameter, σ , defining the kernel width, and (2) regularization parameter, γ , determining the trade-off between the training error minimization and smoothness. A simplex algorithm was applied to tune and optimize these two model hyperparameters.

2.3.3 Ambient light rejection

The ability to suppress any influences from ambient light was tested with intralipid ink phantoms at a fixed PpIX concentration of 100 nM in the laboratory measurements. Light from a halogen lamp (Photonic; PL2000) was guided by a fiber optic microscope illuminator, composed of an optical fiber bundle with a ring-light-shaped distal end (Photonic Optics, Austria; PL1000) onto the phantom. To obtain various illumination conditions, the position of the ring-light was adjusted up and down above the sample at a distance of maximal 60 cm, while the sample and probe were kept fixed. The fluence rate of the ambient light at the top surface of the phantoms was measured with a Panlux 2 Electronic Lux Meter (Gossen Foto- u. Lichtmesstechnik GmbH).

2.3.4 System quantification calibration

For quantification of PpIX in intralipid ink phantoms under the test on ambient light rejection, the ninth value in the data vector in Fig. 3 was used, which is a ratio:

$$R_F = F_{635}/R_{405}, \quad (4)$$

where F_{635} denotes PpIX fluorescence intensity detected from the 635 nm APD channel, indicating the PpIX fluorescence peak under 405-nm excitation. Correspondingly, the reflectance from the 405 nm channel is denoted by R_{405} .

LS-SVM regression was employed to create three non-linear models to predict $\mu'_s(635)$, blood volume fraction (denoted by [Blood]) and PpIX molar concentration (denoted by [PpIX]) in the intralipid blood phantoms. Each model was made from the pre-processed data matrix M and a corresponding data column consisting of true values. In the data analysis 269 phantoms were

included and one phantom was excluded because of obvious misoperation. Each prediction model was validated by the two-fold cross-validation (CV) methodology: the phantom dataset was split into one subset for calibration (training) and the other one for validation (testing). The correlation coefficient, R^2 for the training set and Q^2 for the testing set, both percent coefficient of variation (Cov, defined as $SD/mean$) and the percent error ($mean \pm SD$) for each set of predicted quantities, were calculated to evaluate the precision of the validation model.

2.3.5 Clinical quantification validation

The signals measured from the skins were pre-processed and the APD signals were temperature calibrated prior to normalization with reflectance. The [PpIX], $\mu'_s(635)$ and [Blood] for the tissue samples were predicted by three LS-SVM regression models, where all the phantom dataset were used for training with leave-one-out cross-validation (LOOCV), following the procedure described in Section 2.3.4.

2.3.6 Clinical tissue classification

The clinical data was classified using LS-SVM for tissue diagnostic purpose. Here in the classification model, the tissue type was assigned to logical 1 for tumor lesions and 0 for the surrounding healthy tissue according to the histological diagnosis. The model was trained and tested with LOOCV.

3 Results

3.1 Optical properties of phantoms

For the phantoms with 3~8% intralipid, $\mu'_s(635)$ were calculated to be 7.7~20.4 cm^{-1} from Eq. 3. From the TOF measurement, $\mu'_s(635)$ was determined to be 8.9 cm^{-1} for 3.75% intralipid and $\mu_a(635)=0.020$ cm^{-1} for 0.25% ink or 0.11 cm^{-1} for 3% blood.

3.2 Ambient light rejection

How much the performance of the system is affected by the ambient light level is shown in Fig. 4. The raw fluorescence signal in (a) clearly shows increasing levels of disturbance due to the ambient light from the white light lamp for an increased light fluence rate. The light level can be represented by the DC level of the fluorescence intensity. The ratio in (b) takes the source power fluctuation into account. For a large variation in the ambient light level (from 15 to 2300 lm/m^2), the ratio in (c) only exhibits a variation of approximately 12%, showing that our probe system is significantly insensitive to the ambient light with a much higher light level than the scenarios from operation lamps.

3.3 System quantification calibration

The quantification responses of the LS-SVM regression model with two-fold CV to predict $\mu'_s(635)$, [Blood] and [PpIX] for the phantoms are shown in Fig. 5. The correlation coefficients for the training and testing datasets are calculated to exceed 0.990 and 0.983, respectively. The mean percentage error (mPE) of the predicted values is 3% with a maximum of 4% for $\mu'_s(635)$, 5% with a maximum of 8% for blood concentration. For PpIX, the mean percentage error (mPE) is 8% for all [PpIX] involved and 5% for relatively high [PpIX] ranging from 400 to 1000 nM. Correspondingly,

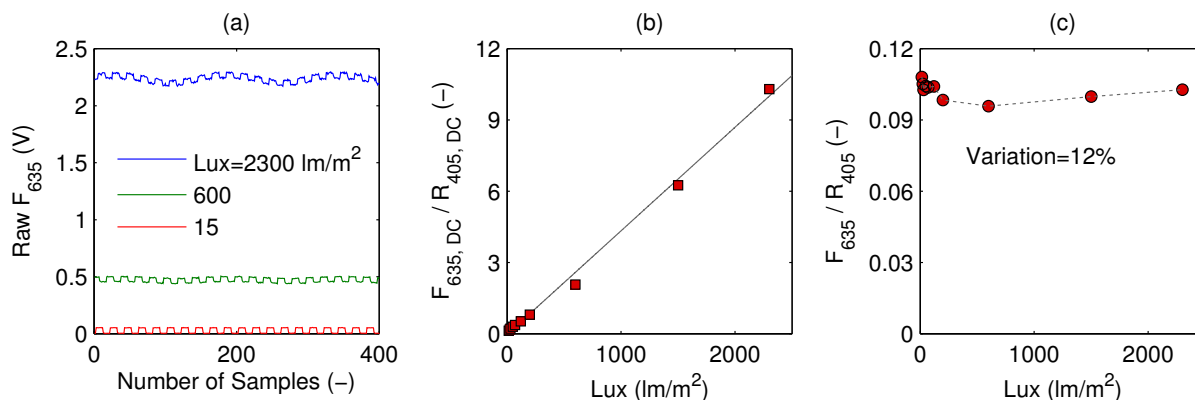


Fig 4 Sensitivity of the fluorophore quantification performance to the ambient light level under the 405-nm excitation, modulated by a TTL pulse at 777 Hz, for a fixed PpIX concentration of 100nM in an intralipid ink phantom with $\mu_a = 0.020 \text{ cm}^{-1}$ and $\mu'_s = 8.90 \text{ cm}^{-1}$ at 635 nm. (a) Example raw fluorescence signals under different ambient light conditions. The sinusoidal pattern of the ambient light can be easily seen for a high lux. For clarity, only signals for a few of the lux levels are shown here; (b) Ratio of the DC level of F_{635} and DC level of R_{405} ; and (c) the ratio of F_{635}/R_{405} versus the ambient light level with a maximum variation of 12%. Solid line in (b) indicates a linear fit to the data.

the mean Cov was calculated to be 3% for $\mu'_s(635)$, 7% for [Blood], 11% for all [PpIX] and 6% for higher [PpIX]. It indicates in general a very good quantification performance for a large variation of optical properties and low fluorophore concentrations in the nM regime.

3.4 Clinical quantification validation

Using the LS-SVM regression model created from the data of the entire phantom dataset, the reduced scattering coefficient at the emission wavelength, blood volume fraction and PpIX molar concentration of the skin under investigation are shown in Fig. 6. The model predicts in general a higher blood content and higher PpIX concentration for the tumor lesions than the normal skin. The two clusters could be employed to classify tissue types for diagnostic purpose.

3.5 Clinical tissue classification

The classification responses for discrimination between normal tissue and tumor lesions involved in the clinical study are shown in Fig. 7(a). The LS-SVM model indicates a significant diagnostic capability with 100% accuracy. Fig. 7(b) shows an example of fluorescence and reflectance signals at 405-nm excitation for one selected patient.

4 Discussions

One of the particular benefits of our probe is that it has overcome the challenge for the fluorescence spectroscopy system to be used in the operating theatre with strong ambient light always present. In the case of brain tumor resection surgery, the surrounding light sources include fluorescence tubes, surgical lamps, and the high power surgical microscope.¹⁶ The suppression of ambient light of our instrument was achieved by a fast pulse modulation of the excitation source in combination with the lock-in like detection. In this way the ambient light level is monitored simultaneously and

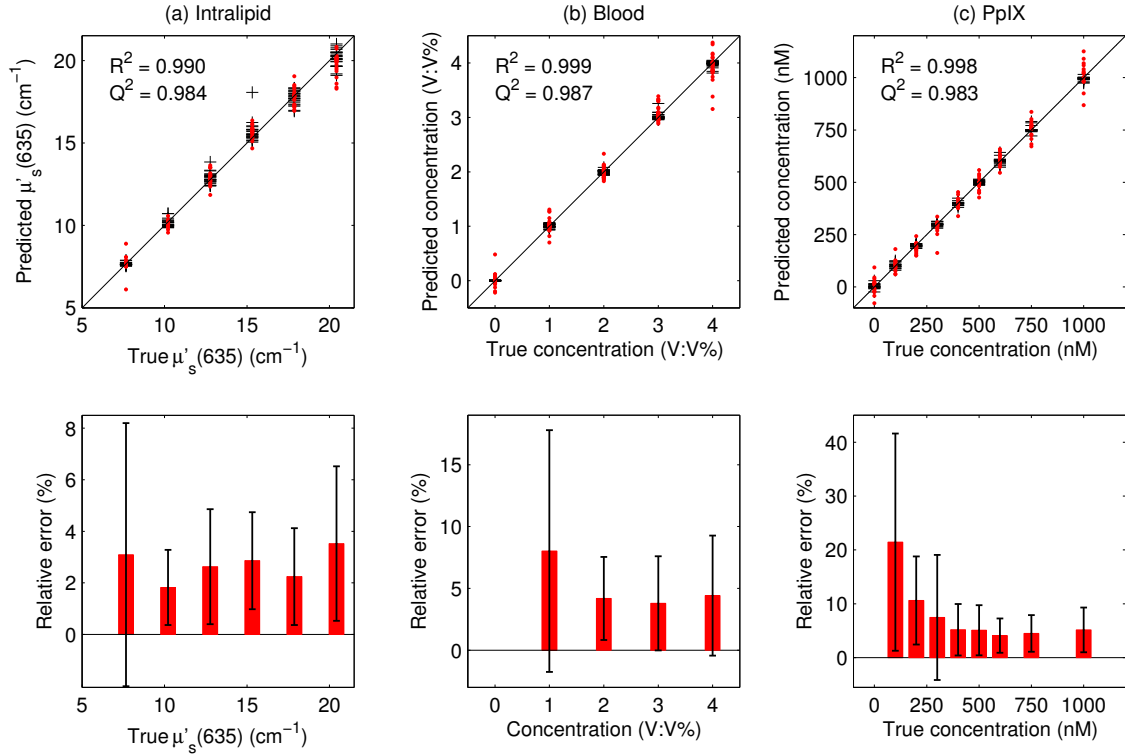


Fig 5 (Top row) PpIX quantification in intralipid blood phantoms with various optical properties using LS-SVM regression with two-fold cross validation (135 samples for training and 134 samples for validation). The dark solid lines indicate the diagonal of best prediction (coordinates 1: 1). R^2 and Q^2 are the correlation coefficients between the true parameter and model response for training and validation, respectively. (Bottom row) Relative error of the predicted parameters (mean \pm SD). The data have not been temperature calibrated because of a long waiting time of ~ 4 h prior to measurement.

then subtracted from the detected optical signals. This design has two major advantages; first, it significantly improves the signal-to-background ratio in the analyzed signals. A recently published work by Sexton *et al.* has demonstrated that pulsed excitation light and time-gated detection technique provides superior sensitivity *in vivo* and can realize fluorescence imaging in room light for FGS.³⁰ However, our system is less expensive, simpler and safer for the eyes compared to LEDs. The modulation at a kHz frequency regime in our design allows detection of weak fluorescence signal in presence of strong ambient light up to 2300 lm/m² in our phantom experiments (see Fig. 4). An even higher signal-to-background light ratio could be expected with a faster modulation frequency, which should not be any problem to increase to orders of magnitudes in-house, even though this level would be sufficient for clinical use. Second, it does not disturb the standard surgical workflow as the previous design,^{4,31} as it is neither necessary to employ an umbrella-like cover on the probe shading the tip, nor take a separate background reference measurement.

APDs are employed as photo detectors for fluorescence spectroscopy with weak light signals in our system. The APDs possess high light-detection sensitivity (gain ~ 50) with high dynamic range as well as fast read out capability (no serial read out from a large CCD chip). The improved sensitivity of APDs over conventional PDs and spectrometers together with the modulation scheme enables efficient removal of the ambient light, providing an exquisite sensitivity to PpIX

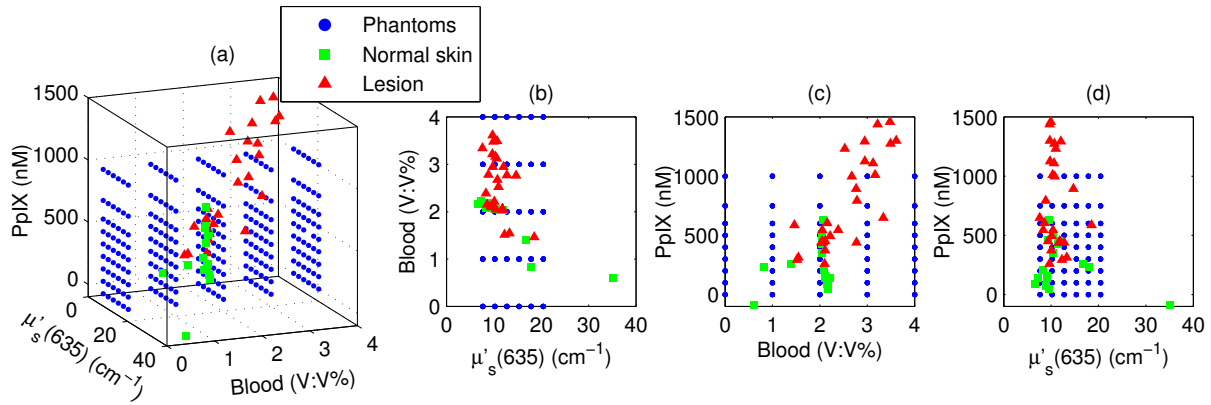


Fig 6 System quantification validation to predict the scattering coefficient at the emission wavelength, blood content and fluorophore concentration of the skin from the data measured at the clinic. The LS-SVM model was created and optimized by leave-one-out cross-validation from 269 phantoms with different amounts of scatters, absorbers and fluorophores (Blue dots). The testing dataset includes measurements of 76 locations in total (44 skin tumor lesions and 32 normal skins). (a) 3D scatter plot, and (b)-(d) are the corresponding 2D projections. The model predicts in general a higher blood content and higher PpIX concentration for the tumor lesions than the normal skin.

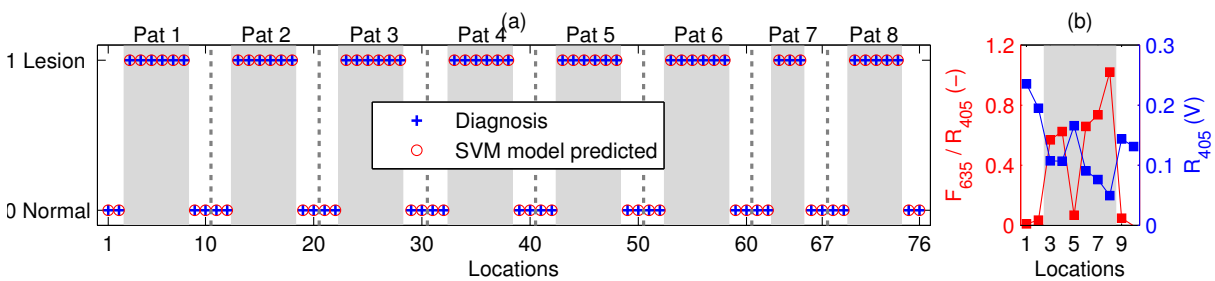


Fig 7 (a) Classification performance of the diagnoses of skin lesions using LS-SVM with leave-one-out cross-validation. The model discriminates successfully in 100% of the cases. (b) As an example, the reflectance signal and the ratio of drug fluorescence peak and reflectance at the 405-nm excitation for one selected patient (Pat 2) are shown. Note that Location 5 has a low normalized fluorescence signal, which might be a result of low blood content (high reflectance) rather than a low PpIX concentration.

fluorescence. In our phantom validation study, PpIX could be precisely quantified in the order of nanomolars in presence of high scattering and absorption. Such concentrations are far below expected tumor tissue concentrations in clinical scenarios. For example, the absolute PpIX concentration was found to be $5.8 \pm 4.8 \mu\text{M}$ (mean \pm SD) in the human high-grade gliomas tissues and $0.2 \pm 0.4 \mu\text{M}$ for grade III brain tumors.³² For ALA-mediated skin-PDT, topical application of ALA was reported to result in a PpIX concentration of 1-2 μM for various human skin malignancies.³³ Due to the high fluorophore sensitivity of our system, it is possible to reduce the ALA dose for intracranial tumor fluorescence purpose (commonly used at 20 mg/kg body weight.²¹), and thus minimize the adverse side effects in patients undergoing operation and not affect normal brain. Owing to the higher photosensitivity of APD, it is also possible to reduce the power of the excitation light in order for a less fluorophore photobleaching, which could perturb the optical diagnostics.

A slight complication with this setup is that APDs suffers from its extremely high sensitivity to temperature (the sensitivity varies typically a couple of percent per degree Celsius). This effect originates from its operation with high reverse bias voltage to achieve desired high photo sensitivity. This temperature variation issue has been effectively solved in our system by thermal calibration with compact thermistors rather than direct control of APD temperature. Such a design does not significantly increase the instrument costs and complexities in surgical operation.

It is well known that one main challenge of fluorescence-based diagnostic methods comes from varying light attenuation by the tissues. Fig. 7(b) shows that the optical properties vary much for different locations, leading to a change in the reflectance at the excitation wavelength. This results in the difficulties in tissue classification using a single excitation wavelength (*e.g.*, see Location 5). In our system, multiple light sources are employed for fluorescence and reflectance spectroscopy. The monitoring of the reflectance is aimed to provide signals to enable to compensate the detected fluorescence signals for tissue optical properties as well as to correct for source power fluctuation by normalizing the APD signals to that from the PD. In the phantom calibration experiments, a wide range of both scattering ($\mu'_s(635)=7.7\sim 20.4 \text{ cm}^{-1}$) and absorption (0~4% blood) have been covered. The results of the multivariate analysis (*i.e.* non-linear LS-SVM regression) indicate that despite the large variation in the optical properties, the detected fluorescence signals correlate linearly to the true fluorophore concentrations (see Fig. 5). Both the significantly high correlation coefficient (>0.98) and the low percent error in the predicted [PpIX] (less than 5% for $400 \text{ nM} \leq [\text{PpIX}] \leq 1 \mu\text{M}$) show that the LS-SVM regression model works pretty well to accurately predict the fluorophore concentrations in the presence of large optical properties variations. Our results are in general better than those in the literature using fluorescence spectroscopy. The comparisons of the quantification performance for PpIX in tissue phantoms with the other designs reported are summarized in Table 2. Kim *et al.*³⁴ used a fiber optic probe and an analytical equation derived from the diffusion theory to estimate [PpIX]. They reported a root mean square deviation from mean of 10.1% and a Cov value of 14% at a fixed [PpIX] of 5 $\mu\text{g}/\text{ml}$ (or 8.9 μM). A recently published work by Valdes *et al.*³⁵ reported a COS imaging system to measure [PpIX] with a CMOS array. They obtained a mean error of 6% and a Cov of less than 10% for [PpIX] in the range between 36 nM and 8.9 μM . However, the optical properties of the phantoms vary less than those in our study. Moreover, slight limitations of their study include the priori knowledge of the optical properties at the excitation wavelength and the inherent limitations that certain assumptions had to be made in the diffusion model. Besides the fluorophore concentration, our LS-SVM regression model can also accurately quantify the reduced scattering coefficient and blood content of the

media. Fig. 5 indicates that our combined fluorescence/reflectance probe in addition to obtaining the [PpIX] accurately, also has achieved a slightly higher quantification accuracy (relative error less than 3% for μ'_s , and 4% for [Blood]) than another recently published study based on spatially resolved diffuse reflectance.⁹ In their study, the mPE of μ'_s and μ_a values were accurate to 4.3% and 5.4%, respectively, when compared with integrating sphere estimates.

Table 2 Comparison of the quantification performance for PpIX in tissue phantoms in this work and the other designs reported, where ^amPE stands for mean percent error; ^bmCov stands for mean coefficient of variation; and ^cR² is the correlation coefficient.

	This work		Kim <i>et al.</i>³⁴	Valdes <i>et al.</i>³⁵
System Design	Fiber optic probe		Fiber optic probe	CMOS camera
Quantification Approach	Multivariate analysis (LS-SVM)		Diffusion theory	Diffusion theory
Number of Phantoms	134	75	54	54
[PpIX] (nM)	100~1000	400~1000	8900	36~8900
mPE^a (%)	8	5	-	6
mCov^b (%)	11	6	14	<10
R² ^c	0.983	-	0.976	0.92
$\mu'_s(635)$ (cm⁻¹)	7.7~20.4		-	8.7~14.5

Other challenges of the fluorescence technique include its superimposition with tissue autofluorescence and complex tissue structures, which may also aggravate the problem of inaccurate fluorophore quantification and thereby tissue diagnostics. There is apparently no doubt that adequate information should be provided for diagnostics in clinical practice. In our design, the 365-nm and the 405-nm can excite tissue autofluorescence which has the potential to provide extra tissue structure information. Meanwhile, the drug fluorescence is superimposed with tissue autofluorescence at the 405 nm excitation wavelength. All the factors mentioned above have been taken into account by the multivariate analysis of the clinical data, where no hypothesis for the light model needs to be made. As shown in Fig. 6, generally very realistic quantification results have been achieved in terms of a higher blood content and higher PpIX concentration for the tumor lesions than the normal skin. The obtained [PpIX] is consistent with the values reported for various human skin malignancies with topically applied ALA.³³ Such clusters could be used for tissue classification purpose. However, one location for normal skin was predicted to have a much higher $\mu'_s(635)$ (>30 cm⁻¹) than the others, which is obviously not likely to be true. In principle, a much larger calibration dataset is required to cover all the possible parameters to be studied in order to improve the quantification performance of the probe for clinical *in vivo* studies.

When the *in vivo* clinical data from the skin lesions were employed to train the non-linear LS-SVM model for the tissue classification purpose, 100% diagnostic accuracy was obtained, as can be seen in Fig. 7(a). It again indicates complicated non-linear dependency of the drug fluorescence signal of many other factors rather than only the fluorophore concentration. A similar study on

skin basal cell carcinomas by Thompson *et al.* using fluorescence/diffuse reflectance spectroscopy together with a linear singular value decomposition analysis yielded diagnostic accuracy of 87%.³⁶ Such comparison suggests the potential of using the probe with multiple sources and non-linear analysis of the spectral data to aid tissue diagnosis.

The results of the clinical data shown in this paper (Figs. 6 and 7) are still preliminary as the database is still under development. However, on the other hand, it already gives a good indication of what might be achievable. A large and accurate enough calibration dataset is a common prerequisite for all multivariate-analysis-based methods. Fig. 7 has already shown a significant discrimination ability even with the small dataset which has been got so far. The obtained clusters in Fig. 6, if combined with a certain classification method, could also provide diagnostics. However, the values obtained here are not very accurate, because of the difference in the tissue phantoms and human tissue with different tumor models, such as tissue autofluorescence and oxygen saturation (the ratio between oxy- and deoxyhemoglobin concentrations). Therefore, we did not proceed to discriminate tissue type. However, it is still interesting to show the potential of the idea for quantification of both fluorophore concentration and tissue optical properties. In the future, the training dataset would be more preferable to be created based on the clinical measurements. Furthermore, the method needs more validation data in order to have a good statistics on the diagnostic performance.

A slight limitation of our instrument is that the delivery fibers for different light sources at the fiber probe tip are aligned in a circle with a diameter of approximately 2.3 mm. This means that the interrogation volume is not exactly the same for each light source. In case of inhomogeneous tissues, especially tumors of small size and irregular tissue structure, it would lead to an inaccurate quantification of fluorophores and thus wrong optical diagnosis. In future clinical studies, it would be good to replace the current probe with dual fibers at the probe tip in order to minimize the probe volume.

From a light source perspective, there might be other reasons for the quantification error in our probe system. A white LED is employed to monitor tissue reflectance at wavelengths of interest. In fact, the white LED consists of a blue LED peaked at 470 nm with a Ce:YAG crystal in front, emitting broad band yellow light from 500 to 700 nm. This elastic light tail towards long wavelengths is possible to leak into the fluorescence bands. To minimize such leakage, the white LED should have a short-pass filter, *e.g.* UG1 or UG11. In addition, the fluorescence of the Ce:YAG crystal is extremely efficient and sometimes not negligible. Therefore, when the 365-nm and 405-nm LEDs are lit up, the elastic violet light will scatter into both the collection fiber and the fiber connecting the white LED. The last mentioned could convert to yellow light by the crystal, travel back to the tissue sample and then superimpose on the tissue and drug fluorescence. Ideally this potential issue could be solved in the future by equipping the white LED with a long-pass GG475 filter.

Further improvements could be made to explore its diagnostic potential of the probe system. An electric high-pass AC filter could be added in each transimpedance amplifier, making the system blind to the DC signal level prior to the analog-to-digital conversion in the DAQ board. This would thus take use of the full dynamic range of the DAQ while without saturating the detector for high signal levels; Furthermore, the green and red LEDs could be easily replaced with additional excitation band (*e.g.* at 445 nm) to evaluate the effects of tissue oxygenation over the ultraviolet-visible spectrum³⁷ and/or acquire the multi-excitation fluorescence in order to form a

two-dimensional excitation emission matrix.³⁸ It has the potential to improve cancer diagnostics by providing absorption and fluorescence characteristics of normal and abnormal tissues.^{38,39}

Point measurements are usually time consuming. However, the probe presented in this work is not going to be used alone for tumor delineation for the entire tumor border especially in the open brain surgery, although it is technically independent of other neurosurgical equipment. It is meant to be used in combination with other systems, for instance, an intraoperative ultrasonic navigation system and the fluorescence surgical microscope.⁵ This is to say, it is meant as a complement to microscopy to check only those uncertain sites which emit very weak fluorescence signals from the tumor tissue (invisible to the surgeons eyes).

In conclusion, we present a fiber optic probe instrument with fluorescence/reflectance spectroscopy for therapy guidance and monitoring. It is meant as a complement to the state-of-the-art neurosurgical fluorescence microscopy for FGS of brain tumor using 5-ALA-induced PpIX as a fluorescence contrast agent. The probe is clinically-adapted to minimize the disruption of the standard surgical workflow. Multiple sources using LEDs with fast pulse modulation and lock-in like detection enable precise quantification of the fluorophore concentration, tissue optical properties and ambient light suppression. We have shown that the probe system is insensitive to strong ambient light up to 2300 lm/m². Validation measurements of tissue phantoms using the LS-SVM regression demonstrate that even with large variations in phantom optical properties, a low quantification error of less than 5% has been obtained for PpIX concentration ranging from 400 nM to 1000 nM which is far below the concentration in the high grade human brain tissue samples. The LS-SVM classification model yields 100% diagnostic accuracy for in vivo skin tumors with topically applied ALA. In principle, the probe is generic to quantify other fluorophores than PpIX in many tissue types.

Acknowledgments

The authors gratefully acknowledge Prof. Karin Wårdell, Dr. Neda Haj-Hosseini and M.D. Johan Richter for the critically important discussions on the clinical adaptations. We would also thank Sören Johansson and Alfi Shaharin for conducting the TOF measurements of tissue phantoms. We also thank Prof. Katarina Svanberg for her valuable discussions and Åke Johansson for his advices and efforts on the electronic components. This work was supported by the Swedish Foundation for Strategic Research (SSF), the Swedish Research Council (VR), the Swedish Governmental Agency for Innovation Systems (Vinnova) under Grant No. 331-2006-7661, a Linnaeus Research Grant to the Lund Laser Center and Elekta AB, Stockholm, Sweden.

References

- 1 U. Utzinger and R. R. Richards-Kortum, "Fiber optic probes for biomedical optical spectroscopy," *J Biomed. Opt.* **8**(1), 121–147 (2003). [doi:10.1117/1.1528207].
- 2 S. Andersson-Engels, Å. Elner, J. Johansson, S. E. Karlsson, L. G. Salford, L. G. Strömblad, K. Svanberg, and S. Svanberg, "Clinical recording of laser-induced fluorescence spectra for evaluation of tumour demarcation feasibility in selected clinical specialities," *Lasers Med. Sci.* **6**(4), 415–424 (1991). [doi:10.1007/bf02042464].
- 3 C. af Klinteberg, M. Andreasson, O. Sandstrom, S. Andersson-Engels, and S. Svanberg, "Compact medical fluorosensor for minimally invasive tissue characterization," *Rev. Sci. Instrum.* **76**(3), 034303 (2005). [doi:10.1063/1.1867569].

- 4 N. Haj-Hosseini, J. Richter, S. Andersson-Engels, and K. Wårdell, "Optical touch pointer for fluorescence guided glioblastoma resection using 5-aminolevulinic acid," *Laser Surg. Med.* **42**(1), 9–14 (2010). [doi:10.1002/Lsm.20868].
- 5 J. C. Richter, N. Haj-Hosseini, S. Andersson-Engel, and K. Wårdell, "Fluorescence spectroscopy measurements in ultrasonic navigated resection of malignant brain tumors," *Laser Surg. Med.* **43**(1), 8–14 (2011). [doi:10.1002/lsm.21022].
- 6 P. A. Valdes, A. Kim, F. Leblond, O. M. Conde, B. T. Harris, K. D. Paulsen, B. C. Wilson, and D. W. Roberts, "Combined fluorescence and reflectance spectroscopy for *in vivo* quantification of cancer biomarkers in low- and high-grade glioma surgery," *J Biomed. Opt.* **16**(11), 116007 (2011). [doi:10.1117/1.3646916].
- 7 D. J. Cappon, T. J. Farrell, Q. Fang, and J. E. Hayward, "Fiber-optic probe design and optical property recovery algorithm for optical biopsy of brain tissue," *J Biomed. Opt.* **18**(10), 107004 (2013). [doi:10.1117/1.jbo.18.10.107004].
- 8 T. M. Baran, M. C. Fenn, and T. H. Foster, "Determination of optical properties by interstitial white light spectroscopy using a custom fiber optic probe," *J Biomed. Opt.* **18**(10), 107007 (2013). [doi:10.1117/1.jbo.18.10.107007].
- 9 A. Kim, M. Roy, F. Dadani, and B. C. Wilson, "A fiberoptic reflectance probe with multiple source-collector separations to increase the dynamic range of derived tissue optical absorption and scattering coefficients," *Opt. Express* **18**(6), 5580–5594 (2010). [doi:10.1364/oe.18.005580].
- 10 J. Swartling, J. Axelsson, G. Ahlgren, K. M. Kälkner, S. Svanberg, K. Svanberg, S. Andersson-Engels, and S. Nilsson, "System for interstitial photodynamic therapy with online dosimetry: first clinical experiences of prostate cancer," *J Biomed. Opt.* **15**(5), 058003 (2010). [doi:10.1117/1.3495720].
- 11 S. C. Kanick, C. van der Leest, J. G. J. V. Aerts, H. C. Hoogsteden, S. Kaščáková, H. J. C. M. Sterenberg, and A. Amelink, "Integration of single-fiber reflectance spectroscopy into ultrasound-guided endoscopic lung cancer staging of mediastinal lymph nodes," *J Biomed. Opt.* **15**(1), 017004 (2010). [doi:10.1117/1.3290822].
- 12 V. R. Sauvage, A. P. Levene, H. T. Nguyen, T. C. Wood, H. Kudo, D. Concas, H. C. Thomas, M. R. Thursz, R. D. Goldin, Q. M. Anstee, and D. S. Elson, "Multi-excitation fluorescence spectroscopy for analysis of non-alcoholic fatty liver disease," *Laser Surg. Med.* **43**(5), 392–400 (2011). [doi:10.1002/lsm.21064].
- 13 M. R. Austwick, B. Clark, C. A. Mosse, K. Johnson, D. W. Chicken, S. K. Somasundaram, K. W. Calabro, Y. Zhu, M. Falzon, G. Kocjan, T. Fearn, S. G. Bown, I. J. Bigio, and M. R. S. Keshtgar, "Scanning elastic scattering spectroscopy detects metastatic breast cancer in sentinel lymph nodes," *J Biomed. Opt.* **15**(4), 047001 (2010). [doi:10.1117/1.3463005].
- 14 G. M. Palmer, C. F. Zhu, T. M. Breslin, F. S. Xu, K. W. Gilchrist, and N. Ramanujam, "Monte Carlo-based inverse model for calculating tissue optical properties. part II: Application to breast cancer diagnosis," *Appl. Opt.* **45**(5), 1072–1078 (2006). [doi:Doi 10.1364/Ao.45.001072].
- 15 G. M. Palmer, R. J. Viola, T. Schroeder, P. S. Yarmolenko, M. W. Dewhirst, and N. Ramanujam, "Quantitative diffuse reflectance and fluorescence spectroscopy: tool to monitor tumor physiology *in vivo*," *J Biomed. Opt.* **14**(2), 024010 (2009). [doi:10.1117/1.3103586].

- 16 M. Brydegaard, N. Haj-Hosseini, K. Wårdell, and S. Andersson-Engels, “Photobleaching-insensitive fluorescence diagnostics in skin and brain tissue,” *IEEE Photon. J* **3**(3), 407–421 (2011). [doi:10.1109/jphot.2011.2141656].
- 17 P. A. Valdes, F. Leblond, A. Kim, B. T. Harris, B. C. Wilson, X. Y. Fan, T. D. Tosteson, A. Hartov, S. B. Ji, K. Erkmén, N. E. Simmons, K. D. Paulsen, and D. W. Roberts, “Quantitative fluorescence in intracranial tumor: implications for ala-induced ppix as an intraoperative biomarker,” *J Neurosurg.* **115**(1), 11–17 (2011). [doi:10.3171/2011.2.jns101451].
- 18 B. Kruijt, S. Kascakova, H. S. de Bruijn, A. van der Ploeg-van den Heuvel, H. J. C. M. Sterenborg, D. J. Robinson, and A. Amelink, “*In vivo* quantification of chromophore concentration using fluorescence differential path length spectroscopy,” *J Biomed. Opt.* **14**(3), 034022 (2009). [doi:10.1117/1.3149862].
- 19 B. W. Pogue, S. L. Gibbs-Strauss, P. A. Valdes, K. S. Samkoe, D. W. Roberts, and K. D. Paulsen, “Review of neurosurgical fluorescence imaging methodologies,” *IEEE J Sel. Top. Quantum Electron.* **16**(3), 493–505 (2010). [doi:10.1109/jstqe.2009.2034541].
- 20 M. Hefti, H. M. Mehdorn, I. Albert, and L. Dorner, “Fluorescence-guided surgery for malignant glioma: a review on aminolevulinic acid induced protoporphyrin IX photodynamic diagnostic in brain tumors,” *Curr. Med. Imaging Rev.* **6**(4), 254–258 (2010). [doi:10.2174/157340510793205503].
- 21 M. J. Colditz, K. V. Leyen, and R. L. Jeffree, “Aminolevulinic acid (ALA)-protoporphyrin IX fluorescence guided tumour resection. Part 2: Theoretical, biochemical and practical aspects,” *J Clin. Neurosci.* **19**(12), 1611–1616 (2012). [doi:10.1016/j.jocn.2012.03.013].
- 22 W. Stummer, A. Novotny, H. Stepp, C. Goetz, K. Bise, and H. J. Reulen, “Fluorescence-guided resection of glioblastoma multiforme by using 5-aminolevulinic acid-induced porphyrins: a prospective study in 52 consecutive patients,” *J Neurosurg.* **93**(6), 1003–1013 (2000). [doi:10.3171/jns.2000.93.6.1003].
- 23 K. Pelckmans, J. A. K. Suykens, T. Van Gestel, J. De Brabanter, L. Lukas, B. Hamers, B. De Moor, and J. Vandewalle, “Ls-svmlab: a matlab/c toolbox for least squares support vector machines,” (2011). <http://www.esat.kuleuven.be/sista/lssvmlab/>.
- 24 S. T. Flock, S. L. Jacques, B. C. Wilson, W. M. Star, and M. J. van Gemert, “Optical properties of intralipid: a phantom medium for light propagation studies,” *Laser Surg. Med.* **12**(5), 510–519 (1992). [doi:10.1002/lsm.1900120510].
- 25 E. Alerstam, S. Andersson-Engels, and T. Svensson, “White Monte Carlo for time-resolved photon migration,” *J Biomed. Opt.* **13**(4), 041304 (2008). [doi:10.1117/1.2950319].
- 26 C. Cortes and V. Vapnik, “Support-vector networks,” *Machine Learning* **20**, 273–297 (1995). [doi:10.1023/A:1022627411411].
- 27 J. A. K. Suykens, T. Van Gestel, and J. De Brabanter, *Least Squares Support Vector Machines*, World Scientific (2002).
- 28 H. Wang and D. Hu, “Comparison of SVM and LS-SVM for regression,” *IEEE International Conference on Neural Networks and Brain* **1**, 279–283 (2005). [doi:10.1109/ICNNB.2005.1614615].
- 29 V. N. Vapnik, *Statistical learning theory*, Wiley, 1 ed. (1998).
- 30 K. Sexton, S. C. Davis, D. McClatchy, P. A. Valdes, S. C. Kanick, K. D. Paulsen, D. W. Roberts, and B. W. Pogue, “Pulsed-light imaging for fluorescence guided surgery under normal room lighting,” *Opt. Lett.* **38**(17), 3249–3252 (2013). [doi:10.1364/ol.38.003249].

- 31 M. A. Ilias, J. Richter, F. Westermark, M. Brantmark, S. Andersson-Engels, and K. Wårdell, "Evaluation of a fiber-optic fluorescence spectroscopy system to assist neurosurgical tumor resections," in *Proc. SPIE-OSA*, **6631**, 66310W (2007). [doi:10.1117/12.728546].
- 32 A. Johansson, G. Palte, O. Schnell, J. C. Tonn, J. Herms, and H. Stepp, "5-aminolevulinic acid-induced protoporphyrin IX levels in tissue of human malignant brain tumors," *Photochem. Photobiol.* **86**(6), 1373–1378 (2010). [doi:10.1111/j.1751-1097.2010.00799.x].
- 33 C. Fritsch, P. Lehmann, W. Stahl, K. W. Schulte, E. Blohm, K. Lang, H. Sies, and T. Ruzicka, "Optimum porphyrin accumulation in epithelial skin tumours and psoriatic lesions after topical application of delta-aminolaevulinic acid," *Brit. J Cancer* **79**(9-10), 1603–1608 (1999). [doi:10.1038/sj.bjc.6690255].
- 34 A. Kim, M. Khurana, Y. Moriyama, and B. C. Wilson, "Quantification of *in vivo* fluorescence decoupled from the effects of tissue optical properties using fiber-optic spectroscopy measurements," *J Biomed. Opt.* **15**(6), 067006 (2010). [doi:10.1117/1.3523616].
- 35 P. A. Valdes, V. L. Jacobs, B. C. Wilson, F. Leblond, D. W. Roberts, and K. D. Paulsen, "System and methods for wide-field quantitative fluorescence imaging during neurosurgery," *Opt. Lett.* **38**(1), 2786–2788 (2013). [doi:10.1364/ol.38.002786].
- 36 A. J. Thompson, S. Coda, M. B. Sorensen, G. Kennedy, R. Patalay, U. Waitong-Bramming, P. A. A. De Beule, M. A. A. Neil, S. Andersson-Engels, N. Bendsoe, P. M. W. French, K. Svanberg, and C. Dunsby, "*In vivo* measurements of diffuse reflectance and time-resolved autofluorescence emission spectra of basal cell carcinomas," *J Biophotonics* **5**(3), 240–254 (2012). [doi:DOI 10.1002/jbio.201100126].
- 37 G. M. Palmer, C. L. Marshek, K. M. Vrotsos, and N. Ramanujam, "Optimal methods for fluorescence and diffuse reflectance measurements of tissue biopsy samples," *Laser Surg. Med.* **30**(3), 191–200 (2002). [doi:10.1002/lsm.10026].
- 38 M. Brydegaard, A. Merdasa, H. Jayaweera, J. Ålebring, and S. Svanberg, "Versatile multispectral microscope based on light emitting diodes," *Rev. Sci. Instrum.* **82**(12), 123106 (2011). [doi:10.1063/1.3660810].
- 39 R. A. Zângaro, L. Silveira, R. Manoharan, G. Zonios, I. Itzkan, R. R. Dasari, J. Van Dam, and M. S. Feld, "Rapid multiexcitation fluorescence spectroscopy system for *in vivo* tissue diagnosis," *Appl. Opt.* **35**(25), 5211–5219 (1996). [doi:10.1364/ao.35.005211].

List of Figures

- 1 Schematic diagram of the fiber optic point probe system, illustrating in vivo measurement of a skin lesion on the right leg of a patient. The subplot on the top left shows the real-time raw optical data detected by the five photo detectors, including the PpIX fluorescence, tissue autofluorescence and reflectance spectra. Here the abbreviations in the figure are BS (dichroic beam splitter), LP (long-pass filter), BP (band-pass filter), PD (photodiode), and APD (avalanche photodiode).
- 2 Example image showing the measured locations (circles) of a skin tumor (squamous cell carcinoma *in situ*) on the patient's forehead.
- 3 The flowchart of data pre-processing to retrieve the spectral data for one measurement location on a sample.
- 4 Sensitivity of the fluorophore quantification performance to the ambient light level under the 405-nm excitation, modulated by a TTL pulse at 777 Hz, for a fixed PpIX concentration of 100nM in an intralipid ink phantom with $\mu_a = 0.020 \text{ cm}^{-1}$ and $\mu'_s = 8.90 \text{ cm}^{-1}$ at 635 nm. (a) Example raw fluorescence signals under different ambient light conditions. The sinusoidal pattern of the ambient light can be easily seen for a high lux. For clarity, only signals for a few of the lux levels are shown here; (b) Ratio of the DC level of F_{635} and DC level of R_{405} ; and (c) the ratio of F_{635}/R_{405} versus the ambient light level with a maximum variation of 12%. Solid line in (b) indicates a linear fit to the data.
- 5 (Top row) PpIX quantification in intralipid blood phantoms with various optical properties using LS-SVM regression with two-fold cross validation (135 samples for training and 134 samples for validation). The dark solid lines indicate the diagonal of best prediction (coordinates 1: 1). R^2 and Q^2 are the correlation coefficients between the true parameter and model response for training and validation, respectively. (Bottom row) Relative error of the predicted parameters (mean \pm SD). The data have not been temperature calibrated because of a long waiting time of ~ 4 h prior to measurement.
- 6 System quantification validation to predict the scattering coefficient at the emission wavelength, blood content and fluorophore concentration of the skin from the data measured at the clinic. The LS-SVM model was created and optimized by leave-one-out cross-validation from 269 phantoms with different amounts of scatters, absorbers and fluorophores (Blue dots). The testing dataset includes measurements of 76 locations in total (44 skin tumor lesions and 32 normal skins). (a) 3D scatter plot, and (b)-(d) are the corresponding 2D projections. The model predicts in general a higher blood content and higher PpIX concentration for the tumor lesions than the normal skin.
- 7 (a) Classification performance of the diagnoses of skin lesions using LS-SVM with leave-one-out cross-validation. The model discriminates successfully in 100% of the cases. (b) As an example, the reflectance signal and the ratio of drug fluorescence peak and reflectance at the 405-nm excitation for one selected patient (Pat 2) are shown. Note that Location 5 has a low normalized fluorescence signal, which might be a result of low blood content (high reflectance) rather than a low PpIX concentration.

List of Tables

- 1 Summary of the skin lesions in this study. Eight patients were involved in the clinical study, each with one lesion. For each lesion, a number of spots on both the tumor and surrounding normal tissue were measured.
- 2 Comparison of the quantification performance for PpIX in tissue phantoms in this work and the other designs reported, where ^amPE stands for mean percent error; ^bmCov stands for mean coefficient of variation; and ^cR² is the correlation coefficient.

Papers II

Ambient Light Rejecting Fiber Optic Probe for Brain Tumor Surgical Resection Guidance

Haiyan Xie,* Mikkel Brydegaard Sørensen, Zhiyuan Xie, Monirehalsadat Mousavi, Johan Axelsson, and Stefan Andersson-Engels

Lund University, Department of Physics, P.O. Box 118, SE-221 00, Lund, Sweden

*Correspondence to: Haiyan Xie (E-mail: haiyan.xie@fysik.lth.se).

Abstract: A light emitting diode based fiber optic probe is developed for therapy guidance and monitoring using frequency modulation. The measurement on intralipid phantoms demonstrates high rejection of ambient light. Quantification of PpIX is presented.

OCIS codes: (170.6510) Spectroscopy, tissue diagnostics; (170.4090) Modulation techniques; (120.3890) Medical optics instrumentation

Glioblastoma multiforme (GBM) is the most common highly malignant and aggressive form of primary brain tumor. The challenge to decide the extent of surgical resection in the operating field is to discriminate accurately between tumor and the surrounding functioning healthy tissue. 5-aminolevulinic acid (ALA)-induced protoporphyrin IX (PpIX) fluorescence-guided resection of brain tumors has gained increased clinical interest in the *in vivo* and real-time open brain surgery. It is tumor targeting and then converted to the fluorescent biomarker PpIX in the malignant cells, thus provides the operating surgeon with an intuitive and real-time surgical guidance tool for differentiating the malignant tissue from surrounding healthy tissue. In the pioneering work by Stummer *et al.* [1], the fluorescence microscopy guided resection of malignant gliomas using 5-ALA has been evaluated. Valdés *et al.* reported a fiber optic probe with tumor tissue delineation accuracies up to 94%, by combining fluorescence and reflectance spectroscopy for *in vivo* quantification of cancer biomarkers in glioma surgery [2]. Previously Haj-Hosseini *et al.* developed a fiber optic probe, called optical touch pointer (OTP), for guiding neurosurgical tumor resection [3]. However, a slight limitation with the OTP system is that it is highly sensitive to the surrounding light sources, such as fluorescence tubes and high power microscope lamps, in the operating room (OR). This results from the fact that the integration time of the spectrometer had to be long enough to detect the weak fluorescence signal. Thus, the measurements had to be carried out while shading the measurement region from the direct light, which obviously is a drawback during the surgery.

In this study, we present a novel clinically-adapted fluorescence spectroscopy system based on a lock-in-based hand-held fiber-optic probe, aiming at increasing the sensitivity, diagnostic potential and ability to suppress ambient light. Measurements on intralipid liquid phantoms also clearly show that our system is much less sensitive to the ambient light and has a high sensitivity and the ability to quantify the fluorophore. The system design also allows measurements of the diffuse reflectance at a number of wavelengths of interest and thus provides an ability to conduct relative fluorescence measurement and in this way potentially enables improved diagnostic capabilities, in a similar way as Valdés *et al.* did [2].

The schematic diagram of the probe is shown in Fig. 1. Five fiber coupled LEDs (365, 405, 530, 640 nm and white, respectively) (FC-5, Prizmatix Ltd.) are modulated sequentially by a TTL pulse at 777 Hz with a duty cycle of 50%, generated from the clock output of a data acquisition (DAQ) electronic board (USB-6351, National Instruments). The hand-held fiber probe (Fiber Patch Cord Bundle, Prizmatix) consists of six surrounding delivery fibers and one collection fiber at the center. All the fibers are made of plastic optical fiber, with a core diameter of 750 μm , a length of 4 m, and a NA of 0.50, bundled together into a 5 cm long and 4 mm diameter stainless steel tubing. Light from the LEDs is guided through the five delivery fibers onto the sample. The fluorescence and reflectance light is collected by the collection fiber. After the fiber collimator (64770, Edmund Optics), it is split into 5 different light paths by employing four dichroic beam splitters (BSs) (DMPL425, 505, 567 and 638, Thorlabs). Reflected light is detected by a silicon photodiode (PD) (53378, Edmund Optics). Fluorescence light at different wavelengths is detected by four avalanche photodiodes (APDs) (S9075, Hamamatsu), respectively. In front of each detector, there is a narrowband band pass filter (FB405-10, FB470-10, FB530-10, FB-635-10, and FB-660-10, respectively) and a light focusing lens (47884, Edmund Optics), resulting in a light spot of a diameter less than 1.5 mm on the detectors. To suppress the back-reflected light from reaching the APDs, a long pass cutoff filter (GG-435, Edmund Optics) is fixed between first two BSs. The photocurrent on the detectors is converted to a voltage by five transimpedance amplifiers and measured by the analog inputs of the DAQ board. The detection

components are mounted in a compact home-made black anodized aluminum box, which has a size of 200x120x104 mm³ and a total weight of 2.5 kg, together with the components. TTL pulse generation and signal manipulation is performed by a software developed in LabVIEW[®] (National Instruments), running on a laptop. The whole system together with the laptop is put on a trolley, which is easily carried to and moved in the OR.

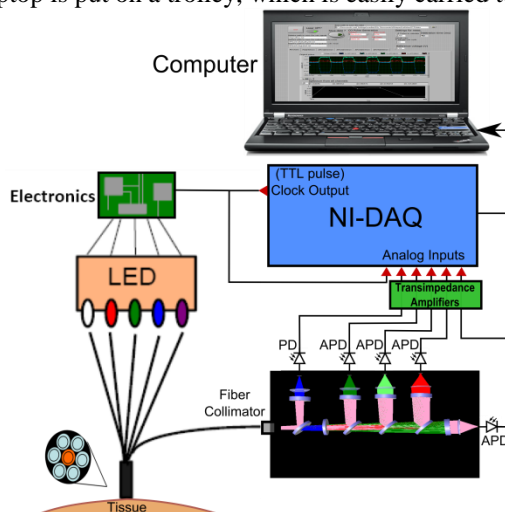


Fig. 1. Schematic diagram of the probe system and fiber probe configuration at the probe tip.

A set of tissue phantoms with various optical properties were prepared by mixing water, intralipid, and ink (or bovine blood). The optical properties were chosen to have a good correspondence to real tissue in small animals. PpIX stock solution was prepared by dissolving PpIX 0.056 g powder (Fischer Scientific) in 20 ml DMSO and 80 ml Water. When diluting the PpIX solution in the tissue phantom, 2% whole volume of Tween (Producer) was added to prevent PpIX from aggregation. The phantoms were stirred for four hours prior to the measurements using a magnetic stirrer and kept stirred during the measurements.

The ability to suppress any influences from ambient light was tested in laboratory measurements. Light from a halogen lamp (PL2000, Photonic) was guided by an optical fiber bundle with a ring-light-shaped distal end to illuminate the sample. To obtain various illumination conditions, the position of the ring-light was adjusted up and down above the sample, while the sample and probe were fixed. The light fluence rate of the ambient light was measured with a Panlux 2 Electronic Luxmeter (Gossen).

The collected pulses on the detectors were processed as described in the following. For each pulse cycle, an average signal value was calculated while the light source was on, subtracted by an average measured value from the time interval with the source off. To increase the signal-to-noise ratio, this difference was averaged over 70 light cycles, corresponding to a total integration time of 90 ms. All the data analysis was performed in the Matlab[®] environment (Mathworks) on a conventional PC.

When the LED source at 405 nm is modulated, PpIX fluorescence intensity detected from the 635 nm channel is denoted by $Fluo(635)$, which indicates the PpIX fluorescence peak. The reflectance from the 405 nm channel is denoted by $Refl(405)$. For the system performance the ratio of these signals was formed:

$$F_R = Fluo(635) / Refl(405) \quad (1)$$

How much the performance of the system is affected by the ambient light level is shown in Fig. 2. The improved sensitivity of APDs over conventional PDs together with the modulation scheme enables efficient removal of the ambient light while exhibiting an exquisite sensitivity to PpIX levels far below expected tissue concentrations. The raw fluorescence signals in (d) clearly show increasing levels of disturbance due to the ambient light from the white light lamp (see the sinusoidal superimposed signal at 100 Hz) for an increased light fluence rates. The light level can be represented by the DC level of the fluorescence intensity in (b), while the ratio in (c) takes the source power fluctuation into account. For a large variation in the ambient light level (from 15 to 2300 lm/m²), the ratio in (a) only exhibits a variation of less than 13%, showing that our probe system is quite insensitive to the ambient light even at high fluence rates, due to the fast modulation frequency of the excitation source in combination with the lock-in detection.

The fluorescence-to-reflectance ratio is plotted as a function of PpIX concentration in Fig. 3 for (a) ink and (b) blood phantoms, respectively. The ratio shows a good linearity to the fluorophore quantities for various set of optical properties.

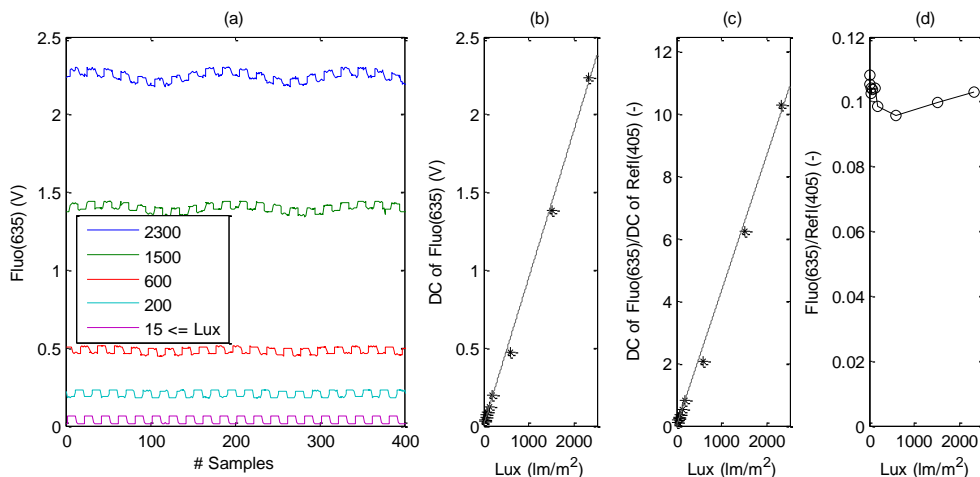


Fig. 2. Sensitivity of the system performance to the ambient light level, for a fixed PpIX concentration of 100nM in an intralipid ink phantom. (a) Example raw fluorescence signals under different ambient light conditions. For clarity, only signals for part of the lux levels are shown here. (b) DC level of Fluo(635), (c) ratio of DC level of Fluo(635) and DC level of Refl(405), and (d) the Fluo(635)/Refl(405) ratio, versus the ambient light level. Solid lines in (b) and (c) indicate a linear fit to the data.

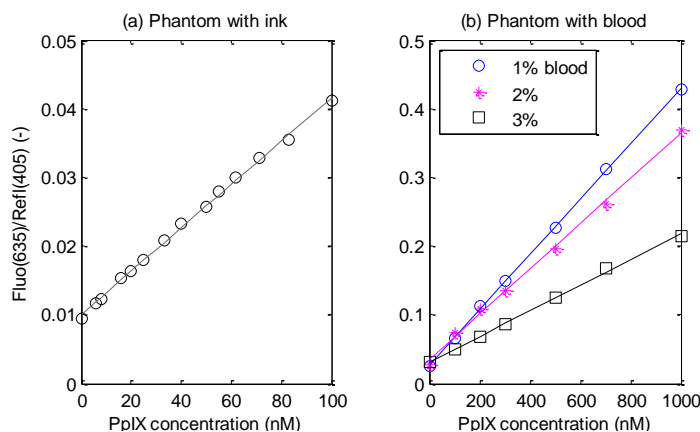


Fig. 3. PpIX quantification in phantoms with various optical properties. (a) Intralipid ink phantoms and (b) intralipid blood phantoms (blood volume of 1%, 2%, and 3%, respectively). Solid line indicates a linear fit to the data.

In conclusion, a fiber optic point probe has been developed with the aim to guide neurosurgical resections of GBM tumors. We have shown that our probe has solved the challenge with strong ambient light always present during such resections. The additional capability of measuring diffuse reflectance at a number of wavelengths increases the diagnostic potential of the system. One can foresee that these signals could enable compensation for e.g. different blood contents in the tissue and source fluctuations. By employing multiple LEDs at several wavelengths it should be possible to compensate for different optical properties of the tissue as well as to also include tissue autofluorescence properties under the UV excitation. These possibilities will contribute to an improved diagnostic potential as compared to previously evaluated systems for this purpose. The next step of this study is to fully explore the diagnostic potential by combining the information of different excitation and detection channels and creating an analytical model to correct the fluorescence signal for tissue absorption and scattering. The performance of the system in clinical measurements on the patients with GBM will also be examined.

References

- [1] W. Stummer, *et al.*, “Fluorescence-guided resection of glioblastoma multiforme utilizing 5-ALA-induced porphyrins: A prospective study in 52 consecutive patients.” *J Neurosurg* **93**:1003–1013 (2000).

- [2] Valdés PA, Kim A, et al., "Combined fluorescence and reflectance spectroscopy for in vivo quantification of cancer biomarkers in low- and high-grade glioma surgery," *J. Biomed. Opt.* 16(11):116007 (2011).
- [3] N. Haj-Hosseini, J. Richter; S. Andersson-Engels, and K. Wårdell, "Optical touch pointer for fluorescence guided glioblastoma resection using 5-aminolevulinic acid," *Lasers Surg Med* **42**, 9-14 (2010).

Papers III

Novel combined fluorescence/reflectance spectroscopy system for guiding brain tumor resections – hardware considerations

Zhiyuan Xie^a, Haiyan Xie^a, Monirehalsadat Mousavi^a, Mikkel Brydegaard^b, Johan Axelsson^a, Stefan Andersson-Engels^a

^aDivision of Atomic Physics, Department of Physics, Lund University P.O. Box 118 SE-221 00, Lund, Sweden ; ^bDivision of Combustion Physics, Department of Physics, Lund University P.O. Box 118 SE-221 00, Lund, Sweden

ABSTRACT

Glioblastoma multiforme (GBM) has long been known as the most common and aggressive form of brain malignancy. The morphological similarities of the malignant and surrounding tissue cause difficulties to distinct the tumors during surgery. In order to achieve better results in resecting malignant brain tumors, a fiber based optical system which can be used intraoperative is developed in this project. In this context, the system hardware details, system controlling interfaces and laboratory testing results are presented.

Based on the results obtained from various tests with tissue-equivalent phantoms, the system is proved to have stable performance, robust structure, and have good linearity as well as high sensitivity to low PpIX concentration under strong ambient light conditions.

Keywords: Glioblastoma multiforme (GBM), tumor resection, PpIX fluorescence, fiber optical probe, ambient light rejection.

1. INTRODUCTION

Glioblastoma multiforme (GBM) is the most common and aggressive form of diffuse astrocytoma. It presents a low survival rate and short surviving time, with around 90% of the patients mortality within 3 years after the initial diagnosis [1]. In modern surgery, many methods have been investigated for assisting precise malignant brain tumors resections. High-resolution intraoperative ultrasound, image guided frameless stereotaxy, intraoperative CT or MRI imaging and fluorescence microscopy are all adapted for the localization and identification of tumor tissue. Unfortunately none of these supplementary methods seem to provide sufficiently accurate information to solve all challenges for accurate surgical guidance.

The idea in this project is to distinguish the tissue types by combining information from tissue auto-fluorescence, fluorescence from the contrast agent ALA-induced PpIX, as well as diffuse reflected light. Malignant glioma cells will take up ALA as a consequence of a damaged blood-brain-barrier in tumor tissue, and convert ALA into strongly fluorescent protoporphyrin IX (PpIX). The PpIX concentration in the tumor can reach up to 50 times the concentration in the surrounding brain. With 405nm excitation light, the PpIX would fluorescence intensively around 635nm.

A system for surgical guidance could thus be based on detecting the characteristic spectrum of protoporphyrin IX in order to locate the tumor border [3]. If based on fiber optics, it would provide means for localizing of protoporphyrin IX in the surgical bed. This approach has been pursued by several research groups, e.g. Valdés et al. [4] and Kim et al. [5].

The system presented in this paper was inspired by the developments performed by Haj-Hosseini et al. at Linköping University [3,6]. This original instrument was named ‘optical touch pointer’ (OTP). The new system design mainly focus on increasing the system sensitivity, robustness, and ambient light influence rejecting ability by developing new signal processing methods. At the same time a new light detecting system are designed for constructing a more compact and robust system.

2. MATERIALS AND METHODS

2.1 System design

Arrangement of combined fluorescence/reflectance system

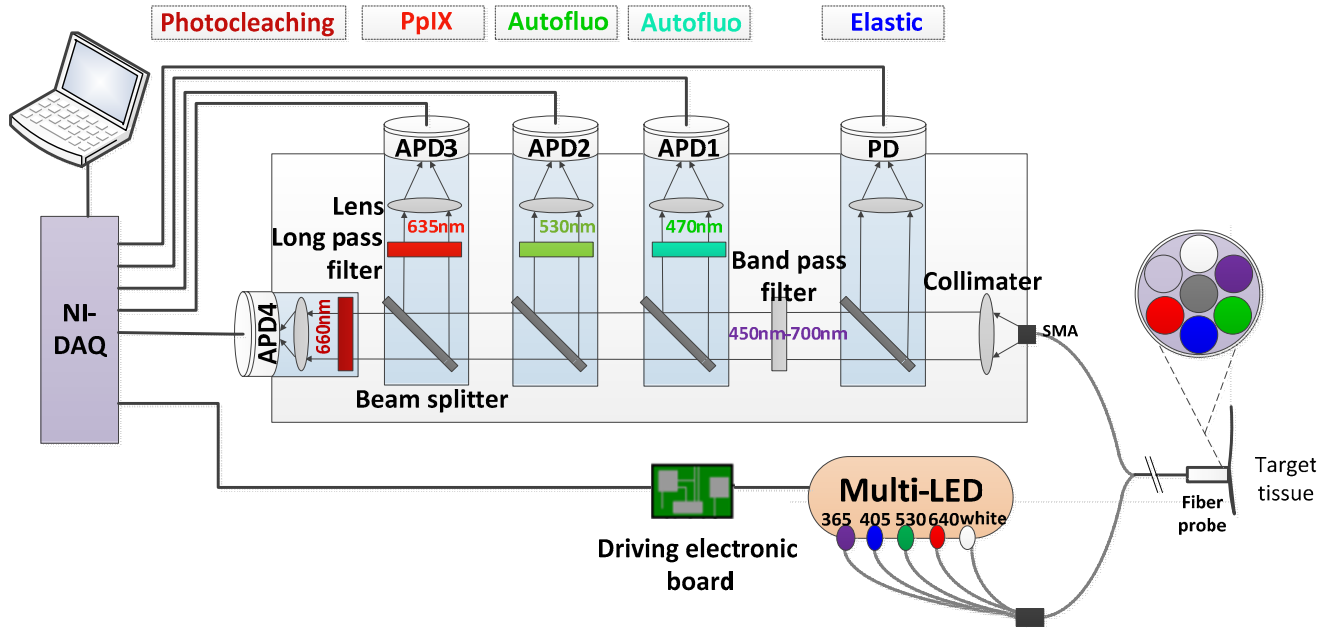


Figure 1. Schematic diagram of the combined fluorescence/reflectance system

As shown in Figure 1, the system consists of three distinct parts with corresponding interfaces (filtering) in between: a light source unit consisting of 5 Light emitting diodes(LED)s, light guiding fibers, and a detection part. In order to build a compact system insensitive to ambient light, a multi-LED source including 5 LEDs (365nm, 405nm, 530nm, 640nm and white light) is employed in the design. In this multi-LED source, 365 nm-LED is used to excite tissue auto-fluorescence and 405 nm-LED is for generating PpIX fluorescence with an intensity peak at 635 nm. The other three LEDs (530,640nm and white) are used for monitoring tissue diffuse reflectance at various wavelengths. This could potentially be used for compensating the fluorescence signal with light attenuation determined by the tissue optical properties. The 5 LEDs are coupled to individual optical fibers. The distal ends of the fibers are surrounding a central detection fiber in an optical probe (Fiber Patch Cord Bundle, Prizmatix Ltd). All fibers have a core diameter of 750 μm diameter and a NA of 0.5, the fiber length is 4 m. At the end of the bundled there is a 5 cm long hand-held stainless steel probe. The detection fiber guides collected light to a compact detection unit. This unit is constructed for directing light of different wavelengths onto 5 independent light detectors including 1 Photodiode (Edmund Optics; 53378) for diffuse reflected light channel, and 4 Avalanche Photodiodes (APDs) (Hamamatsu; S9075) for 510nm, 530nm, 635nm, 660nm wavelength bands. After efficient amplification electronics, the signals are directed to a data acquisition board (NI-DAQ card) for data acquisition and further signal processing.

Each light sensing unit is fixed at the end of an independent custom-designed plastic tube. A band pass filter (Edmund Optics; 470-10, FB530-10, FB-635-10, and FB-660-10, respectively) followed by a focusing lens was placed in front of every sensing unit. The band pass filters sort out the desired wavelengths and the focusing lens focuses the expanded light beam to match the detectors' detecting area. One long pass filter (GG-435, Edmund Optics) is set after the 405nm channel for suppress the diffuse reflected light from entering the other channels.

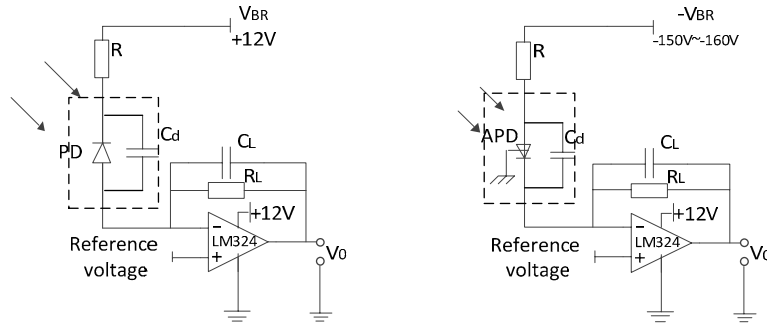


Figure 2. APDs and PD amplification circuit design sketches.

The weak photocurrent on the photon detectors are converted to voltage result by amplification electronics. The design shown in Figure 2 is inspired by the designs described by *Hobbs, Philip C. D's*[7]. The operational amplifier shown in the figure is the four paths multi-amplifier LM324. R_L is $75k\Omega$ in both the APD and PD electronic circuits. With this resistance the amplification power for both APD and PD would be the same, meanwhile the efficient dynamic range and bandwidth of the output can be ensured. C_L is set to be 10 pf in order to suppress the current swing across the detector capacitance C_d . With this design, the SNR loss of the system can be controlled below 1 dB , and response frequency of the amplifier unit can reach over 7 kHz .

2.2 Light source modulation and signal processing methods

In order to sufficiently suppress the influence of the ambient light, light intensity modulation is applied in the design. Two light modulation methods (TTL modulation and sinusoidal modulation) and corresponding signal processing methods were developed and tested.

TTL wave modulation and signal processing

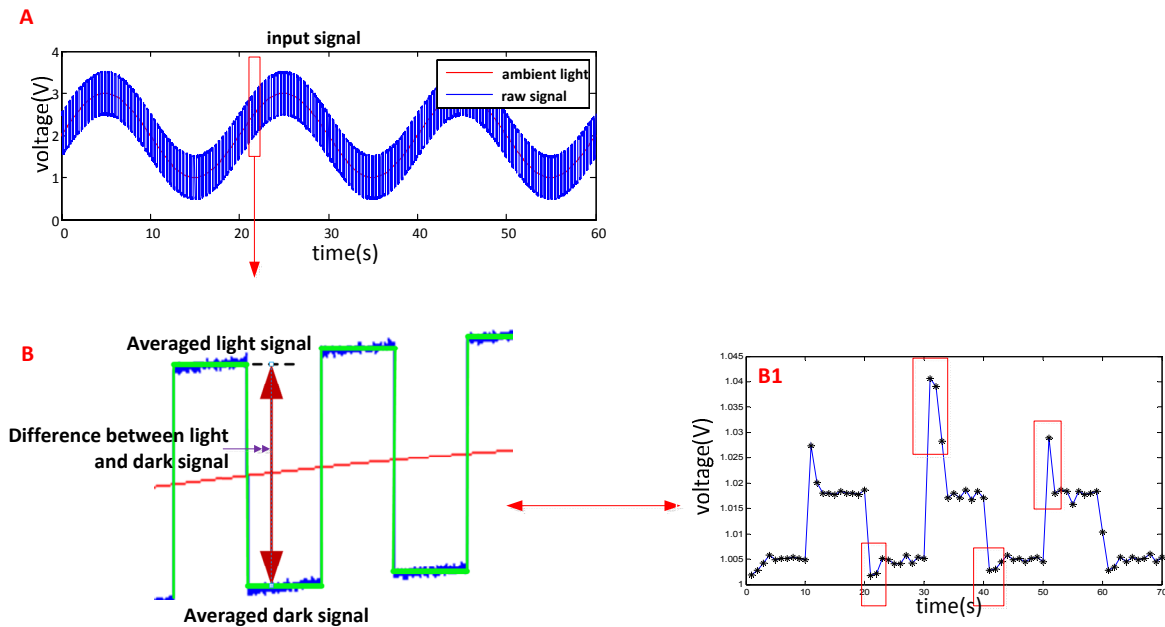


Figure 3. TTL wave modulation and signal processing. (A) shows the typical raw signal detected by the APD/PD unit, which is a summation of the high frequency pulses generated by the DAQ-card-modulated light source, and low frequencies ambient light signal (the sinusoidal signals). (B) shows the main signal processing details. (B1) shows the part of experimental raw signal

From Figure 3. (B) one can see if light source modulation frequency is sufficiently high, in the short time period for each pulse the raw signal intensity variation should be small. This is the essential reason why fast modulation is preferred.

To process the signal, the raw signal is first averaged over every half cycle to obtain two raw-data results in each cycle, the averaged light signal I_{Light} , and also the averaged dark signal I_{Dark} . Later the data is processed to reduce the influence from the ambient light and other unknown parameters during the recording according to:

$$I_{signal}(i) = (I_{Light} - I_{Dark})_{fluo(i)} / (I_{Light} - I_{Dark})_{Ref(i)} \quad (1)$$

In Equation (1), $i \geq 1$ refers to the signal cycle number. This compensating process eliminates much of the influence of light intensity variation caused by probe holding geometry differences, and of tissue type variation.

As an addition, one example experimental raw signal is shown in Figure 3. (B1), the high signal peaks appear in the figure are caused by the operational amplifier, when sharp signal change occurs in the signal the amplifier easily generates a transient signal peak. These peaks are removed in advance before the processes shown in Figure 3. (B).

Sine wave modulation and signal processing

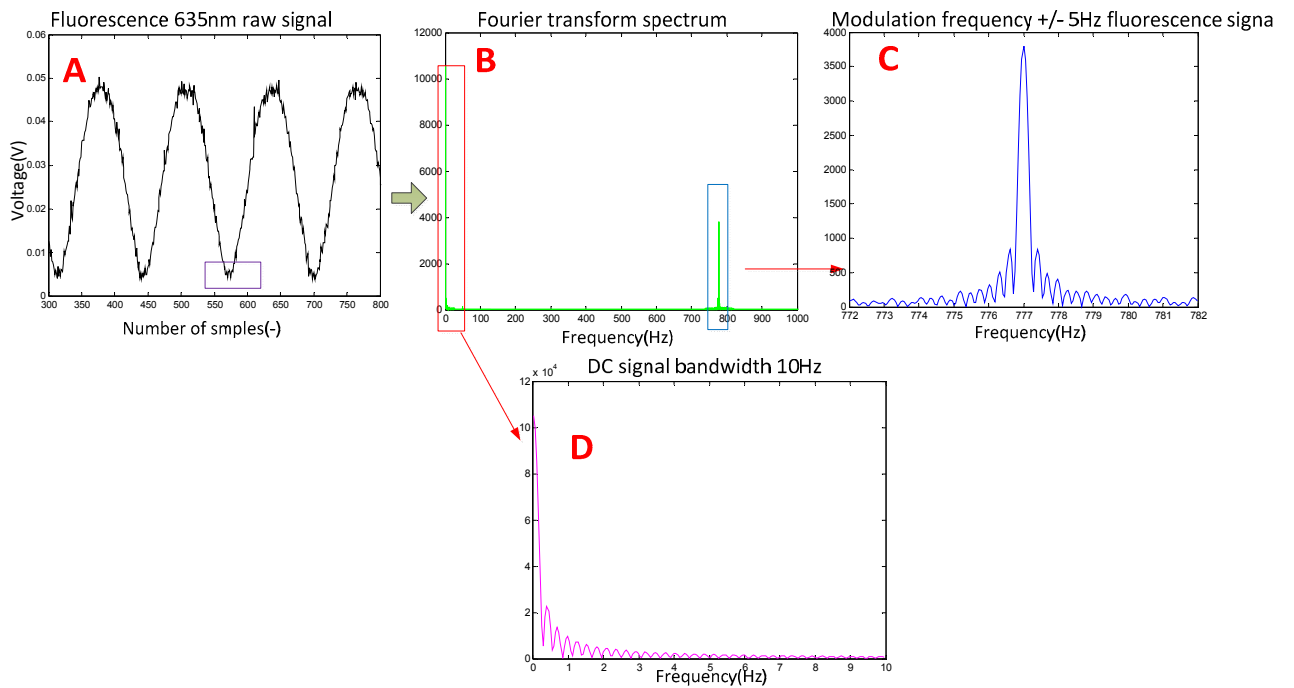


Figure 4. Sine wave modulation, (A) shows the raw fluorescence signal which is the summation of the attenuated modulation signal, high frequency noise signals and a DC component. (B) shows the Fourier transformed raw signal. In the figure there are two obvious peaks located at 777Hz which is the light source modulation frequency as shown in detail in (C), and 0Hz presenting the DC component as shown in (D).

The signal peak in Figure 4. (C) is integrated with 10Hz bandwidth around the central modulation frequency. The result obtained presents the fluorescence light intensity.

In both methods the ratio of fluorescence signal to diffuse reflectance signal are calculated, this is for compensating the light source intensity fluctuation as well as tissue optical properties change.

In the signal processing, the influence of noise is first reduced by signal filtering, and the signals are then multiplied by a calibration factor to provide a true signal level. The calibration considers optical losses in the signal path as well as detector efficiency. The internal gain in the APDs varies also with the temperature. Therefore the temperatures of the APDs are measured and the correction factor is a function of temperature.

2.3 Software development

LabVIEW[®] (National Instruments) is used to control the light source modulation, acquire signal and also to perform signal processing. In the software we have also created multifunction interfaces corresponding to the two modulation methods. The Matlab[®] (Mathworks[™], Inc.) is, on the other hand, used for laboratory signal analysis and simulation.

3. RESULTS AND DISCUSSIONS

3.1 System setup

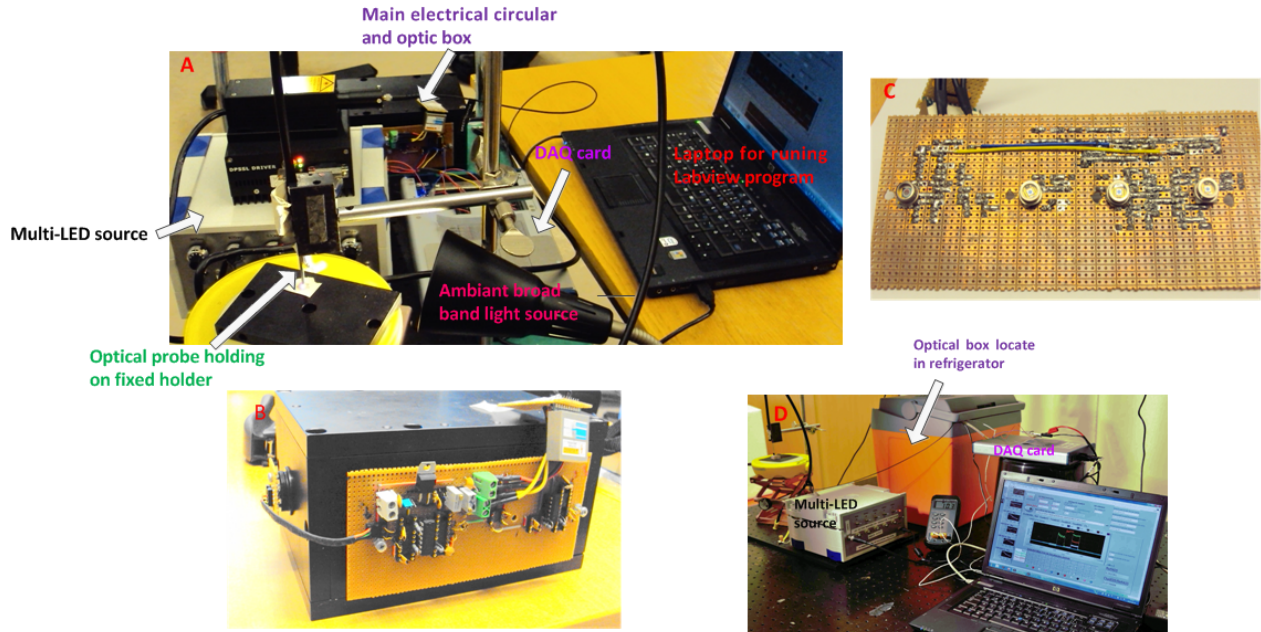


Figure 5. Final system hardware set up. (A) A view of the complete system. (B) Detailed view of the optical box, The designed electrical board is attached and fixed at the side of the optical box, most linking cables and components are portable. (C) A view of electrical board from the back side, the position of photo-detectors is based on the geometry of the optical box, so that the APDs and PD can be inserted into the holes aligned on the side wall of the optical box. (D) In order to obtain stable gain of the detecting components, the whole optical box was located in the car refrigerator box running at a fixed temperature of 14.5C° during some tissue phantom studies..

In the long term experimenting with the system, the stability and good performance of the hardware design is proved.

3.2 Labview interfaces

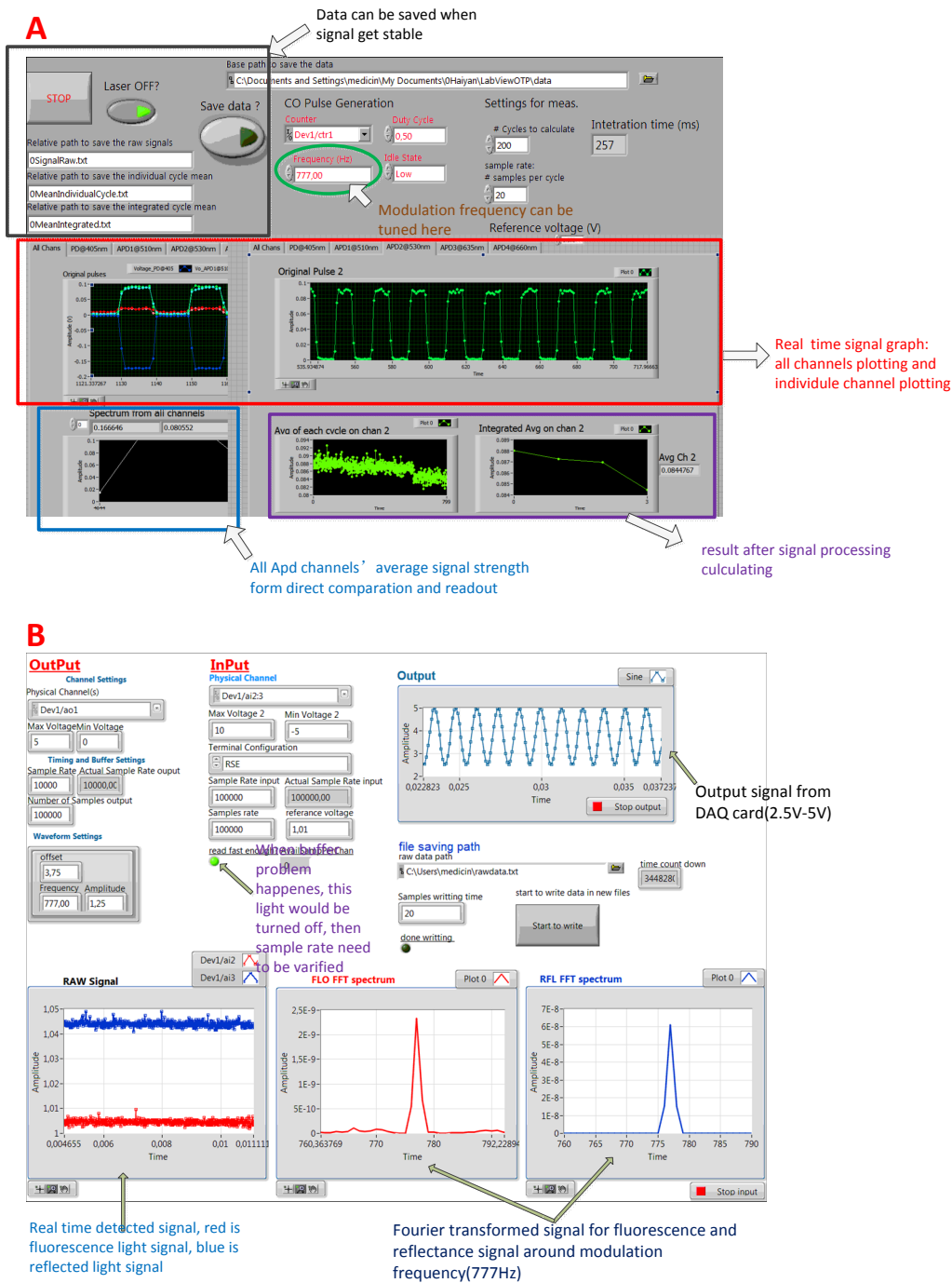


Figure 6. (A) Front panel of the system in LabView® program for TTL wave modulation.(B) Front panel of the system LabView® program for sine wave modulation.

In both interfaces, the recorded raw signal and processed results from several channels are presented in real-time. At the same time, all the experiment data can be saved in independent txt files for further data analysis with Matlab® .

3.3 System performance evaluation

The system performances were explored from two aspects: The ambient light suppression ability and the PpIX sensitivity. The evaluation mainly focused on signals from 635nm (PpIX characteristic fluorescence) channel, and the reflection channel, since the PpIX fluorescence is of particularly interest for tissue diagnostics.

A liquid phantom including 3.5% volume of Intralipid, 0.5% of Indian Ink (1:100 stock solution) and 96% water was prepared. The system was tested under large variation in the ambient light level (from 15 to 2300 lm/m^2). The light source used in the experiment was a stable ring light. PpIX powder (0.056 g) was dissolved in 20 mL of DMSO and 80 mL of distilled water was added to obtain a 1 mM PpIX stock solution.

Ambient light suppression ability

In the ambient light suppressing tests, liquid tissue phantom with 100 nM PpIX concentration was used. And the system is tested under large variation in the ambient light level (from 15 to 2300 lm/m^2). The light source used in the experiment was a stable ring light.

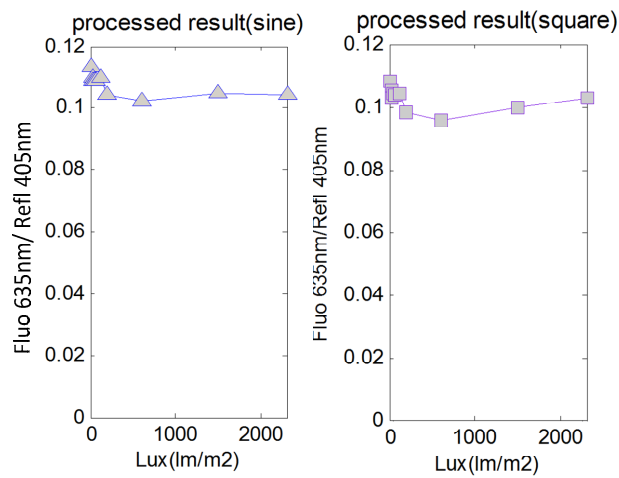


Figure 7. System ambient light suppressing tests result for sine/square wave modulation.

These two plots in Figure 7 are thus presenting the results of the ambient light rejection of two systems. They show extremely high similarities between the results for the two modulation schemes. From the figures one can understand that the ambient light suppression is very efficient for both techniques, and only influences the final signal to a small extent (4.5% maximum variance). Thus both processing methods can achieve almost ambient light influence-free fluorescence detection. The slight variation in the final signal may be due to fact that the PpIX was not homogeneously dissolved, indicated by very similar variations in both curves.

PpIX quantification ability

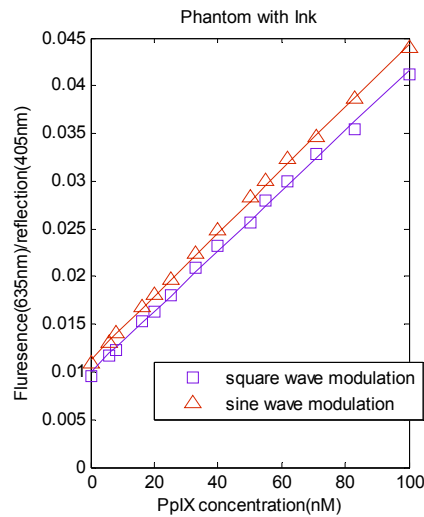


Figure 8. Linearity and sensitivity of system PpIX quantification ability test, results from ink-based tissue phantom with sine and TTL wave modulation methods. The solid lines are the linear fit of the points.

As shown in Figure 8, great linearity is shown on the fluorescence/reflectance ratio signal intensity versus PpIX concentration in the range from 10nM to 100nM for both methods. The slightly higher value from sine wave modulation method might be due to the fluorophore bleaching, as the experiment of sine wave modulation method was measured first. Despite the low PpIX concentrations in these tests is much lower than of clinical relevance, the signal-to-noise ratio still seems to be acceptable at the lowest PpIX concentration for both modulation schemes.

4. CONCLUSION

The paper described a combined fluorescence/reflectance spectroscopy system aiming for GBM resection developed within Lund University biophotonics group. With the use of low cost and compact multi-LEDs as light sources, and the high sensitivity APDs and PD as light detection units, the system is shown to be able to dramatically decreased the long signal integration time needed and enriches the functions of the first generation system [1].

From laboratory tests, the system shows capability of measuring weak signals in the presence of strong ambient light, which is of importance for brain surgery guidance. Also the system has high sensitivity to low PpIX concentration (much lower concentrations than expected in brain tumors) even in highly absorbing and tissue phantoms. Also, it is proved that the system works equally well with both TTL and sinusoidal modulation methods, which gives more choices for the future system developing.

The system combines the fluorescence and reflectance, with the potential to measure the fluorophore concentration in tissues, independent on tissue optical properties. Also the original desire for a high efficient, compact and robust system is achieved by delicate designing of electronic circuit. The LabView program made friendly simple interface, ultimately simplifying the system operating. With the promising data, further clinical evaluation of the system is under process.

ACKNOWLEDGEMENT

The authors warmly acknowledge fruitful discussions and collaborations with Karin Wårdell, Neda Haj-Hosseini, Johan Richter, Malin Svensson, Jonas Gårding, Ola Svärm and Niels Bendsoe. The project was financially supported by VR, SSF, VINNOVA, and the Linneus Centre at LLC.

REFERENCES

- [1] Zhiyuan Xie, "Novel fluorescence/ reflectance spectroscopy system for guiding brain tumor resection," Lund University master thesis, 3-21 (2013).
- [2] N. Haj-Hosseini, J. Richter, S. Andersson-Engels, and K. Wårdell, "Photobleaching behavior of protoporphyrin IX during 5-aminolevulinic acid marked glioblastoma detection," *Proceedings of SPIE* 7161, 8 (2009).
- [3] N. Haj-Hosseini, J. Richter, S. Andersson-Engels, and K. Wårdell, "Optical touch pointer for fluorescence guided glioblastoma resection using 5-aminolevulinic acid," *Lasers in Surgery and Medicine* 42, 9–14 (2010).
- [4] P. A. Valdés, A. Kim, F. Leblond, O. M. Conde, B. T. Harris, K. D. Paulsen, B. C. Wilson, and D. W. Roberts, "Combined fluorescence and reflectance spectroscopy for in vivo quantification of cancer biomarkers in low- and high-grade glioma surgery," *Journal of Biomedical Optics* 116007,7 (2011).
- [5] Jones, C. J., Director, Miscellaneous Optics Corporation, interview, Sept. 23 2011 A. Kim, M. Roy, F. Dadani, and B. C. Wilson, "A fiberoptic reflectance probe with multiple source-collector separations to increase the dynamic range of derived tissue optical absorption and scattering coefficients," *Optics Express* 18, 94 (2010).
- [6] N. Haj-Hosseini, Stefan Andersson-Engels, Karin Wardell, "Fluorescence Spectroscopy Measurements in Ultrasonic Navigated Resection of Malignant Brain Tumors," *Lasers in Surgery and Medicine* 43, 8-14 (2011)
- [7] P. C. D. Hobbs, [Building Electro-Optical Systems: Making It all Work], Wiley.com Vol.71, 542–545(2009).

Papers IV

Development of a novel combined fluorescence and reflectance spectroscopy system for guiding high-grade glioma resections

Monirehalsadat Mousavi, Haiyan Xie, Zhiyuan Xie, Mikkel Brydegaard, Johan Axelsson, and Stefan Andersson-Engels
Lund University, Department of Physics, P.O. Box 118, SE-221 00, Lund, Sweden

1. ABSTRACT

Total resection of glioblastoma multiform (GBM), the most common and aggressive malignant brain tumor, is challenging among other things due to difficulty in intraoperative discrimination between normal and residual tumor cells. This project demonstrates the potential of a system based on a combination of autofluorescence and diffuse reflectance spectroscopy to be used as an intraoperative guiding tool. In this context, a system based on 5 LEDs coupled to optical fiber was employed to deliver UV/visible light to the sample sequentially. Remitted light from the tissue; including diffuse reflected and fluorescence of endogenous and exogenous fluorophores, as well as its photobleaching product, are transmitted to one photodiode and four avalanche photodiodes. This instrument has been evaluated with very promising results by performing various tissue-equivalent phantom laboratory and clinical studies on skin lesions.

2. INTRODUCTION

Surgical resection of glioblastoma tumors, the most common and aggressive type of malignant brain tumor, is difficult due to its similarity in appearance to surrounding brain tissue and its infiltrative growth pattern. The standard method used today for tissue discrimination during surgical resections is visual inspection and palpation. Ultrasound and MR images are also taken before and after surgery in order to locate the tumor, delineate the borders between malignant and healthy tissue, as well as to verify the result of the resection. This information is not always sufficient for optimal surgical results.

The main idea of this project is to develop a system that can assist the surgeon in distinguishing tissue types during brain tumor resection. This system is based on an optical fiber probe, enabling *in vivo* fluorescence and reflectance spectroscopy during surgery. The tissue discrimination in the fluorescence signals is based on both endogenous fluorescence and contrast agents, while the reflectance correlates with optical properties of the tissue. The contrast agent employed is 5-aminolevulinic acid (ALA)-induced protoporphyrin IX (PpIX). It is assumed that the PpIX concentration is well correlated with the malignant transformation of the tissue. The ALA is administered orally to the patient prior to surgery. Malignant glial tumor tissue will then build up a higher concentration of Protoporphyrin IX, providing a fluorescence peak at 635 nm following 405 nm light excitation. The primary goal is obviously to provide a signal with high sensitivity and specificity for malignant tissue.

The idea for the system is thus to combine multi-wavelength diffuse reflection and fluorescence signals to obtain information related to PpIX concentration, independent on the amount of blood in the tissue. The previous generation of this setup, called optical touch pointer (OTP) [1] was also somewhat sensitive to ambient light during the measurements, such as microscope lamp and room light in the operating room. In that system laser was as a source for fluorescence excitation illumination and a spectrometry method was used to detect fluorescence signals during tumor resection. The suppression capability of background light was not fully optimal, mainly due to that the signal integration time was rather long. The ambition was to reduce this sensitivity in the now presented system. By pulsing the light sources and employing lock-in detection, this ambient light can very efficiently be suppressed in the detection. This method has in lab tests proven to detect very low PpIX fluorescence concentrations in tissue phantoms, with insignificant influence of ambient light. An *in vivo*

elaborate test on skin tumor was conducted with this specific system to demonstrate its full capability, before the systems will be taken into use in the ongoing clinical research program for glioblastoma tumors.

3. MATERIALS AND METHODS

3.1 System specification

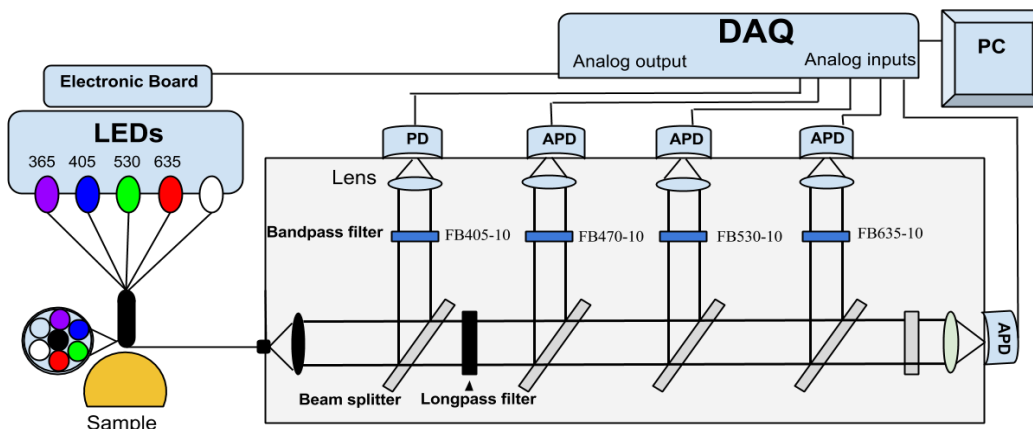


Figure 1. Schematic representation of the system

The system developed with the purpose to be useful for guiding brain tumor resections is outlined in Figure 1, including a schematic illustration of the distal end of the fiber-optic probe. It has three main parts: A light source, a fiber optical probe and a detector unit. The light source (Prizmatix Ltd.) is constructed of LEDs with four different wavelengths: 365nm, 405nm, 530nm, 635nm as well as a white light LED. The UV light is used to excite endogenous fluorophores in tissue, while the violet light serves as an excitation source for PpIX. Other wavelengths and white light are used to provide reflection data and thus signals correlating with optical properties from the tissue at these wavelengths. The light source is controlled by the output ports of a 16-bit data acquisition (DAQ) board (Supplier, Type No. USB6351). A labview program controls the light generation sequences and time intervals between the on (high voltage) and off (low voltage) mode of the LEDs. For this purpose, a custom made electrical board was designed and connected to the Digital Clock (CTR) output channel of the DAQ board.

The hand-held fiber-optical probe delivers light to the sample by five optical fibers each with a core diameter of 750 μm , a numerical aperture of 0.5 and a length of 4 meters suitable for the operating room. The optical fiber located in the center of probe is used to collect fluorescence and diffusely reflected light from the sample and guides the collected light to the detection unit. There is a fiber collimator (Edmund Optics; 64770) in front of the detection unit. The collimated light is split into five different light paths by means of four dichroic beam splitters (BS) (Thorlabs; DMPL425, 505, 567, and 638, respectively). The detector after the first beam splitter is a silicon photodiode (PD) (Edmund Optics; 53378). This is employed to detect diffusely reflected UV and violet light from the probed tissue. Four avalanche photodiodes (APD) (Hamamatsu; S9075), are used to detect the collected endogenous fluorescence light, exogenous PpIX-fluorescence and its photobleaching products, and also reflectance from the red, green and white LED. To suppress the strong diffusely reflected light from reaching the APDs, a long pass cutoff filter (3 mm Edmond optics GG-435) is mounted between the first two detector channels. Bandpass filters (Edmund Optics; FB405-10, FB470-10, FB530-10, FB-635-10, and FB-660-10, respectively) are mounted in front of each detector to transmit only the desired spectral band of light to each detector. The

bandpass filters are followed by a lens to focus the light onto the center of the active area of the detector. The photocurrents from the photodetectors are first converted to voltages by five trans-impedance amplifiers, one for each detector, transmitted to five analogue inputs of the DAQ board and then sent to the computer. Real-time control and initial data analysis is performed in LabView (Version 2012, National Instruments).

3.2 Signal processing

Light intensity modulation has been employed in the data acquisition for two reasons. Firstly, it was important to measure the signals generated for the five LEDs independently. Secondly it was essential to enable measurements in strong ambient light conditions. The periodic square-wave modulation has been evaluated to modulate the light from the source in this system. This modulation is based on a TTL signal generated from the CTR port of the DAQ board. a series of square wave pulses is created with a varied voltage sequence with square wave voltage pulses between 0 (low) and 5V (high) at a frequency of 777 Hz. The resulting waveform from the square wave modulation consists of a 777 Hz repeated time sequence of 11 time slots. This sequence includes one time slot where each of the LEDs is on at maximum and reduced power, respectively, and one where they are all switched off. The main reason to apply voltage in high and low power is to monitoring the power fluctuation resulted from temperature variation of LEDs. For each detection channel, the average signal value within each of these time slots is calculated and the background from ambient light measured with all LEDs switched off is subtracted from all signals. In order to increase the signal-to-noise ratio, this sequence is repeated over 70 cycles and an average value was calculated, corresponding to a 90 ms integration time.

3.3 Samples

In order to validate and test the system performance, water-based tissue phantoms were prepared. The tissue phantom employed in this study was based on three major ingredients, an absorber, a scatterer and a fluorophore. Diluted Intralipid (Fresenius Kabi, Sweden; 200 mg/ml), which is a fat emulsion, was added to provide the required scattering properties, while bovine blood (purchased from a local supermarket) or diluted India ink (Pelican Fount, Germany; 1:100 stock solution prepared in our lab), were used as absorbers. The Protoporphyrin IX (PpIX, Fisher Scientific) was served as a fluorophore. In order to better control and suppress any aggregation of PpIX in the phantom, the surfactant tween (Scharlau Chemie) was mixed into the phantom. The phantoms were designed to mimic the optical properties of gray matter of brain tissue.

4. RESULT

4.1 System linearity assessment

Several sets of experiments were carried out to validate our setup. First only 405nm excitation light was used for studies on system validation of system linearity response and background light suppression capabilities in a dark room as well as under well controlled ambient light conditions. In the first series of experiments liquid phantoms were prepared by mixing 3.5% volume of Intralipid, 0.5% of Ink (1:100 stock solution) and 96% water. PpIX powder (0.056 g) was dissolved in 20 mL of DMSO and 80 mL of distilled water was added to obtain a 1 mM PpIX stock solution. The fluorophore concentration in the tissue phantom was, in this series of measurements, varied between 10 to 100 nM. The phantom with the highest fluorophore concentration was prepared in a glass cylinder container. The lower concentrations have subsequently been prepared by diluting with the initial tissue phantom, without any fluorophore. A gentle stirring of the sample during measurement was employed to prevent the fluorophores from aggregation and to minimize the photobleaching so that the bleached dye

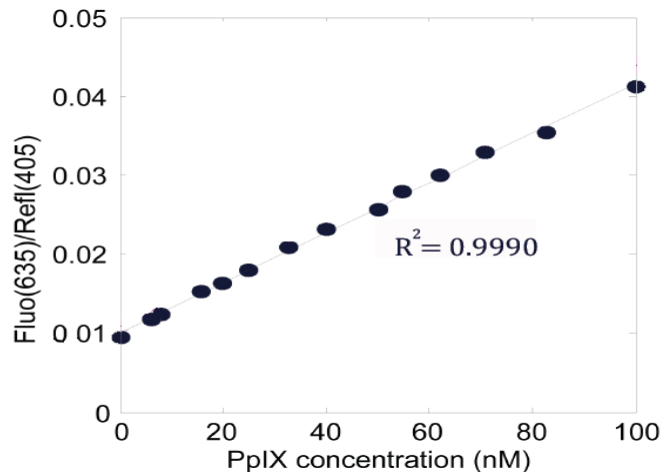


Figure 2. PpIX quantification using blue light. The solid line indicates a linear fit to the data

molecules directly under the tip of the delivering fiber were continuously replaced by fresh fluorophores. The measured data need to be corrected to account for any small variation in source power. For this purpose, the ratio between fluorescence and reflection signals was formed. Figure 2 shows the results from the first set of measurements. The ratio has a very linear dependence on the fluorophore concentration for both the square and sine wave modulations using 405 nm LED as an excitation source. The work has shown that very low fluorescence concentration is detectable by this system, much lower concentrations than is expected in brain tissue during clinical use [2].

4.2 Ambient light suppression

As mentioned in the Introduction, the previous generation of this setup (OTP) [1] was sensitive to the ambient light during the measurements, such as fluorescence microscope lamp and room light in the operating room. In order to evaluate the capability of suppressing ambient light with the present system, measurements were conducted with tissue phantoms under well controlled ambient light conditions. In this study we used a white light ring-lamp from a microscope with similar emission spectrum to the surgical operating microscope, to examine the influence of different light conditions on the recorded signals. A tissue phantom with 100 nM PpIX concentration was prepared and the ring light was located at varying distances vertically above the sample to provide an even illumination of different intensities. A light-meter was used to quantitatively determine the ring light intensity at the surface of the tissue phantom. The experiment started with a 60 centimeter distance from the sample. The distance was then decreased to obtain a stronger ambient light condition.

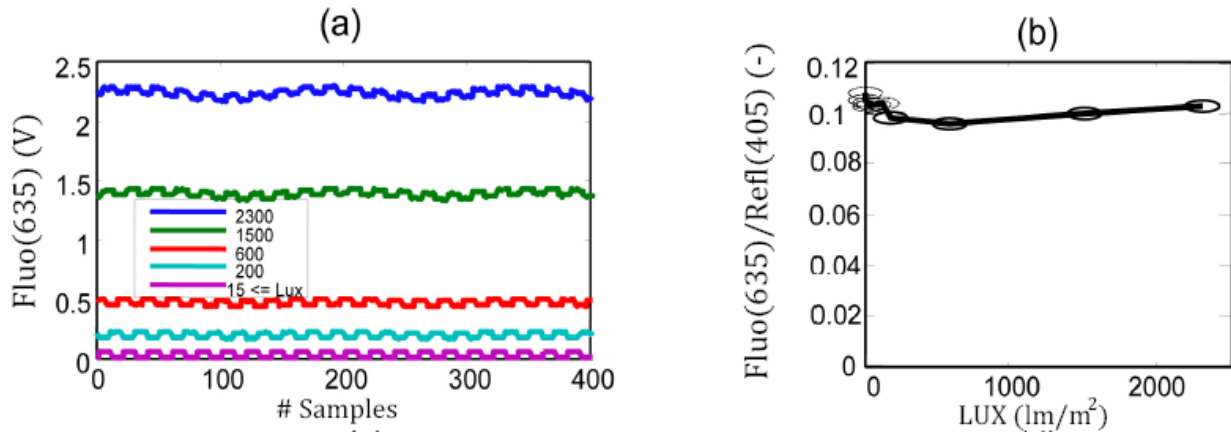


Figure 3. Sensitivity of the system to the ambient light level for a fixed PpIX concentration of 100 nM. Figures (a) shows the raw data when the blue light was modulated by a square waves and (b) demonstrates the fluorescence vs reflection ratio (i.e. the evaluated signal corresponding to the PpIX concentration) in different ambient light conditions.

Figure 3(a) illustrates the results, including raw data, for different ambient light conditions. Since the ambient light has the modulations in the low frequency range (0-100 Hz), the detected signal with a modulation at 777 Hz is totally related to the light from the LED source. In The low frequency wavy shape of the raw data curves is related to the ring light and the relatively small pulses were produced from the 777 Hz frequency-modulated LED. Figure 3(b) illustrates the evaluated signal level as a function of the ambient light intensity. Here, the on-off lock-in type of subtraction was performed for the 777 Hz modulation to remove the influence of the ambient light. As mentioned in the experimental setup chapter, the average signal value was for these plots calculated over 70 cycles to increase the signal-to-noise ratio. The results clearly indicate that the measured signal is almost completely dominated by the ambient light, while the fluorescence signal could be recovered almost uninfluenced by the ambient light when the lock-in type of subtraction was performed.

4.3 Evaluation protocol

Now, after having been able to successfully demonstrate the capability of suppressing any influence of ambient light on the detected signal using one 405 nm excitation source, all channels were connected. The multiple LEDs were run sequentially using an electrical board (multiplexer) connected to the DAQ board. In order to evaluate the experimental data, multivariate analysis is used in the data processing. The partial least squares (PLS) method was employed to develop a linear model of sample fluorescence and optical properties from 269 different samples varied in known dependent variables such as absorption, scattering and fluorescence. Intralipid concentration varies between 3% -8% of the whole phantom volume, while 0%-4% of the blood concentration was considered as an absorption variation. Protoporphyrin concentration was varied between 0 to 1000 nM. The samples were prepared through several dilution steps starting from the highest concentration. It was diluted into the lowest concentration and the last sample was measured in a separate container without any fluorophore. The measurement process occurs similarly to the previous experiment. For the PLS model regression, data normalization was done and a data matrix was created. This model can be used to predict the fluorescence concentration in unknown samples in the future, as long as the absorption, scattering and fluorescence properties fall into the interval of this set of samples. Leave-one-out methodology was used to evaluate the accuracy of predicting the fluorophore concentrations. LOO-CV split the dataset into two groups, it left one observation as the validation data, and the remaining observations were used to build the PLS regression model and this was repeated so that each variable was used as validation data.

Linear regression analysis was performed using the data from all sample measures to correlate between predicted and true properties for different variables. Figure 4 illustrates the relation between these values and also indicates their coefficient of determination. This coefficient denotes the goodness of linear relation between responds and predicted values. As can be seen, the estimated blood and intralipid concentration are highly correlated with correlation coefficient of 0.99 and 0.98, respectively. For fluorescence concentration, the correlation coefficient is lower at 0.84. The result shows the viability of PLS regression for intralipid/scattering, blood/absorption, and PpIX fluorescence concentration estimation using the multi-LEDs arrangement. It was recognized that there was an instability in the APDs temperature since it is well known that APD gain is very sensitive to ambient temperature.

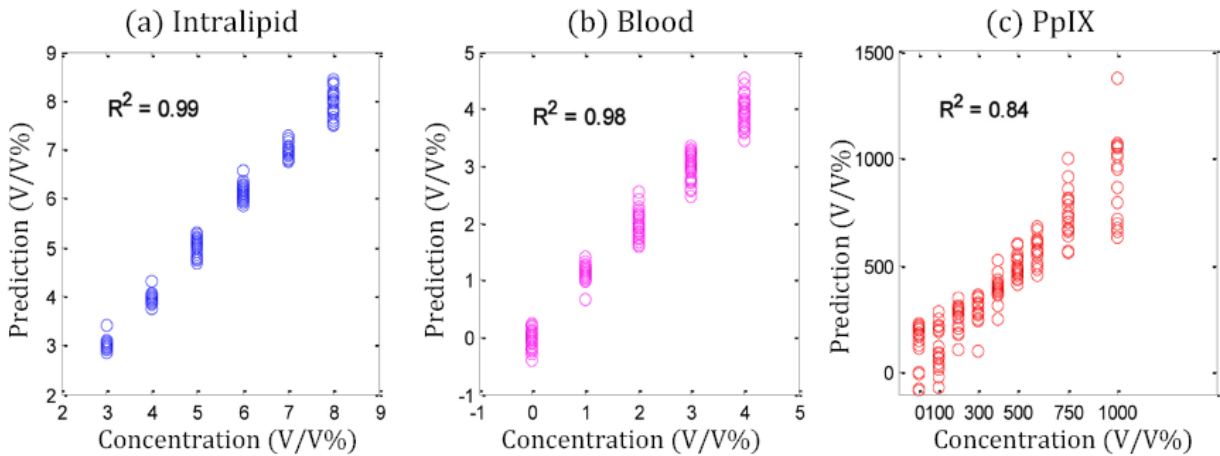


Figure 4. PpIX quantification in liquid phantom with various optical properties. a) Predicted Intralipid concentration b) Predicted blood concentration and c) Predicted PpIX concentration.

4.4 *In vivo* experiments

In order to ensure that the system will work in complex living systems, an *in vivo* clinical human trial was performed. Skin tumors are easily accessible and such tumors were used in this first clinical trial. The whole setup was packed on to a

portable case for outpatient clinical data acquisition and carried to the clinic of Dermatology at Skåne University Hospital in Lund.

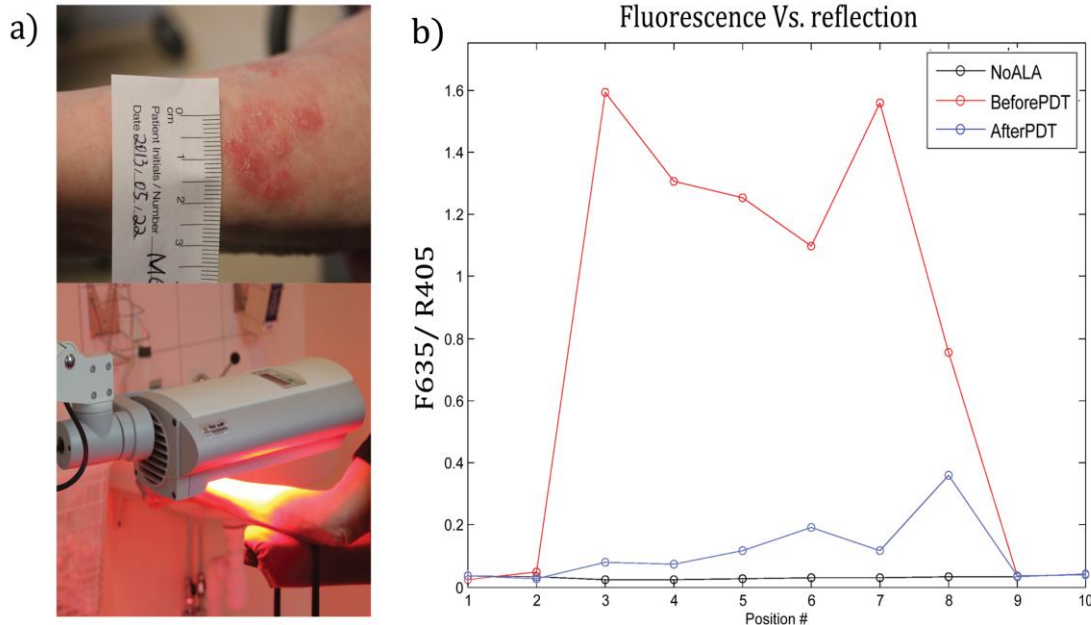


Figure 5. a) A typical skin tumor under treatment .b) In vivo fluorescence reflectance spectroscopy of a patient with a skin tumor before ALA administration before PDT and after PDT.

Figure 5 (a) presents one of the eight measurements of the different experiments conducted on patients with skin tumor undergoing PDT. The PpIX accumulation at the site of application in the skin tumor is obvious from the results presented in the Figure 5(b). In this case it was straight forward to detect the lesion in the turbid tissue with a robust distinction. The curve after PDT evidences PpIX existence after treatment which indicates a somewhat prolonged photosensitivity of this drug in the lesion.

5. CONCLUSION

A novel combined fluorescence reflectance spectroscopy system based on LED-excitation and APD-detection has been developed and evaluated. The system is built as an intraoperative guiding tool for resection of glioblastoma, the most frequent and complex to treat the malignant brain tumor. The LEDs as diagnostic light sources are interesting in respect of their compactness and low cost. As well, it provides sufficient intensity at the desired wavelengths, and any wavelength desired for the diagnostics. The main advantage for the present application of APDs as detectors, instead of a spectrometer used in the previous generation of the system [1] is the short integration time. This makes it possible to correctly subtract any ambient background light in a noise-free manner.

The combined use of reflectance and fluorescence, using different wavelength of interest, optimizes the diagnostic capabilities. The UV light excitation source provides information about tissue autofluorescence properties. The other light sources are employed to compensate for any variations of optical properties of the examined tissue. The use of multiple detection wavelengths in parallel allows to also compensating for any small fluctuations in the LED output by forming dimensionless ratios of detection signals. The blue light is also utilized to induce PpIX fluorophore. Accurate extraction of intrinsic fluorescence could potentially provide better diagnostic accuracy.

The linearity study conducted demonstrates that very low fluorescence signal can be detected in the presence of strong ambient light with the developed system. The ambient light suppression, as a main challenge in previous study, is successfully achieved for improved clinical applicability. Multivariate analysis of the signals has proved a great potential in separating the contributions to the signal from fluorescence, absorption and scattering in a series of tissue phantom measurements.

The clinical trials on skin tumors were performed in order to test the instrument and its performance. While the data are promising, future work will focus on improving the system performance and preparing the setup to carry out real time measurement in collaboration with Linköping University for ALA-guided brain tumor resections.

6. ACKNOWLEDGMENT

The authors warmly acknowledge fruitful discussions and collaborations with Karin Wårdell, Neda Haj-Hosseini, Johan Richter, Malin Svensson, Jonas Gårding, Niels Bendsoe and Ola Svärm. The project was financially supported by the Swedish Research Council (VR); the Swedish Foundation for Strategic Research (SSF); the Swedish Governmental Agency for Innovation Systems (VINNOVA); as well as by the Linneus Centre at Lund Laser Centre.

References

1. N. Haj-Hosseini, J. Richter, S. Andersson-Engels and K. Wardell, "Optical Touch Pointer for Fluorescence Guided Glioblastoma Resection Using 5-Aminolevulinic Acid," *Laser Surg Med* 42(1), 9-14 (2010)
2. A. Johansson, G. Palte, O. Schnell, J. C. Tonn, J. Herms and H. Stepp, "5-Aminolevulinic Acid-induced Protoporphyrin IX Levels in Tissue of Human Malignant Brain Tumors," *Photochem Photobiol* 86(6), 1373-1378 (2010)